DISSERTATION

Numerical Modeling of Flow Distribution and Sediment Transport for Channel Contractions

Submitted by

Joon-woo Noh

Department of Civil Engineering

In partial fulfillment of the requirements

for the degree of Doctor of Philosophy

Colorado State University

Fort Collins, Colorado

Spring 2003

UMI Number: 3092687

ProQuest Information and Learning Company
300 North Zeeb Road
P.O. Box 1346
Ann Arbor, MI 48106-1346

COLORADO STATE UNIVERSITY

November 14, 2002

WE HEREBY RECOMMEND THAT THE DISSERTATION PREPARED UNDER OUR SUPERVISION BY **JOON-WOO NOH** ENTITLED **NUMERICAL MODELING OF FLOW DISTRIBUTION AND SEDIMENT TRANSPORT FOR CHANNEL CONTRACTIONS** BE ACCEPTED AS FULFILLLING IN PART REQUIREMENTS FOR THE DEGREE OF DOCTOR OF PHILOSOPHY

Committee on Graduate Work

Mohan Reddy

Berger Bai...

Thurman W. Smith

Albert Molinas
Advisor

Sandra Woods
Department Head

ABSTRACT OF DISSERTATION

Numerical Modeling of Flow Distribution and Sediment Transport for Channel Contractions

The main objective of this dissertation is to determine the flow distribution in channel contractions and to model the corresponding sediment transport. In channel contractions, the flow area is reduced, flow velocity is increased, and as a result the scour process is significantly increased. The intensity of local scour is amplified at locations where the velocity gradient is large. For the safety assessment of manmade hydraulic structures such as bridge abutments and coffer dam structures, the accurate assessment of scour problem is of great importance.

In the dissertation, first, using a numerical model flow distribution at contracted reaches investigated. This model solves the Reynolds and continuity equations for fully developed turbulent flows. Employing the streamlined upwind scheme in the finite element formulation, the algorithm provides numerical stability. In order to achieve computational efficiency, the penalty function is incorporated to satisfy the continuity condition automatically without solving an additional equation. The hydrodynamic analysis investigates velocity and shear distributions in channel contractions due to the skewed abutments with angle variations from 30° to 150° with 10° increments. The analysis is conducted for both single and double abutments. Following series of numerical simulations, a semi-empirical equation was derived for expressing maximum velocity as a function of the

contraction ratio, friction, and the skewness angle. Using this empirical equation, it is possible to determine the approximate maximum velocities and the corresponding shear stresses in contracted zones for different skewness angles. In designing footing depth and bank protection for hydraulic structures placed at angle to oncoming flows, this equation provides the magnitude of maximum velocities and the corresponding shear stresses without the use of complex numerical modeling.

Next in the dissertation, a bed load transport model is developed for scour analysis in contracted reaches; this model is applied to estimate scour in the Mississippi River. During Phase I of the Lock & Dam No. 26 replacement project, a cofferdam was constructed to reduce the width of Mississippi by approximately 50 %. Increases in flow velocities in the contracted region resulted in the significant lowering (erosion) of the channel bed. The numerical model solves the sediment continuity equation to investigate scour and deposition process in the vicinity of channel contractions. In an effort to achieve the benefit of matrix diagonalization, lumped matrix formulation was introduced and incorporated to the model. The proposed model is verified and its applicability is evaluated through the comparison with measured data.

Finally, the unsteady 2-dimensional convection and diffusion equation is solved numerically for the real-time simulation of suspended sediment propagation. The streamlined upwind scheme efficiently reduces numerical oscillations in convection dominated flows due to the high Peclet number. By using the mixed boundary condition to express the external source terms or externally induced suspended load as a function of time in the algorithm, the model is capable of handling not only continuous load cases but also non-continuous suspended load influx. The suspended load transport model was verified

using a case study for which an analytical exact solution is available and was applied to the real-time simulation of a suspended load influx case on the Mississippi River. The model algorithm provides a framework upon which water quality as well as contaminant transport models can be built.

Joon-woo Noh,
Civil Engineering Department,
Colorado State University,
Fort Collins, Colorado, 80523,
Spring, 2003

ACKNOWLEDGEMENTS

The author wishes to express his sincere gratitude and appreciation to his main advisor, Dr. Albert Molinas, for his guidance, advice, and continuous encouragement he provided throughout the course of this work. Sincere thanks are also extended to the graduate committee members, Dr. M. Reddy, Dr. B. Bienkiewicz, and Dr. F. Smith. Special thanks also due to Dr. Y. Hafez for his guidance and academic assitance.

The author wishes to thank his wife Soyen and my children for their understanding and support throughout the period of this work. Special thanks are also due to his aunt Suki and her husband for their warmest support and help.

The author wishes to thank his friend Dr. B.S. Kang who was working in ERC with the author during the period of his degree. Special thanks are also due to his friends Mr. H. Hussain and Dr. B. Bounvilay for their encouragement and support.

The author wishes to thank his parents for loving, caring, supporting and their prayers. Also, the author wishes to thank and always feels sorry for his sister who suspended her studies due to financial problems.

Finally, the author thank to God Jesus Christ, without him nothing can be possible.......

TABLE OF CONTENTS

1. INTRODUCTION 1

1.1. Problem Statement 1

1.2. Objectives 3

1.3. Procedures 4

2. LITERATURE REVIEW AND THEORY 8

2.1. Governing Equations for Turbulent Flow 8

2.2. Computation of Fluid Stresses 11

2.2.1. Bottom shear stress 11

2.2.2. Wind shear stress on the surface 14

2.2.3. Lateral stresses 15

2.3. Turbulent Viscosity 17

2.4. Wall Boundary Conditions 18

2.5. Turbulence Models 20

2.5.1. One-equation models 20

2.5.2. Two-equation models 21

2.6. Finite Element Method for Fluid Flow 23

2.7. Abutment Studies 26

2.7.1. Laboratory studies for investigating flow around abutments 26

2.7.2. Numerical studies for investigating flow around hydraulic structures 28

2.8. Review of the Sediment Transport Theories 30

2.8.1. Logarithmic velocity profile ... 30

2.8.2. Smooth and rough boundary surface ... 32

2.8.3. Laminar sublayer and shear Reynolds number ... 33

2.8.4. Roughness coefficient for resistance to flow ... 34

2.8.5. Critical shear stress ... 36

2.8.6. Theoretical approach for bed form analysis ... 39

2.8.7. Bed load transport equations ... 41

2.8.8. Suspended load transport ... 42

3. HYDRODYNAMIC MODEL ... 48

3.1. Basic Concept of Finite Element Method ... 49

3.2. Discretization of Domain ... 51

3.3. Convection Dominated Flow Problem ... 53

3.3.1. Petrov-Galerkin method ... 55

3.3.2. Comparison of the standard Galerkin and Petrov-Galerkin method ... 56

3.3.3. Application Petrov-Galerkin for multi-dimensional cases ... 58

3.4. The Penalty Function ... 60

3.5. Two-dimensional Navier-Stokes Equations ... 61

3.5.1. Discretization form of the x-momentum equation ... 63

3.5.2. Discretization form of the y-momentum equation ... 66

3.6. General Computational Procedure ... 69

3.7. Model Verification and Application ... 71

3.8. Single Abutments ... 76

3.9. Double Abutments 81

3.10. Analysis on the Maximum Velocity 85

3.11. Summary 93

4. SEDIMENT TRANSPORT MODELING IN CHANNEL CONTRACTIONS.......... 95

4.1. Bed load Transport 96

4.1.1. The sediment continuity equation 96

4.1.2. Finite element formulation of the governing equation............................. 101

4.1.3. Lumped capacitance matrix 103

4.2. Suspended Load Transport 104

4.2.1. Finite element formulation 105

4.2.2. Mixed boundary conditions 107

4.2.3. Turbulent mixing coefficients for suspended load transport 109

4.3. Model Validation 111

4.3.1. Model verification of bed load transport.. 111

4.3.2. Model validation and discussion of suspended load transport.................. 114

4.4. Model Application on the Mississippi River 117

4.4.1. Flow velocity distributions... 119

4.4.2. Application of the bed load transport model 120

4.4.3. Application of the suspended load transport model................................. 126

4.5. Summary 129

5. SUMMARY, CONCLUSIONS, AND RECOMMENDATIONS 131

5.1. Flow Distribution Analysis of Channel Contractions 132

5.2. Sediment Transport Analysis of Contracted Reaches 134

5.3. Recommendations 135

Appendix A. References 137

Appendix B. Evaluation of Element Matrices 147

Appendix C. Capacitance Matrix Diagonalization 150

Appendix D. Treatment on Nodal Point Boundary Values 153

Appendix E. Stability Analysis 156

Appendix F. Numerical Schemes for Unsteady Term 159

Appendix G. Determination of the Characteristic Length 163

Appendix H. Numerical Diffusion 165

Appendix I. Results of the Suspended Load Transport in the Mississippi River 167

LIST OF FIGURES

Figure 2.1 Modified Shields diagram (After Govers, 1987). 37

Figure 2.2 Particle motion diagram (After Julien, 1995). 38

Figure 2.3 Typical bed form transition in downstream direction. 39

Figure 3.1 Examples of typical two-dimensional element. 52

Figure 3.2 Applications for various Peclet numbers. 57

Figure 3.3 Variation of shear amplification with respect to protrusion ratio. 72

Figure 3.4 Comparison of computed values with measured shear amplifications. 72

Figure 3.5 Comparison between experimental and numerical results: (a) Kwan (1984) experiments; (b) numerical simulation for L/B=0.3 and U_a/V_*=12 75

Figure 3.6 Plotting lines in the contracted reach for single abutments. 76

Figure 3.7 Total velocity distributions for single abutment for the case of f = 0.02: a) θ = 50°; b) θ = 90°; c) θ = 130°. 77

Figure 3.8 Resultant velocity distributions in the contracted reach due to single abutments for the case of f = 0.02: (a) θ = 50°; (b) θ = 90°; (c) θ =130°. 79

Figure 3.9 Plotting lines in the contracted reach for double abutments. 83

Figure 3.10 Velocity distributions for double abutments: (a) 70° and 110°; (b) 90°. 83

Figure 3.11 Velocity profiles for contracted reach for double abutments: (a) θ = 50° and 130°; (b) θ = 70° and 110°; (c) θ = 90°. 84

Figure 3.12 Variation of velocity amplification with skewness: (a) f = 0.08; (b) f = 0.02; (c) f = 0.0088. 90

Figure 3.13 Variation of maximum velocities with skewness angle using Equation (3.9.3) with: (a) f = 0.08; (b) f = 0.02; and (c) f = 0.0088. 91

Figure 3.14 Relationship between maximum velocities and skewness angle from Equation (3.9.3) for different f values at: (a) upstream; (b) mid-point; and (c) downstream station. 92

Figure 3.15 Comparison of maximum velocities computed from the FEM model and from Equation (3.9.3)....93

Figure 4.1 Shear stress distributions (a) without curvature correction (b) with curvature correction. 101

Figure 4.2 Velocity distributions and zone of the analysis. 112

Figure 4.3 Channel bed topographies in the contracted reach....113

Figure 4.4(a) Standard Galerkin without numerical diffusion....116

Figure 4.4(b) Standard Galerkin with numerical diffusion....116

Figure 4.4(c) Petrov-Galerkin without numerical diffusion. 116

Figure 4.5 Location and plan view of the study reach. 117

Figure 4.6 Mesh generation for the study reach in the Mississippi River....118

Figure 4.7 Flow velocity distributions in the study reach of the Mississippi River......119

Figure 4.8(a) Bed elevation distributions in contracted reach after 1 day (24 hours). 122

Figure 4.8(b) Bed elevation distributions in contracted reach after 3 days (72 hours)......123

Figure 4.8(c) Bed elevation distributions in contracted reach after 10 days. 124

Figure 4.9 Comparison between measured (a) and computed (b) bed elevation. 125

Figure 4.10 Numerical results of the suspended load transport model. 128

Figure G.1 General bilinear quadrilateral element (After Heinrich & Pepper, 1999)....164

LIST OF TABLES

Table 3.1 Resultant maximum velocities for single abutments. 80

Table 3.2 Resultant maximum velocities for double abutments. 85

Table 3.3 Coefficients of Equation (3.9.1) from nonlinear statistical analysis. 87

CHAPTER 1

1. INTRODUCTION

1.1. Problem Statement

Channel contractions result in the reduction of flow area. In channel contraction zones, due to the local increase in velocities, shear stresses, vortices, and turbulence, bed topographies are subject to significant changes. Flow area reduction may occur due to natural river geometry or due to the presence of manmade hydraulic structures. In case of contraction due to hydraulic structures, such as bridge abutments, dikes, and coffer dams, flow velocity increases locally and flow pattern changes. The combination of these factors leads to the removal of channel bed material from around the foundations of these hydraulic structures and the development of local scour holes. Therefore, the determination of flow properties in channel contractions is very important in the design and construction of these structures. It is also important for the safety assessment of the bank protection and in the determination of the rip-rap material sizes.

Generally, the determination of the flow field around hydraulic structures is achieved through numerical simulation. In this study, a two-dimensional finite element model was proposed and used for the analysis of flow motion in channel contractions. Variations in flow parameters such as increases in local velocity that significantly influence the channel-bed scour are identified using a numerical model. The model solves the Navier-Stokes equations using the upwind finite element scheme. In the algorithm, vertical gradient effects are accounted for by using the power law to express the vertical distribution of longitudinal velocity. The advantage of this approach is that the vertical variation, which is neglected in depth-averaged models, is incorporated. Basically, the flow model solves the Reynolds-averaged turbulent flow equations along a horizontal plane passing through on average water surface.

Using this model, the hydrodynamic analysis is conducted in channel contractions formed by vertical wall abutments. While most abutment studies are conducted for abutments placed perpendicular to flow, the attention in this dissertation is on the flow distributions in contracted reaches due to skewed vertical wall abutments. Through the examination of the lateral velocity profiles, the maximum velocities and the velocity distributions corresponding to different angles of inclinations are discussed and related to those encountered for vertical abutments. From successive model applications, an analytical expression relating velocity amplification factor to contraction ratio and angle of inclination is derived.

Shear stresses corresponding to flow velocities can be used to predict bed elevation changes. This is accomplished by solving the governing sediment continuity equation. In the algorithm, by incorporating the flow continuity equation into the shear stress computation, the concept of equilibrium scour is taken into account. By solving the convection and diffusion equation, suspended load transport is also included in this study. The model predicts the variation of suspended load concentration due to flow field. Using the proposed numerical model, the suspended load transport behavior as well as distribution of the concentration can be efficiently visualized for the entire flow domain.

After model verification, the application to the Mississippi River demonstrated the practical use of the sediment transport model. In the study reach of the Mississippi River used for example application, a typical channel contraction occurs due to the coffer dam construction. The numerical analysis examines bed elevation changes as well as suspended load transport. Employing the upwind finite element scheme, the algorithm used in the model provides numerical stability and reduces numerical oscillations that commonly occur in the convection dominated flow problems.

1.2. Objectives

The main goal of this dissertation is to propose and use a numerical model to determine the flow velocity and sediment transport in contracted reaches. The analysis is focused on the following items:

(a) Flow distribution in channel contractions due to straight and skewed abutments:

1. Velocity profiles in asymmetrical contracted reaches due to skeweness;
2. The effect of flow intensity and the roughness coefficient on velocity distribution;
3. Application and discussion of different boundary conditions;
4. The location and the amplification factor of the maximum velocity in contracted reaches.

(b) Bed load transport in contracted reaches:

1. Understanding of fundamental processes of the bed load transport;
2. Determination of scour depth using bed load transport equations;
3. Application of unsteady FEM modeling scheme; and
4. Investigation of the location and magnitude of maximum scour.

(c) Suspended load transport in open channels with a contracted reach:

1. Numerical solution of the suspended sediment transport equation;

2. Identification of the concentration of the suspended load distribution;
3. Simulation of suspended load propagation in real time; and
4. Extending model application to cases other than suspended load transport.

1.3. Procedures

The flow analysis focuses on the flow distribution in contracted reaches due to the skewed abutments. The range of skewness angle changes is reasonably chosen using practical limits and was varied with 10° angle increments. Assigning boundary conditions in the mesh generation program a series of numerical simulations are conducted corresponding to different skewness angles. The computational accuracy is provided by using very fine non-uniform finite element mesh.

In the mesh generation algorithm, assembling individual element matrices, results in a very large global matrix for the computational domain. In two-dimensional finite element problems, since the global matrix is typically very sparse, it is desirable to reduce the bandwidth of the global matrix. This can be achieved by assigning temporary node numbers to original ones and after the solution is obtained, by replacing the temporary node numbers with the original ones once again. The advantage of this scheme is not only to reduce the storage space but also to save computational time. As a result of this renumbering scheme, the computations are up to 10 times faster than those without renumbering procedure. The steps followed in the flow distribution analysis are listed as follows:

1. Using the model, flow distributions in the contracted reach due to the vertical wall abutments are determined.
2. The analysis is focused on the flow in the contracted reach due to skewed vertical wall abutments with changes the inclination of abutments relative to the approach flow.
3. To study angle variations, the angle abutments make with the bank are changed from 30° to 150° with increments of 10°, while keeping the projected flow contraction ratio constant.
4. The process is repeated for 2 different types of abutment configurations: i) the single abutment case, ii) the double abutment case.
5. Each of the two cases is examined for different contraction ratios under varying flow angle and different flow intensities to examine the combined effects.
6. An analytical expression relating velocity amplification to the contraction ratios, total width and to the angle of inclination is derived.

Based on the resultant flow velocity, the shear stress on the channel bottom can be obtained mathematically. The shear stress distribution is subsequently used to determine general bed elevation changes. In general, when the flow passes through a channel contraction, a higher velocity gradient is expected. This leads to higher shear stresses and the removal of channel bed materials. In a more direct approach to determine the scour depth, it is possible to compute the amount of sediment using bed load transport equations. However, sediment motion is still difficult to model numerically, because it is a complex fully three-dimensional process due to turbulent flows.

The bed load transport equation is given in terms of critical shear stress, shear stress, and particle diameter. Also, there is a close relationship between scour process and flow depth. The flow depth increase as a result of scour reduces corresponding shear stresses. Then the scour process gradually decreased until the equilibrium state is met in which scour process discontinues. Conversely, in the deposition zone, due to decrease in total flow depth, minor scour occurs until sediment transport reaches an equilibrium state. The changes in bed elevation can be mathematically described by solving the sediment continuity equation. In this dissertation, the sediment continuity equation is solved by using the finite element method, and the results of quantitative analysis are presented. The main steps followed in the bed elevation changes including model development are listed as follows.

1. The hydrodynamic model is applied to the real river and the sediment continuity equation is solved after the flow distribution is obtained,
2. It is assumed that the channel bed is covered by non-cohesive uniform sand, and the armoring factor and fractional load configuration are not taken into account,
3. In order to express shear stress in terms of the flow depth, an algorithm which converts the pressure term into the flow depth is incorporated into the model,
4. The analysis of bed elevation transition is carried out in the contracted reach,
5. Location of maximum scour depth is identified.
6. Since the flow velocity and depth are related through the continuity equation, an algorithm reflecting effects of bed elevation changes on velocities is used.

While the bed load transport occurs in contact with channel bed, fine sediments are brought into the suspension due to turbulent flow fluctuation. The transport process of suspended load can be described mathematically by well-known convection and diffusion equation. This equation is applicable for various open channel flow modeling problems, such as contaminant transport or water quality. The suspended load transport model should be capable of handling the suspended load introduced into the river regime in a continuous or instantaneous manner. The following items are taken into account in the suspended load transport model development and the analysis:

1. The governing equation of suspended load transport is solved using the Petrov-Galerkin finite element method.
2. For the treatment of the unsteady term, diagonalization scheme of the capacitance matrix is applied.
3. The propagation of suspended load is visualized in real time simulation,
4. Discussion of the choosing the integration time step is provided,
5. Various numerical schemes of the time integration are reviewed,
6. Discussion on the selection of parameters, such as diffusion coefficients is provided,
7. Through the comparison with an analytical solution for which a theoretical solution exists, the model is validated.
8. The mixed boundary condition for the treatment of the inflow from the tributary channel is discussed.

CHAPTER 2

2. LITERATURE REVIEW AND THEORY

In this chapter, mathematical governing theories related to this study are reviewed and investigated. In the first section of literature review, the governing equations for incompressible turbulent flows are discussed. They include the continuity equation and Reynolds-averaged momentum equations. The fundamental assumption is that the flow is time independent, fully developed, and two-dimensional. Each term of the governing equation, especially stress terms, such as lateral and bottom shear stresses are investigated in detail. Review of the past work is focused on the flow motions and its distribution in channel contractions observed around bridge abutments. Based on the laboratory as well as numerical works, the configuration of the experimental conditions including flow parameters is discussed.

The second section of this chapter covers theories of sediment transport, bed load and suspended load, respectively. Sediment continuity equation linked with bed load transport equations describes bed elevation changes mathematically. The convection and diffusion equation expresses the suspended load transport in terms of additional diffusion coefficients along with the flow velocity. The mathematical derivation and numerical manipulation of these equations are investigated and reviewed based on past applications.

2.1. Governing Equations for Turbulent Flow

The governing equations describing the flow motion are based on the conservation laws for mass and momentum. These equations are written in tensor notation as:

Mass conservation (continuity equation)

$$\frac{\partial U_i}{\partial x_i} = 0.0 \tag{2.1.1}$$

Momentum conservation (Navier-Stokes equations)

$$\frac{\partial U_i}{\partial t} + U_j \frac{\partial U_i}{\partial x_j} = -\frac{1}{\rho}\frac{\partial P}{\partial x_i} + \nu \frac{\partial^2 U_i}{\partial x_j^2} + f_i \tag{2.1.2}$$

where, U_i ($i = 1,2,3$) are the instantaneous velocity components in the direction X_i, P is the instantaneous pressure, and f_i are body forces per unit mass in the X_i direction.

For turbulent flows, Equations (2.1.1) and (2.1.2) describe temporal and spatial variations for the flow velocity and pressure. The time and space scales cover a broad range and solving these motions numerically is not feasible for practical applications. For this reason, the instantaneous velocity, U_i, in the X_i -coordinate direction, is expressed as summation of the time-averaged velocity, $\overline{U_i}$, and the fluctuation part, u_i'

$$U_i = \overline{U_i} + u_i' \tag{2.1.3}$$

Following the same approach, the pressure P is written as

$$P = \overline{P} + p' \tag{2.1.4}$$

The time average of a quantity, for example, $\overline{U_i}$, is calculated as follows

$$\overline{U_i} = \frac{1}{T}\int_0^T U_i \, dt \tag{2.1.5}$$

In general, while the local time average of the fluctuating part is zero, the average of the fluctuations product is nonzero i.e.

$$\overline{u_i'} = 0, \quad \overline{u_i' u_j'} \neq 0 \tag{2.1.6}$$

Performing time average in the way indicated by Equation (2.1.5) and after substituting Equations (2.1.3) and (2.1.4) into Equations (2.1.1) and (2.1.2), yields

$$\frac{\partial \overline{U_i}}{\partial x_i} = 0 \tag{2.1.7}$$

$$\frac{\partial \overline{U_i}}{\partial t} + \overline{U_i}\frac{\partial \overline{U_i}}{\partial x_j} = -\frac{1}{\rho}\frac{\partial \overline{P}}{\partial x_i} + \frac{\partial}{\partial x_j}\left(\nu \frac{\partial \overline{U_i}}{\partial x_j} - \overline{u_i' u_j'}\right) + f_i \tag{2.1.8}$$

This averaging process introduces unknown double correlations between the fluctuating velocities. These time-averaged nonzero products of turbulent fluctuation act as stresses on a fluid element. These stresses are called turbulent stresses and can be expressed as follows.

$$\tau_{ij} = -\rho\, \overline{u_i' u_j'} \tag{2.1.9}$$

where, ρ = fluid density; and $\overline{u_i' u_j'}$ = the time-averaged product between fluctuating velocity components, the temporal cross-correlation.

The subscripts i and j denote x_i and x_j -coordinate directions, respectively. Since the time averaged formulation was first introduced by Osborne Reynolds in 1883, the stress terms are also referred as Reynolds stresses. In many flow regions, the turbulent stresses are larger than their laminar counterparts and they can be therefore neglected. Equation (2.1.8) can be rewritten as

$$\frac{\partial \overline{U_i}}{\partial t} + \overline{U_i}\frac{\partial \overline{U_i}}{\partial x_j} = -\frac{1}{\rho}\frac{\partial \overline{P}}{\partial x_i} + \frac{\partial}{\partial x_j}\left(\frac{\overline{\tau_{ij}}}{\rho}\right) + f_i \tag{2.1.10}$$

Omitting the over-bar for simplicity, the expanded form of the Reynolds equation of motion and continuity, for steady, incompressible, fully developed flows can be explicitly written as

$$\frac{\partial U}{\partial x}+\frac{\partial V}{\partial y}=0 \tag{2.1.11}$$

$$U\frac{\partial U}{\partial x}+V\frac{\partial U}{\partial y}=-\frac{\partial}{\partial x}\left(\frac{P}{\rho}\right)+\frac{\partial}{\partial x}\left(\frac{\tau_{xx}}{\rho}\right)+\frac{\partial}{\partial y}\left(\frac{\tau_{xy}}{\rho}\right)+\left[\frac{\partial}{\partial z}\left(\frac{\tau_s}{\rho}\right)\right]_{z=H}+F_x \tag{2.1.12}$$

$$U\frac{\partial V}{\partial x}+V\frac{\partial V}{\partial y}=-\frac{\partial}{\partial y}\left(\frac{P}{\rho}\right)+\frac{\partial}{\partial x}\left(\frac{\tau_{yx}}{\rho}\right)+\frac{\partial}{\partial y}\left(\frac{\tau_{yy}}{\rho}\right)+\left[\frac{\partial}{\partial z}\left(\frac{\tau_n}{\rho}\right)\right]_{z=H}+F_y \tag{2.1.13}$$

where, U is the flow velocity in the x-direction (longitudinal); V is flow velocity in the y-direction (lateral); P is the mean pressure; $F_x = g\sin\theta$ and $F_y = 0$ are body forces in the longitudinal and lateral direction respectively; g is the gravitational acceleration; θ is averaged water surface slope in the longitudinal direction of flow; z is vertical distance from the channel bed; H is averaged flow depth; τ_s and τ_n are the longitudinal and lateral turbulent shear stresses respectively.

The first two terms of Equation (2.1.12) and (2.1.13) are convective accelerations and represent inertial forces. The first and last terms in the right-hand side of Equation (2.1.12) and (2.1.13) represent the mean pressure and water surface gradient respectively. The second and third terms in the right-hand side of Equation (2.1.12) and (2.1.13) represent the combined effects of viscous stress and Reynolds stress.

2.2. Computation of Fluid Stresses

2.2.1. Bottom shear stress

The velocity field of fluid flow is affected by the friction on the bottom of the channel. The assumption for bottom shear stress, τ_b, is that the magnitude is the same as that corresponding to steady, uniform flow and that it acts in the direction of the flow velocity.

For one-dimensional flow, the bottom shear stress or friction can be computed by well-known formula by Chézy as

$$\frac{U_{av}}{V_*} = \frac{C}{\sqrt{g}} \tag{2.2.1}$$

$$\text{with } V_* = \sqrt{\frac{\tau_b}{\rho}} \tag{2.2.2}$$

where, C = Chézy discharge coefficient, τ_b = bottom shear stress, and V_* = shear velocity

Using this relationship, the bottom shear stress can be rewritten as

$$\tau_b = \rho\, k_b\, U^2 \tag{2.2.3}$$

where, ρ = mass density of the water; k_b = a dimensionless local shear-stress coefficient; and U = averaged cross sectional velocity

The shear stress coefficient k_b also can be expressed as

$$k_b = \frac{f}{8} \tag{2.2.4}$$

where, f = Darcy-Weisbach friction factor.

For two-dimensional flow, bottom shear stress components τ_{bx} and τ_{by} are given by

$$\tau_{bx} = \rho k_b U \sqrt{U^2 + V^2} \tag{2.2.5}$$

and

$$\tau_{by} = \rho k_b V \sqrt{U^2 + V^2} \tag{2.2.6}$$

where, U, V = velocities in the horizontal x-and y-coordinate directions, respectively.

The Darcy-Weisbach friction factor, f, is related to the roughness and the Reynolds number of the open channel flow. It is recommended for use by Committee of the Hydraulics Division of the American Society of Civil Engineers (1963). Most of the surface water in the open channels are developed and considered to be turbulent flows in fully rough regime. Consequently, f predominantly depends on the roughness of the bottom surface. In two-dimensional flow, the approximate mean velocity profiles are assumed to follow logarithmic distribution (Chow, 1959). Based on this assumption and the results from many experiments, an appropriate value for the roughness coefficient for fully developed uniform flow in the fixed open channel system can be determined as

$$\frac{1}{\sqrt{f}} = 2\log\left(\frac{12R}{k_s}\right) \tag{2.2.7}$$

where, R = The hydraulic radius; and k_s = A characteristic length parameter.

The hydraulic radius R is equal to the flow depth in two-dimensional flow and the coefficient, k_s is called the roughness height. The ratio of k_s/R is denoted as the relative roughness.

According to Henderson (1966), the choice of value of k_s implies equivalence between the surface roughness and surface uniformly coated with sand grains of diameter k_s. If a bed composition is known, values of k_s can be directly obtained. Otherwise, it has to be obtained from published values specified for selected surface descriptions. As a result, it may not be easy to determine the accurate value of k_s and the coefficient k_b is computed using the well known Chézy-Manning equation (Chow, 1959) written as

$$k_b = \frac{g}{C^2} \tag{2.2.8}$$

and

$$k_b = \frac{gn^2}{2.208H^{1/3}} \tag{2.2.9}$$

where, C = Chézy coefficient; and n = Manning roughness coefficient; g = gravitational acceleration; H = depth of flow; and the factor 2.208 is used when g and H are expressed in inch. Chézy Coefficient, C, and the Darcy-Weisbach friction factor, f, depend on the surface roughness and are also functions of Reynolds number. The equation which expresses the relationship between these to coefficients can be written as follows

$$C = \left(\frac{8g}{f} \right)^{1/2} \tag{2.2.10}$$

In addition, the relationship between the coefficients C and n is expressed as follows

$$C = 1.49 \frac{H^{1/6}}{n} \tag{2.2.11}$$

In fully rough and turbulent conditions of the flow, the n is kept constant for each channel surface. Chow (1959) and Barnes (1967) suggested values of Manning coefficient, n, for natural rivers and flood plain.

2.2.2. Wind shear stress on the surface

This shear stress is for the relationship between wind and upper layer of water surface. When wind exerts a drag force on the water surface in the direction of the wind, the movement of upper layer of water surface in contact with the air produces turbulent kinetic energy and transports to the water depth. This stress is transmitted throughout the entire depth of flow for a shallow water system, and thus affects the mean velocity by diffusion and advection. The equation for relating surface wind stress, τ^s, with wind velocity can be written as

$$\tau^s = k \rho_a W^2 \tag{2.2.12}$$

where, k = a drag coefficient; ρ_a = density of air; and W = wind velocity near the water surface. For the two-dimensional flow, components of surface wind stress in the x- and y- coordinate directions can be written as

$$\tau_x^s = k\rho_a W^2 \cos\psi \tag{2.2.13}$$

and

$$\tau_y^s = k\rho_a W^2 \sin\psi \tag{2.2.14}$$

where, ψ = the angle between the direction of wind and x- axis.

2.2.3. Lateral stresses

The turbulent stress terms lead the numbers of unknowns in the governing equation more than the numbers of equations. To obtain the solutions to the governing equations, these turbulent stress terms should be expressed in terms of the flow motion variables. Numerous research studies developed mathematical basis for investigation of the mean turbulent flow motion. Majority of the investigations in turbulence modeling are conducted in the fields of fluid mechanics and aeronautical engineering. Various authors (Launder and Spalding, 1972; Rodi, 1993) provided the state of art reviews on turbulence modeling.

One of the classical approaches for the Reynolds stress in three-dimensional flow was proposed by Boussinesq in 1877, who assumed that the turbulent stresses are directly proportional to the mean velocity gradients. This is expressed by the following equation

$$\tau_{ij} = \rho\left[\nu_T\left(\frac{\partial u_i}{\partial x_j} + \frac{\partial u_j}{\partial x_i}\right) - \frac{2}{3}k\delta_{ij}\right] \tag{2.2.15}$$

where, ν_T = kinematic eddy viscosity; u_i = time averaged velocity; k = turbulent kinetic energy; and δ_{ij} = kronecker delta. In Equation (2.2.15), the term that involves the Kronecker delta is required to satisfy the normal stress conditions when $i = j$. In this case, the velocity gradients yield the normal stresses as

$$\tau_{11} = 2\rho\nu_T \frac{\partial u_1}{\partial x_1} , \qquad \tau_{22} = 2\rho\nu_T \frac{\partial u_2}{\partial x_2} , \qquad \tau_{33} = 2\rho\nu_T \frac{\partial u_3}{\partial x_3} \tag{2.2.16}$$

The continuity equation is

$$\frac{\partial u_i}{\partial x_i} = 0 \tag{2.2.17}$$

The sum of normal stresses is required to equal zero. By definition, all of the normal stresses are positive and their summation is

$$\tau_{11} + \tau_{22} + \tau_{33} = -2\rho k \tag{2.2.18}$$

McGuirk and Rodi (1987) extended this concept to the vertically integrated fluid motion by replacing ν_T and k of Equation (2.2.15) with $\bar{\nu}_T$ and $\bar{k}$, which are depth averaged quantities. Although these are not truly depth average values in the mathematical sense, when used in Equation (2.2.15), the proper quantities are obtained.

The eddy viscosity coefficient depends not only on the property of the fluid, but also on the state of the turbulent motion so that it may vary abruptly from one point to another or with time. The assumption of isotropic eddy viscosity in Equation (2.2.15) is also one of the simplifications; therefore, definitions of turbulence momentum transport are employed for directional eddy viscosity. According to Pinder and Gray (1977), the use of eddy viscosity has the desirable effect of increasing stability of the model.

However, in cases where turbulent stresses are important, a constant eddy viscosity model is not sufficient for accurate simulation of the behavior of flow.

2.3. Turbulent Viscosity

For more advanced turbulent models than eddy viscosity model proposed by Boussinesq, Prandtl suggested the mixing-length hypothesis in 1925, to find relations describing the distribution of eddy viscosity. Based on the assumption that eddies move around in a fluid like molecules in a gas, he related the eddy viscosity to the mean velocity gradient,

$$\nu_T = l_m{}^2 \left| \frac{du}{dy} \right| \tag{2.3.1}$$

where, u = time averaged velocity in the x-coordinate direction; and l_m = Prandtl mixing length. von Kármán (Schlichting, 1968) suggested the following expression to relate l_m to the mean velocity

$$l_m = \kappa \left| \frac{du/dy}{d^2u/dy^2} \right| \tag{2.3.2}$$

in which κ = von Kármán's constant. Experiments have shown that the value of κ is not universal but the average value of about 0.4 is used in typical applications. For more general cases, Rodi (1980) extended the mixing-length hypothesis as follows

$$\nu_T = l_m{}^2 \left[\left(\frac{\partial u_i}{\partial x_j} + \frac{\partial u_j}{\partial x_i} \right) \frac{\partial u_i}{\partial x_j} \right]^{1/2} \tag{2.3.3}$$

From this equation, the kinematic eddy viscosity is given in terms of l_m and mean velocity gradients. However, due to the difficulty to specify l_m for complex flows, this formulation has not been frequently used.

Following the von Kármán's mixing length of Equation (2.3.2), the well-known logarithmic velocity distribution can be derived. Based on this velocity distribution and experimental study on the pipe flow, Elder (1959) presented the following equation for the flow in infinite inclined wide panel

$$v_t = \kappa Z V_* \left(1 - \frac{Z}{H}\right) \tag{2.3.4}$$

where, κ = von Kármán's constant; Z = vertical distance from bed; H = total depth of flow; and V_* = shear velocity. Substituting κ for 0.4 and integrating over the depth of flow, yields the following expression

$$\overline{v_t} = 0.067 H V_* \tag{2.3.5}$$

Although this equation is for the kinematic eddy viscosity in the vertical direction, a similar relationship is applicable to obtain the transverse mixing. Fisher et al. (1979) found that the values of $\overline{v_t}/(HV_*)$ for the straight uniform channels generally have values between 0.1 and 0.2. For practical use in natural channels, the curvature and irregular geometry tend to increase the value of $\overline{v_t}/(HV_*)$ to 0.6±0.3. Higher values are expected if the flow encounters sudden geometrical changes, such as sharp curves and side wall irregularity.

2.4. Wall Boundary Conditions

Since lateral shear stress is closely related to viscous effects on the wall, wall boundary conditions are discussed here. The viscous effects are significant only for the region which is very close to the wall. Following this assumption, Launder and Spalding (1974) proposed the wall function approach for the treatment of the wall boundary conditions.

Since most of the turbulent flow regions have high Reynolds number, turbulence models were developed for the flow problems outside of the viscous sublayer. The relationship between the distance from the wall y, kinematic viscosity ν, and longitudinal shear velocity V_*, is normalized and often taken (Rodi, 1984) as

$$30 \le \frac{yV_*}{\nu} \le 100 \tag{2.4.1}$$

Since the primary shear stress and primary shear velocity are related to the logarithmic law of the wall, either of them can be specified as the boundary condition for the x-momentum equation. Shamber and Larock (1981) specified primary shear stress at the virtual wall for the x-momentum equation as

$$\frac{\tau}{\rho} = -V_*|V_*| = \frac{-\kappa^2}{\left(\ln E\frac{yV_*^2}{\nu}\right)}|U|U \tag{2.4.2}$$

$$V_* = \frac{\kappa U}{\ln\left(E\frac{yV_*}{\nu}\right)} \tag{2.4.3}$$

where, E = a parameter reflecting roughness of the wall.

Naot (1984) expressed the primary shear in terms of the velocity U using the logarithmic law. The U velocity component is computed from Equation (2.4.3), assuming that the shear velocity is known. From this U value, the shear stress is updated in an iterative manner until convergence is achieved.

For a smooth wall, Naot (1984) uses $E = 9.0$ and for the rough walls,

$$E = \frac{e^{\kappa B}}{\left(K_s\frac{V_*}{\nu}\right)} \tag{2.4.4}$$

where, B = 8.5, and K_s is the roughness height. The values of B for the entire turbulence regime, Yalin and Krishnappan and Lau (1986) developed following equation:

$$B = (5.5 + 2.5 \ln R) \exp\{-0.217 (\ln R)^2\} + 8.5 (1 - \exp\{-0.217 (\ln R)^2\}) \qquad (2.4.5)$$

where, $R = \left(\frac{V_* K_s}{\nu} \right)$.

Shamber and Larock (1981), Naot and Rodi (1984), and Naot et al. (1993) take the boundary conditions for the velocity normal to the wall as zero. Therefore, the stresses normal to the wall do not need to be specified.

2.5. Turbulence Models

2.5.1. One-equation models

Turbulence models have been proposed, which employ transport equations for turbulence quantities. The simplest turbulence model is the one-equation model that expresses the eddy viscosity coefficient as a function of the turbulence kinematic energy, k, and characteristic length scale, L, of the turbulence flow. The eddy viscosity can be computed as

$$\nu_T = c'_\mu \sqrt{k} L \qquad (2.5.1)$$

where, c'_μ = an empirical coefficient. This formulation relates the eddy viscosity to the velocity scale, $\sqrt{k}$, and the length scale, L, that is related to the large-scale turbulence motion. This is called as the Kolmogrov-Prandtl expression (Rodi, 1993). The length scale is determined empirically. Launder and Spalding (1972) gave some examples of various algebraic expressions for the length scale computations.

Morgan et al. (1977) used the finite element method for the analysis of turbulent coaxial jet flow using the mixing length viscosity model. The prediction from the model is shown to compare well with the experimental results and finite difference based model. Taylor et al. (1978) applied finite element method to the two-dimensional, incompressible pipe flow and free shear flow problems, using one-equation turbulence model to determine the turbulent eddy viscosity coefficient. Using a similar one-equation model, Thomas et al. (1981) solved the problem of two-dimensional confined flow. He also used the finite element method for a flow past the backward facing step. For both cases, one-equation model showed good agreement between computed and measured values. The limitation of this model is the need to obtain the algebraic equation for the length scale. For this reason, the application of this model is restricted mainly to the shear-layer-flows.

With a precise algebraic description of the characteristic length, one-equation turbulence model was found to be an acceptable turbulent flow model. Therefore, a model using Prandtl's mixing length theory may be given consideration to simulate the turbulent flow motion, since it requires smaller effort to develop.

2.5.2. Two-equation models

The difficulty in finding the suitable length scale led the advancement from one-equation model to two-equation model in which transport of the turbulence length scale also accounted. The two-equation turbulent model has shown great possibilities in the fields of mechanical and aerospace engineering. This model has been introduced and used for simulations on the flow motion in the open channel. Rodi (1993) concluded in his state-of-the-art review, that the turbulent kinetic energy, k, and the dissipation rate of turbulent energy, ε, is universal and well suited for applications in hydraulics problems. By dimensional analysis, since the dissipation rate, ε, has a dimension of $k^{1.5}/L$, the parameter k-ε is found to have equivalent dimension of k-L. If the variables k and ε are computed, the kinematic eddy viscosity can be obtained as

$$\nu_T = c_\mu \frac{k^2}{\varepsilon} \tag{2.5.2}$$

where, c_μ = an empirical constant.

Each of these parameters is computed by solving the transport equations simultaneously. Applications of the k-ε model for two-dimensional turbulent flows are discussed by many researchers. McGuirk and Rodi (1978) used k-ε model for depth averaged open channel flow as well as heat transfer. Rastogi and Rodi (1979) employed k-ε model in computing three-dimensional flow and depth averaged open channel flow. In their formulation of transport equation, terms that account for the production and dissipation of turbulence due to bottom shear stresses are also included. However, it should be noted that the terms that arise due to vertical distributions of velocities are neglected in the depth averaged model. Durst and Rastogi (1979) carried out the computation of shear flows, and Raithby et al. (1978) used laterally averaged k-ε model to simulate rectangular depression.

Taylor et al. (1981) solved problem of backwater-facing step using the FEM employing the two-equation model of turbulence. Schamber and Larock (1981) predicted velocity distributions in sediment basins using k-ε turbulent model, using the rigid-lid assumption along the free surface. They employed slip boundary conditions for sidewalls and wall boundary conditions for the bottom of the sediment basins. Schamber (1982) discussed finite element method formulation in the analysis of laterally averaged flow of the sediment basin using the k-ε turbulence model. Finnie and Jeppson (1991) used simplified k-ε turbulent finite element model to investigate flow motions under the sluice gate. They used q-r equations (q is the square root of turbulent kinetic energy, $\sqrt{k}$, and r is the square root of dissipation rate, $\sqrt{\varepsilon}$), which is a variant of Smith's q-f model (1984 a&b). The turbulent viscosity terms are expressed using the relationship

$$\nu_T = c_\mu \frac{k^2}{\varepsilon} = c_\mu \frac{q^4}{r^2} \tag{2.5.3}$$

Two-equation turbulence models assume that the state of turbulence is characterized by length and velocity scales, which can be related each other using Prandtl mixing length expression or other formulations. These models imply isotropic eddy viscosity. Also, higher order models that do not use eddy viscosity concept were proposed and employed in various flow conditions.

2.6. Finite Element Method for Fluid Flow

The finite element method (FEM) is a numerical analysis technique used for obtaining approximate solutions to a wide variety of engineering problems. Although it is originally devised for analysis of structural engineering problems, FEM has developed to be one of the most effective tools for evaluating a wide range of problems in continuum mechanics. This development has been led by advancements in high-speed digital computers.

In the study of numerical modeling of open channel flows, variations in water surface elevation and velocity distributions in horizontal spatial dimensions are of great importance. The finite element method has been applied to fluid-flow problem and it is one of the ideal techniques for modeling two-dimensional flow motions in the complex geometrical domain. The finite element turbulent flow model solving the two-dimensional Navier-Stokes equations provide the user great advantages in defining boundary conditions.

Many researchers have done numerical studies on the flow motion using the finite element method. King (1976), Cooley and Moin (1976), and Keuning (1976), solved one-dimensional Saint-Venant equation for the hydrodynamic analysis of the open channel flow. Despite their successful attempts, their computations showed that, at least for the one-dimensional case, the existing finite difference schemes were overall superior when compared with the finite element. Hughes et al. (1978, 1979) used penalty function in solving various flow problems. They solved Navier-Stokes equations combining the bilinear interpolation for velocity with one quadrature point integration for the penalty term. Gray and Linch (1979), for the analysis of tidal flows, used unsteady finite element model in which time-variable terms were accounted for by using semi implicit scheme for unsteady terms. Zienkiewicz and Heinrich (1979) employed penalty function to analyze the shallow water flow problems under the assumption that Navier-Stokes equations are equivalent to steady shallow-water equations with pressure corresponding to depth.

For the treatment of computational oscillations, the upwind finite element scheme has been proposed and applied. Most of oscillations are encountered in the convection dominated flows due to higher Peclet or Reynolds numbers. Heinrich et al. (1977) applied the upwind approach to two-dimensional convection and diffusion equations. Brooks and Hughes (1982) presented the general framework on the upwind scheme for its application to the Navier-Stokes equations. Katopodes (1984) solved one and two-dimensional unsteady shallow wave equations employing dissipative Galerkin scheme by adapting Dendy's (1974) approach, which introduced an artificial diffusion that can be selectively applied to the modeling of river flow (Chaudhry, 1993).

For the finite element upwinding scheme, there is considerable controversy between finite element researchers. Advocates of upwinding scheme claim that the procedure does not result in accuracy losses that can be encountered in the application of finite difference upwind scheme. On the contrary, those who prefer standard Galerkin method state that finite element upwind scheme causes loss of accuracy. Gresho and Lee (1981) recommended that finer mesh be employed for the construction of mesh domain to avoid oscillations resulting from numerical computations. Despite the controversy between each side's, the upwind finite element implementation seems to have become a standard scheme for the computational fluid dynamics. Berger and Stockstill (1995) produced a 2D finite element model using an extension of the SUPG (Streamlined Upwind Petrov-Galerkin) concept for shallow water equation and applied their model to high velocity channels. Through comparison with flume data, 2D supercritical flow in contractions was demonstrated.

For three-dimensional finite element model, Li and Zhan (1993), using the standard Galerkin method, proposed a multilayer semi-implicit finite element model in which nine-node Lagrangian quadratic isoparametric elements were employed for spatial discretization in the horizontal domain. Li and Zhan (1998) improved their previous model using three-node Lagrangian interpolation for vertical gradients of the vertical velocity components instead of integrating vertically the two horizontal momentum equations. They applied their model to analyze the stratified sea flow.

2.7. Abutment Studies

In abutment studies, the main objective is to predict the maximum depth of scour. Usually, scour at bridge sites can be grouped into 3 major types. They are: general scour, contraction scour, and local scour. The combination of these three different kinds of scours yields the final scour depth around bridge abutments. The local scour is commonly defined as the scour around an obstruction. Abutment scour is a complex three-dimensional physical phenomenon that has been studied by many researchers in the last few decades.

2.7.1. Laboratory studies for investigating flow around abutments

A few of notable past studies on the abutment scour were done by Ahmad (1953), Liu et al. (1961), Garde et al. (1961), Lausen (1963), Gill (1971), Khiereldin (1995), Abdeldayem (1996), and Nosh (1996). Past studies on the flow around abutments are based on study of flow motion around groins and dikes that can be viewed as very thin abutment. Awazu (1967) conducted an experimental study using shear stress around the spur dikes using 12 different combinations of flow conditions. The opening ratio in his experimental study varied between 0.10 and 0.40 with different Froude numbers of 0.488, 0.508, and 0.526. Zaghloul (1974), and Rajaratnam and Nwachukwu (1983a) conducted laboratory studies on the flow motion around spur dikes. Zaghloul (1974) extended his experimental results to the numerical study. Rajaratnam and Nwachukwu (1983 a&b) presented a summary of the relationship between the ratio of U/U_o and x/a for two different sets of runs where, $x =$ longitudinal distance along the flume, and $a =$ spur dike protrusion length.

Kwan (1984) investigated the effect of skewness angle of the abutment on the resulting scour. Kwan compared maximum scour depth which can be obtained from different skewness angles for a constant projection ratio. During his experiments, Kwan used 3 different abutments which made 45°, 90°, and 135° angles with flow. From his analysis of the velocity distribution, the maximum velocity occurred at the upstream corner of the abutment, where the maximum scour hole was found.

Studies by Melville (1992) have shown that the local scour takes place at the abutment and spur dikes are similar. Melville reported that in many cases the bridge failure is directly related to abutment scour. Lim (1997) presents scour prediction formula from the semi empirical analysis to determine the maximum local clear-water scour depth at the abutment on the based on the continuity equation, scour geometry, and the law of resistance in the alluvial channel. Melville (1997) summarized many of the results from the pier and abutment scour research. Most of the recent data in his study were collected from Dongol (1994). Molinas et al. (1998) derived shear amplification equation based on experimental results using vertical wall abutments. Their experimental results were collected from 15 different cases which included 3 different projection ratios and different approach flow velocities. They concluded that high shear stress occurred at the upstream nose of the abutment and local scour around the abutments is related with increased flow velocity and shear intensity.

Ahmed and Rajaratnam (2000) presented the results from an experimental investigation of skewed three-dimensional flow around a bridge abutment which was not a vertical wall abutment. They reported that the shear stress was amplified 3.63 times the approach shear at the nose of the abutment. The use of the term "skewed" by Ahmed and Rajaratnam referred to a skewed abutment wall as opposed to a vertical wall. For the overtopping flow over an abutment, Kuhnle et al. (1999) investigated and reported about the geometry of scour holes developed around spur dikes using 2 different 90 degree spur dikes varying in length. They concluded that the shape of the spur dike, rather than its length, plays an important role in the development of maximum scour depth for overtopping flows.

2.7.2. Numerical studies for investigating flow around hydraulic structures

In abutment studies, the zone of interest is located at the contracted region where protection against scour is needed. Numerical and experimental studies of the flow distribution in this region were interested in the designing aspect of hydraulic structures. According to the laboratory work and numerical model simulation by Zaghloul (1974), the maximum velocity and vorticity were found in the nose region of a dike.

Tingsanchali and Maheshwaran (1990) used two-dimensional depth-averaged k-ε turbulent model for the analysis of flow around groins. The governing equations were solved using a hybrid finite difference scheme. For improved shear stress computations, streamline correction was incorporated for the curvature of streamlines to compute shear stress distributions around the tip of groins by adapting a 3-D correction for roughness effects. They modified Johnston's (1960) 3-D correction and it is given as a function of the turning angle. Tingsanchali and Maheshwaran presented comparisons between their numerical results and an experimental study done by Rajaratnam and Nwachukwu (1983). Mayerle et al. (1995), using 3-dimensional finite element model, compared reattachment length by applying different definitions of eddy viscosity closure. They concluded that the viscosity approach based on mixing length and the assumption of the local equilibrium for the kinetic energy produced wake length in good agreement with the measurements.

Ouillon and Dartus (1997) investigated flow around groins using three-dimensional k-ε model adopting a porosity method to track the free surface. They presented comparisons between the results for rigid-lid and depth-averaged models. The discrepancy between the two models was on the length of reattachment zone behind the groin. The free surface assumption for the model modification is following Celik and Rodi (1984)'s work.

Biglari and Sturm (1998) conducted numerical modeling of flow around bridge abutments located on the floodplain of a compound open channel using a two-dimensional, depth averaged, k-ε model. The model uses finite difference scheme with a staggered grid to solve the governing turbulence equations. Molinas and Hafez (2000) derived formulations for velocity amplification factor as a function of abutment protrusion ratio using a two-dimensional finite element model which solves Navier-Stokes equations. So far, all of the previous studies were done for abutments placed perpendicular to flow direction. Although Kwan (1984) presented an experimental study which was for skewed abutments, his research covered only 3 different skewness angles and investigated only the maximum scour. For a more detailed study of skewness, a numerical modeling study is needed.

2.8. Review of the Sediment Transport Theories

2.8.1. Logarithmic velocity profile

In the case of laminar flow, the shear stress is obtained directly from the fluid viscosity and velocity gradient. Logarithmic velocity distribution can be used to define the relationship between the main flow velocity and the boundary shear. The mathematical expression of the shear stress for the laminar flow is given as

$$\tau = \mu \frac{du}{dz} \tag{2.8.1}$$

where, τ is shear stress, μ is laminar fluid viscosity, u is velocity component in the direction of main flow, and z is normal distance from the boundary

For turbulent flows, instead of using only laminar fluid viscosity, the turbulent shear stress based on turbulent viscosity can be included. Using the Prandtl's definition of turbulent viscosity as

$$\mu_t = \rho l_m^2 \left| \frac{du}{dz} \right| \tag{2.8.2}$$

Therefore, the total shear stress can be given as follows

$$\tau_{total} = \mu \frac{du}{dz} + \rho\, l_m^2 \left(\frac{du}{dz} \right)^2 \tag{2.8.3}$$

where, ρ is the fluid density, $du/dz =$ velocity gradient at a distance y from the solid surface, $l_m =$ characteristic length of the mixing length, and μ_t is turbulent fluid viscosity.

In turbulent flows, shear stress of the laminar flow is negligible compared to the turbulent counterpart. Prandtl's mixing length theory was advanced by von Kármán who attempted to relate l_m to the mean velocity profile using the following formula

$$l_m = \kappa \left| \frac{du/dz}{d^2u/dz^2} \right| \tag{2.8.4}$$

where, κ is a universal constant equal to 0.40. Using Pandtl's assumption for the mixing length as $l_m = \kappa y$ for turbulent flows, substituting this value into Equation (2.8.2), shear stress becomes

$$\tau = \rho \kappa^2 z^2 \left(\frac{du}{dz} \right)^2 \tag{2.8.5}$$

Rearranging the above equation with respect to the velocity term

$$du = \frac{1}{\kappa} \sqrt{\frac{\tau}{\rho}} \frac{dz}{z} \tag{2.8.6}$$

Integration of both sides of above equation leads to

$$u = 2.5 \sqrt{\frac{\tau}{\rho}} \ln \frac{z}{z_o} \tag{2.8.7}$$

The shear stress, τ, in the region close to the wall remains virtually equal to the boundary shear stress, $\tau = \rho V_*^2$, where the shear velocity, V_*, is defined as

$$V_* = \sqrt{\frac{\tau}{\rho}} = \kappa z \left(\frac{du}{dz} \right) \tag{2.8.8}$$

Equation (2.8.7) can be rewritten as

$$\frac{u}{V_*} = \frac{1}{\kappa} \ln \frac{z}{z_o} \tag{2.8.9}$$

2.8.2. Smooth and rough boundary surface

From Equation (2.8.9) the velocity in the turbulent region follows von Kármán's logarithmic velocity distribution law. The parameter z_o was found to be related to the boundary roughness. Nikuradse (1936) defined z_o for the pipe flows as

$$z_o = \frac{m\nu}{V_*} \tag{2.8.10}$$

where, m is a constant that is equal to $1/9$ for smooth surfaces, and is equal to $1/30.2$ for rough surfaces; and ν is the kinematic viscosity

After substituting Equation (2.8.10) into Equation (2.8.9) and rearranging, the following equations are obtained for smooth and rough boundary surfaces, respectively.

$$\frac{U}{V_*} = \frac{2.3}{\kappa}\log\left(\frac{9zV_*}{\nu}\right) = 5.75\log\left(\frac{zV_*}{\nu_m}\right) + 5.5 \tag{2.8.11}$$

$$\frac{U}{V_*} = \frac{2.3}{\kappa}\log\left(\frac{30z}{k_s}\right) = 5.75\log\left(\frac{z}{k_s}\right) + 8.5 \tag{2.8.12}$$

where, k_s is the roughness height known as Nikuradse sand roughness.

Keulegan (1938) derived the following equation to obtain the velocity profile based on the Nikuradse's data

$$\frac{U}{V_*} = 5.75\log\left(\frac{mR}{z_o}\right) + C \tag{2.8.13}$$

After substituting the value of z_o from Equation (2.8.10), and integrating the above equation over flow depth h, the expression for mean flow velocity profiles can be written for smooth and rough boundaries as:

$$\frac{U}{V_*} = 5.75\log\left(\frac{u_*h}{\nu_m}\right) + 3.25 \quad \text{(Smooth)} \tag{2.8.14}$$

$$\frac{U}{V_*} = 5.75\log\left(\frac{h}{k_s}\right) + 6.25 \qquad \text{(Rough)} \tag{2.8.15}$$

2.8.3. Laminar sublayer and shear Reynolds number

In turbulent flows, the laminar sublayer exists very close to the channel boundary where viscous shear stresses are dominant. The boundary shear stress at this region can be given as

$$\tau = \rho_m V_*^2 \tag{2.8.16}$$

From Equation (2.8.1), assuming that the velocity at the most outside of this layer is u_δ, the shear stress at this point will be

$$\tau = \mu_m \frac{u_\delta}{\delta} = \rho_m V_*^2 \tag{2.8.17}$$

where, δ = the thickness of laminar sublayer

In dimensionless form, Equation (2.8.17) can be rewritten as follows

$$\frac{u_\delta}{V_*} = \frac{V_*\delta}{\nu_m} \tag{2.8.18}$$

Since the flow velocity u of the turbulent profile must equal to the velocity u_δ of the laminar sublayer, after substituting Equation (2.8.13) into (2.8.14) and solving for thickness δ leads to

$$\delta = \frac{11.6\nu_m}{V_*} \tag{2.8.19}$$

The particle shear Reynolds number Re_* is defined by the product of shear velocity and grain size over the kinematic viscosity of the mixture of fluid and sediment ν_m,

$$\mathrm{Re}_* = \frac{V_* d_s}{\nu_m} \tag{2.8.20}$$

Hydraulically smooth turbulent flow is determined when the height of the boundary roughness, which is characterized by the sediment size d_s, is much smaller than the laminar sublayer thickness. That is, when

$$3d_s < \delta \text{ or } \mathrm{Re}_* = \frac{V_* d_s}{\nu_m} < 4 \tag{2.8.21}$$

Likewise, for the hydraulically rough turbulent flows, the grain size d_s is much bigger than the laminar sublayer thickness. That is, in the case

$$d_s > 6\delta \text{ or } \mathrm{Re}_* = \frac{V_* d_s}{\nu_m} > 70 \tag{2.8.22}$$

and the transition zone corresponds to the following condition.

$$\frac{\delta}{3} < d_s < 6\delta \text{ or } 4 < \mathrm{Re}_* < 70 \tag{2.8.23}$$

2.8.4. Roughness coefficient for resistance to flow

Most common parameters for describing the resistance to steady uniform flow are: Chézy coefficient C, Manning's n, and the Darcy-Weisbach friction factor f. The relationship between these terms and the flow depth, h, is

$$C = \sqrt{\frac{8g}{f}} = \frac{R^{1/6}}{n} \quad \text{(in Metric unit)} \tag{2.8.24a}$$

$$C = \sqrt{\frac{8g}{f}} = \frac{1.49R^{1/6}}{n} \quad \text{(in English unit)} \tag{2.8.24b}$$

where, R is the hydraulic radius and g is the gravitational acceleration. For wide channels, R becomes equal to h.

In plane bed channel, assuming that the total channel bed resistance is solely given by the grain resistance, the grain Chézy coefficient is denoted as C'; the Darcy-Weisbach grain friction factor is denoted as f'; and the grain manning coefficient as n'. Using the grain parameters, Equation (2.8.24) can be given as

$$C' \equiv \sqrt{\frac{8g}{f'}} \equiv \frac{R^{1/6}}{n'} \quad \text{(in Metric units)} \tag{2.8.25a}$$

$$C' \equiv \sqrt{\frac{8g}{f'}} \equiv \frac{1.49R^{1/6}}{n'} \quad \text{(in English units)} \tag{2.8.25b}$$

Assuming the total resistance of the channel assumed to equal to the grain resistance, the roughness variables for channel bed can be given as $\tau = \tau'$, $u_* = u_*'$, $C = C'$, and $n = n'$.

Strickler (1923) defined Manning's n' as a function of sediment particle size as

$$n' = \frac{d^{1/6}}{21.1} \tag{2.8.26a}$$

where, $d =$ mean diameter of uniform sand in meters; or

$$n' = \frac{d^{1/6}}{25.7} \tag{2.8.26b}$$

where, $d =$ mean diameter of uniform sand in ft.

Since Equation (2.8.26a) and Equation (2.8.26b) both were obtained from a small laboratory flume with uniform sand, they should not be applied directly to the natural river with nonunifom bed material. Meyer-Peter and Muller (1948), considered a sand mixture, and modified Stickler's formula as

$$n' = \frac{d_{90}^{1/6}}{26} \tag{2.8.27}$$

where, d_{90} = sediment diameter (in meter) for which 90% of the mixture is finer by dry weight. Equation (2.8.27) can be used to approximate Manning's coefficient when the bed is not covered by cobbles or armored. Lane and Carlson (1953) in their study of the San Luis Valley canal suggested that

$$n' = \frac{d_{75}^{1/6}}{39} \tag{2.8.28}$$

where, d_{75} = sediment diameter (in inch) for which 75% of the mixture is finer by dry weight.

2.8.5. Critical shear stress

When the fluid exerts hydrodynamic forces on sediment particles, it sets the particles into a state of motion. For noncohesive materials, the resisting force is closely related to the particle weight. When the hydrodynamic momentum forces acting on a single particle exceed the resisting moment of force balance, the threshold condition is initiated and the particle is at the incipient motion state.

In turbulent flows, the hydrodynamic forces around the sediment yield the lifting force. Since the lifting force is proportional to the drag force, the buoyancy force acts in the vertical direction opposite to the particle weight. If the submerged weight of the particle is equivalent to the hydrodynamic force, the ratio of these two terms can be expressed using the dimensionless shear stress. This is the Shields parameter and can be written as

$$\tau_* = \frac{\tau}{(\gamma_s - \gamma_m)d_s} = \frac{\rho_m V_*^2}{(\gamma_s - \gamma_m)d_s} \tag{2.8.29}$$

where, τ = boundary shear stress, V_* = shear velocity, γ_s = specific weight of a sediment particle, γ_m = specific weight of the fluid mixture, d_s = particle diameter.

The critical value of the Shields parameter is dependent not only on the particle weight but also flow conditions. Therefore, the ratio of sediment size to the laminar sublayer thickness and grain shear Reynolds number, Re_*, also has to be considered. Shields (1936) determined the beginning of motion by measuring sediment transport for the values of τ_*. He found that the threshold condition is as large as the critical value and these values are extrapolated until the sediment transport discontinues.

Yalin and Karahan (1979) using the grain size d_s, obtained the modified Shields diagram in Figure 2.1.

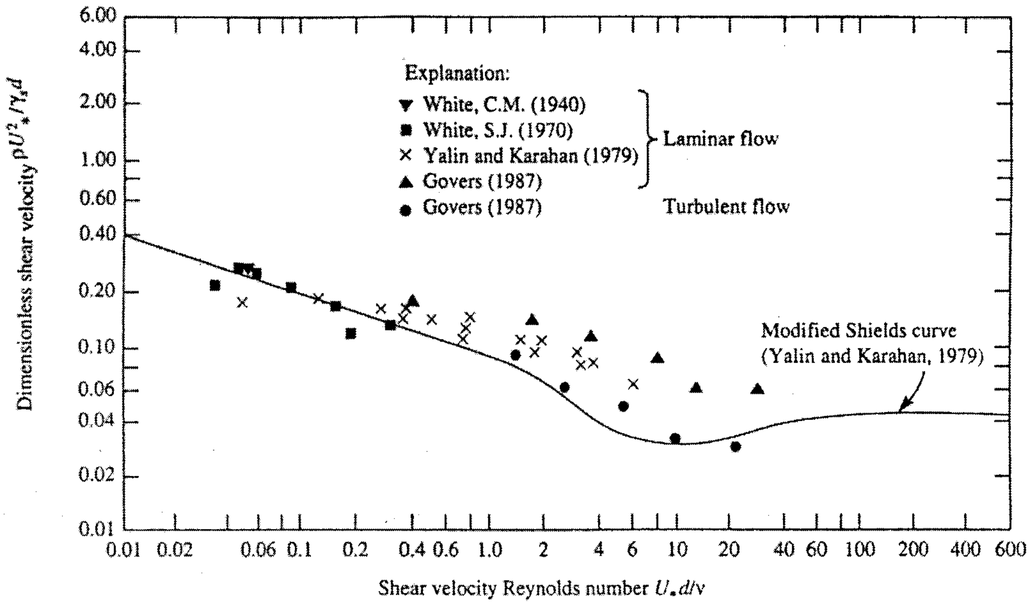

Figure 2.1 Modified Shields diagram (After Govers, 1987).

From Equation (2.8.29), since shear velocity, V_*, appears both in the Shields parameter and in the particle Reynolds number, Re_*, after mathematical manipulation, it is possible to replace Shields diagram with the dimensionless particle diagram which is shown in Figure 2.2. The critical values of Shields parameter τ_c also can be approximated as follows (Julien, 1995)

$$\tau_c = 0.5\tan\phi \qquad \text{when } d_* < 0.3$$

$$\tau_c = 0.25 d_*^{-0.6}\tan\phi \text{ when } 0.3 < d_* < 19 \tag{2.8.30}$$

$$\tau_c = 0.013 d_*^{0.4}\tan\phi \text{ when } 0.3 < d_* < 19$$

$$\tau_c = 0.06\tan\phi \qquad \text{when } d_* > 50$$

where, $d_* = d_{50}\left[\frac{(G-1)g}{\nu_m}\right]^{1/3}$, and $\phi =$ Angle of repose, which is usually given as 30° for sands.

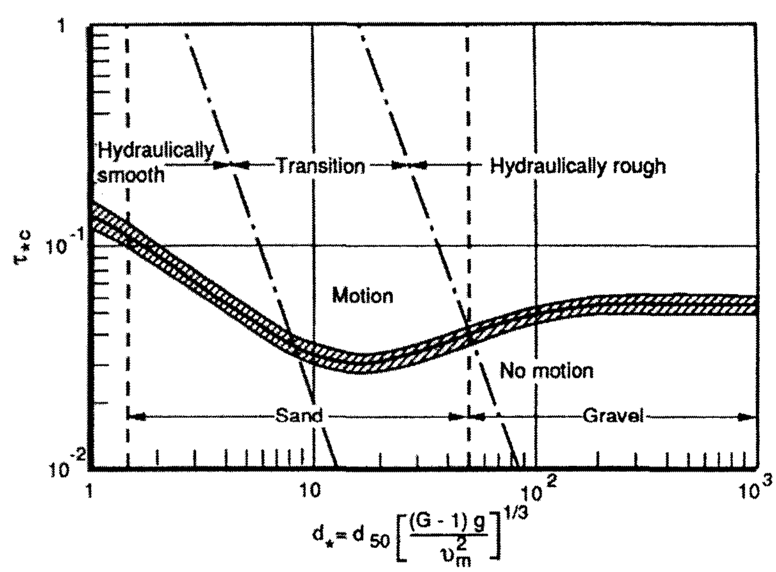

Figure 2.2 Particle motion diagram (After Julien, 1995).

2.8.6. Theoretical approach for bed form analysis

Research on the prediction of bed forms involves both theoretical and empirical approaches. This study is based on recent work that mainly covers theoretical approaches. From the sediment continuity equation, theoretical approach can be explained from the flow over dunes, which is shown in Figure 2.3. The governing equation is given as

$$\gamma_s \frac{\partial z}{\partial t} + \frac{\partial q_s}{\partial x} = 0 \qquad (2.8.31)$$

Exner (1925) assumed that

$$q_s = AU_b \qquad (2.8.32)$$

where, A is constant and U_b is the flow velocity near the bed.

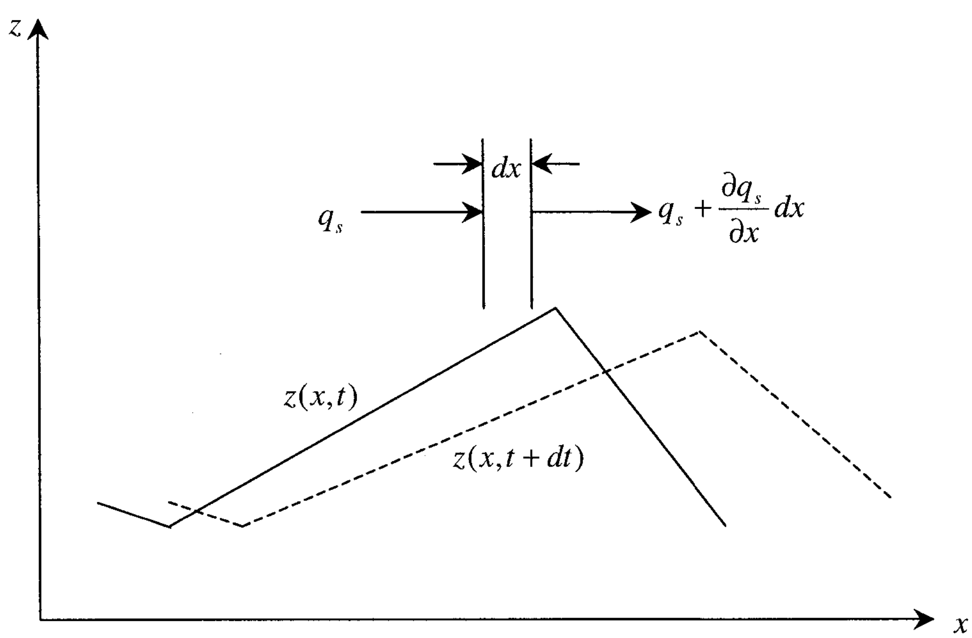

Figure 2.3 Typical bed form transition in downstream direction.

substituting Equation (2.8.32) into Equation (2.8.31) yields

$$\gamma_s \frac{\partial z}{\partial t} + A \frac{\partial U_b}{\partial x} = 0 \tag{2.8.33}$$

The above equation is known as Exner's (1925) equation.

Tanguy et al. (1989) predicted bed elevation distributions for a channel with a dike perpendicular to flow. Solving the two-dimensional shallow water equation along with sediment continuity equation, Tanguy et al. developed a numerical model using the finite element method. The governing equation except the unsteady term is diagonalized using modified shape function which is valid only for triangular element to ease matrix manipulation. Brørs (1999) conducted a numerical simulation of scour development under the submerged pipelines. The flow distributions are computed using finite element rigid-lid model by solving Navier-Stokes turbulent flow equations with k-ε closure and using the finite difference scheme, the following sediment continuity equation is solved.

$$\frac{\partial z}{\partial t} = \frac{1}{1-n}\left[-\frac{q_i}{\partial x_i} + D - E \right] \qquad i = 1, 2 \tag{2.8.34}$$

where, n is porosity, D is the rate of which sediment is deposited, and E is the rate of which sediment erosion. Although flow computation is done in the two-dimension domain using x-z coordinate system, sediment continuity equation is assumed and solved in one-dimensional domain. Written in finite difference equation and the new bed level p at time n+1 will be given as follow

$$z_p^{n+1} = z_p^n + \frac{1}{1-n}\left[-\frac{q_{p-1}^n - q_p^n}{x_{p-1}^n - x_p} + D_p^n - E_p^n \right]\Delta t \tag{2.8.35}$$

where, Δt is morphological time step which is much longer than the unsteady flow time step.

2.8.7. Bed load transport equations

Bed load transport occurs when the shear stress applied on the bed material exceeds the critical shear stress. Bed load transports the coarse, noncohesive bed materials such as sand and gravel in contact with a thin layer near the bed, while fine materials such as silt and clay particles are set into the suspension. The thin layer is called the bed layer. Studies on bed load transport are done either using a deterministic or a statistical approach. Duboys and Meyer-Peter & Muller proposed deterministic methods, and Kalinske and Einstein developed statistical methods. In this study, only deterministic methods are considered and incorporated in the mathematical model.

Duboys' Equation (1879)

Based on the concept that the sediment moves in a thin layer along the bed, the bed shear stress is always bigger than the critical shear stress to initiate transport motion. The unit of bed material in motion per unit width and time is in ft^2/s

$$q_b = \frac{0.173}{d_s^{3/4}} \tau(\tau - \tau_c) \tag{2.8.36}$$

where, d_s = the diameter of particles (in mm); τ = is the boundary shear stress (lb/ft^2); and the critical shear stress, τ_c, is given as follows

$$\tau_c = 0.0125 + 0.019 d_s \ (lb/ft^2) \tag{2.8.37}$$

Meyer-Peter and Muller's Equation (1948)

This equation is developed based on the median sediment size d_{50}. Chien (1956) proposed the reduced form as

$$\frac{q_b}{\sqrt{(G-1) g d_s^3}} = 8(\tau - \tau_c)^{1.5} \tag{2.8.38}$$

This equation is most appropriate for the channel with large width-depth ratios. The corresponding dimensional formulation is given as

$$q_b \approx \frac{12.9}{\gamma_s \sqrt{\rho}} (\tau - \tau_c)^{1.5} \text{ (lb/ft}^2\text{)} \tag{2.8.39}$$

van Rijn Equation (1984)

van Rijn proposed a method to predict the type of bedforms and their dimensions in the lower flow region. This method is based on the analysis of flume and field data. van Rijn assumed that the bedforms and their dimensions are controlled mainly by the bed load transport. He also suggested describing the bed load transport as a function of a dimensionless particle diameter, d_*, and a transport stage parameter, T, as follows

$$d_* = d_{50}\left[(s-1)\frac{g}{v_m^2}\right]^{\frac{1}{3}}, \; T = \frac{\tau - \tau_c}{\tau_c} \tag{2.8.40}$$

The amount of the sediment is computed as

$$q_b = 0.053\left[\left(\frac{\rho_s}{\rho} - 1\right)g\right]^{0.5} d_{50}^{1.5} d_*^{-0.3} T^{2.1} \tag{2.8.41}$$

Assuming a reasonable value for k_s as $3d_{90}$, the relationship can be expressed by the following mathematical expression

$$C' = \sqrt{\frac{8g}{f'}} = \frac{2.3}{\kappa}\sqrt{g}\log\left(\frac{12.2R}{3d_{90}}\right) \cong 5.75\sqrt{g}\log\left(\frac{4h}{d_{90}}\right) \tag{2.8.42}$$

2.8.8. Suspended load transport

While coarse material transport occurs near the channel bed surface, finer materials such as silts and clay are brought into suspension when the turbulent velocity fluctuations are sufficiently large. Thus, suspended load transport usually occurs above the layer of bed load transport.

The Governing Equation

The concept of concentration is employed and commonly used in measuring the amount of suspended sediment. In hydraulic engineering, flux-averaged concentration with the amount of discharge Q is used to represent the mass flux passing through the area of a certain cross section, A, as

$$C_f = \frac{1}{Q}\int_A CUdA \qquad (2.8.43)$$

where, C_f = the flux-averaged concentration, U = averaged flow velocity, and Q = flow discharge

The governing equation for the suspended load is derived from the sediment continuity equation. The rate of mass change equals the difference of mass fluxes across the area of the control volume. The relationship is

$$\frac{\partial C}{\partial t} + \frac{\partial q_{sx}}{\partial x} + \frac{\partial q_{sy}}{\partial y} + \frac{\partial q_{sz}}{\partial z} = Q \qquad (2.8.44)$$

where, C is the averaged sediment concentration inside of the control volume; q_{sx}, q_{sy}, q_{sz} are the mass fluxes through the area of control volume; and Q is the rate of sediment per unit volume supplied from an external source. The units of C are not important as long as they are consistent with those of q_s and Q.

There are three types of fluxes cross through the area of control volume. The types are advective, diffusive, and mixing fluxes. These are expressed by the following equations.

$$q_{sx} = UC - (D+\varepsilon_x)\frac{\partial C}{\partial x}$$
$$q_{sy} = VC - (D+\varepsilon_y)\frac{\partial C}{\partial y} \qquad (2.8.45)$$
$$q_{sz} = WC - (D+\varepsilon_z)\frac{\partial C}{\partial z}$$

where, D = molecular diffusion coefficient; ε_x, ε_y, ε_z = turbulent diffusion coefficient in x, y, and z direction, respectively.

The first terms in the right hand sides of Equation (2.8.45) represent the advective fluxes which describe the transport of sediment by velocity currents. The rate of mass transport per unit area is obtained from the product of sediment concentration and the velocity components, u, v, and w. Two additional fluxes must be considered in sediment transport. Molecular diffusion, D refers to the sediment particles scattering by random molecular motion following the Fick's law. Turbulent diffusion coefficients, ε_x ε_y and ε_z describe sediment perturbation due to the turbulent flow motion. After substituting Equation (2.8.45) to Equation (2.8.44), the governing equation describing the movement of suspended load is

$$\frac{\partial C}{\partial t} + \frac{\partial UC}{\partial x} + \frac{\partial VC}{\partial y} + \frac{\partial WC}{\partial z} = (D+\varepsilon_x)\frac{\partial^2 C}{\partial x^2} + (D+\varepsilon_y)\frac{\partial^2 C}{\partial y^2} + (D+\varepsilon_z)\frac{\partial^2 C}{\partial z^2} + Q \qquad (2.8.46)$$

The first time derivative term of Equation (2.8.46) represents for the mass change rate with respect to the time. The rest of the terms on the left-hand side that include velocity and sediment concentration, represent advection properties in x, y and z directions, respectively. The right hand side terms of Equation (2.8.46) are diffusion terms expressed by second derivatives with respect to the x, y, and z directions respectively; and the last term Q represents the source term.

Unlike Navier-Stokes equations, this equation can be easily solved because the equation is linear. This equation also has numerous applications in the field of sediment, contaminant transport and water quality problems. The properties of diffusion coefficients can be defined in two different types of flow conditions. In laminar flow, only the molecular diffusion exists and the turbulent mixing coefficients become zeros. For the turbulent flow, the turbulent mixing coefficients, ε_x, ε_y, and ε_z are much bigger than the molecular diffusion coefficient D so that in turbulent flows, the molecular diffusion term is negligible.

Definition of suspended load

Using the depth-integrated advection flux of sediment CU above the bed load transport thickness of a, the unit suspended sediment discharge q_s in streams or canals is determined from

$$q_s = \int_a^h CU \, dy \tag{2.8.47}$$

The corresponding total suspended sediment discharge Q_s is obtained from the integration of the unit suspended sediment discharge over the entire width of the channel as

$$Q_s = \int_{\text{width}} q_s \, dw \tag{2.8.48}$$

When expressing the amount of sediment in suspension passing through a cross section during a certain period of time, the definition of suspended load L_s can be given as

$$L_s = \int_{time} Q_s \, dt \tag{2.8.49}$$

While the units to describe the amount of bed load can be those of weight, mass, or volume, the units of suspended load are given by metric tons (1000kg).

The Rouse Equation

In steady equilibrium conditions, the net upward movement of sediment due to turbulence is balanced by the downward sediment movement due to the fall velocity. Assuming one-dimensional convection and diffusion equation in flow depth direction z,

$$\omega\frac{\partial C}{\partial z} = \varepsilon_z \frac{\partial^2 C}{\partial z^2} \tag{2.8.50}$$

Since the fall velocity can be given as, ω, after integration with respect to z, Equation (2.8.50) yields

$$\omega C + \varepsilon_z \frac{\partial C}{\partial z} = 0 \tag{2.8.51}$$

After integration from bed layer to water surface, Equation (2.8.51) will be given in terms of C as

$$C = C_a \exp\left(-\omega\int_a^z \frac{dz}{\varepsilon_z}\right) \tag{2.8.52}$$

The shear stress at a distance z above the bed is

$$\tau_z = \gamma S(h - z) = \tau\left(1 - \frac{z}{h}\right) \tag{2.8.53}$$

In turbulent flow, the shear stress can be given as

$$\tau_z = \varepsilon_m \rho \frac{dU}{dz} \tag{2.8.54}$$

where, ε_m is momentum exchange coefficient

Adapting von Kármán velocity distributions of Equation (2.8.8),

$$\frac{du}{dz} = \frac{V_*}{\kappa z} \tag{2.8.55}$$

Equations (2.8.50), (2.8.51), and (2.8.52) can be summarized as follows

$$\varepsilon_m = \kappa V_* \frac{z}{h}(h - z) \tag{2.8.56}$$

$$\varepsilon_z = \beta \kappa V_* \frac{z}{h}(h - z) \tag{2.8.57}$$

After substituting Equation (2.8.57) into Equation (2.8.51) and integrating from a to z

$$\int_a^z \frac{dC}{C} = -\int_a^z \frac{\omega dz}{\beta \kappa V_* (z/h)(h - z)} \tag{2.8.58}$$

The above equation can be solved as follows

$$\ln \frac{C}{C_a} = -\int_a^z \frac{(\omega / \beta \kappa V_*) h}{z(h - z)} dz \tag{2.8.59}$$

Finally, the concentration C can be found from the following equation

$$\frac{C}{C_a} = \left(\frac{h - z}{z} \frac{a}{h - a} \right)^{\mathrm{Ro} = \omega / \beta \kappa V_*} \tag{2.8.60}$$

where, C_a represents the reference sediment concentration at a reference elevation a above the bed elevation. The exponential value of Ro, referred to as Rouse number, defines the ratio of sediment properties to the hydraulic characteristics of the flow. In Equation (2.8.60), ω is fall velocity; β is momentum exchange coefficient; κ is von Kármán constant of 0.4; and V_* is shear velocity.

CHAPTER 3

3. HYDRODYNAMIC MODEL

In this chapter, using the finite element methods a two-dimensional hydrodynamic model is proposed and applied to analyze flow distribution in contracted reaches. The attention is focused on the flow distributions in the channel contraction formed by the skewed abutments. Proposed numerical model solves the steady state Reynolds flow of motion and continuity equations using the Petrov-Galerkin method. The notable difference between the standard Galerkin and Petrov-Galerkin method lies in the choice of the weighting function. That is, the weighting function of the standard Galerkin scheme is identical to the shape function, while that of the Petrov-Galerkin scheme is not. The Petrov-Galerkin scheme is corresponding to the upwind finite difference method in introducing the balancing diffusion terms to provide numerical stability. Through the comparison with the standard Galerkin method, this chapter explains the theoretical background and the derivation of the balancing diffusion terms.

After model verification using the experimental data, the model is applied and used for the flow distribution analysis. The investigation focuses on the velocity profile in the channel contraction and compares the maximum velocity variation due to the skeweness. In the model run, the skeweness angle of the abutment varies from 30° to 150°, with 10° increments for single and double abutment cases. After a series of model run, an analytical expression is derived to find the maximum velocity as a function of contraction ratio and skewness angle in channel contractions.

3.1. Basic Concept of Finite Element Method

The concept of the finite element method is that any approximate quantity can be obtained using piecewise smooth functions which is defined using numbers of elements. The smooth functions are called as shape or basis, which can be described by the value at number of points in its domain. The value is defined at nodes which connect adjacent elements. In the finite element solution, the nodal values are given as unknowns and interpreted through the assembly of the shape functions. The shape functions should be chosen to approximate variables as closely as possible and one order less partial derivative of the highest derivatives in the equation has to be continuous as well.

Using the chosen shape functions, the finite element equation can be established. In general, finite element equations obtained by using direct methods, variational methods, or weighted residual methods. Weighted residual methods are general scheme for linear and nonlinear partial differential equations which include collocation, least square, and Galerkin method. In all of these methods, a set of shape function including appropriate constants or functions can approximate the unknown variables. According to the selected constants or functions, the type of residual method is defined. A typical form of the partial differential equation can be given as

$$L(\phi) - f = 0 \tag{3.1.1}$$

where, L = the differential operator; ϕ = unknown field variable; and f = a known function of the independent variables.

The unknown variable, ϕ can be approximated using the shape function as

$$\phi \approx \tilde{\phi} = \sum_{i=1}^{m} N_i \phi_i \tag{3.1.2}$$

where, N_i = the shape functions; and ϕ_i = the unknown nodal variables.

If the approximation of the unknown value $\tilde{\phi}$ is substituted into Equation (3.1.1), the equation will not be satisfied due to the approximation. The trial function defined as

$$L(\tilde{\phi}) - f = R \tag{3.1.3}$$

where, R = the residual or error results from the approximating ϕ by $\tilde{\phi}$.

The method of weighted residuals tries to determine the m of unknown variables of ϕ_i in a way that the error R can be as small as possible over the entire computational domain (Huebner, 1982, pp. 108-111). To do so, multiplying the weighting function to the average of the error and make this weighted average zero over the entire computation domain, D. That is,

$$\int_D W_i \left[L(\tilde{\phi}) - f \right] dD = \int_D W_i R dD = 0 \tag{3.1.4}$$

According to the selection of the weighting functions, the difference of the weighted residual methods is determined. The most often used scheme to derive the finite element equation is Galerkin's method in which weighting function is as same as the shape functions, that is, $W_i = N_i$, for $i = 1, 2, 3, \ldots, m$. One of the alternative implementation is the Petrov-Galerkin method which employs different weighting function than the shape function, as $W_i \neq N_i$. Once the weighting functions are specified, a set of m simultaneous equations has to be solved for the unknown variables as

$$\int_D W_i \left[L(\tilde{\phi}) - f \right] dD = 0 \,;\ i = 1, 2, 3, \ldots, m \tag{3.1.5}$$

$$\text{where, } \tilde{\phi} = \sum_{i=1}^{m} N_i^{(e)} \phi_i^{(e)} \tag{3.1.6}$$

in which, the subscript (e) denotes the functions or variable of the element and n is the number of unknown nodal variables assigned to the element. Equation (3.1.6) can be substituted to Equation (3.1.4) to yield

$$\int_{D^{(e)}} W_i^{(e)} \left\lfloor L\,(\tilde{\phi}^{(e)}) - f^{(e)} \right\rfloor dD^{(e)} = 0\,;\; i = 1, 2, 3, \ldots., m \tag{3.1.7}$$

a set of such expression are developed for each element and combined for the entire domain. This assembly of elements yields the global matrix and results in large algebraic equations which must be solved simultaneously.

In many cases, it is possible to reduce the order of derivatives of the differential terms by applying the integration by part to the integral expressions of the finite element equations. The surface or line integral resulting from the integration by part provides convenient means for applying certain boundary conditions for the problem. These boundary conditions are called natural boundary conditions and are sometimes moved to right hand side of the governing equation. Although these line integral terms appear in every element of the system, they are only to be evaluated along the boundary elements since all of the internal contributions will be canceled each other.

3.2. Discretization of Domain

Using basic element, the domain can be discretized into the element assembly. Consequently, refined discretization leads to the more exact solution of the partial differential equations. In most cases, the shape of these basic elements is geometrically simple. In Figure 3.1, typical two-dimensional elements are shown. In the figure, the three node triangular element is the simplest and the most common element that can define those unknown variables in the two dimensional domain, because it is simple and capable of modeling any shape. The four node rectangular element is another common element. It can be formed directly or through the combination of two or four triangular elements. Elements with additional nodes are used in describing higher order approximating functions. By mapping a parent element in the local coordinate system into the distorted global coordinate system, these elements allow constructing elements with curved sides.

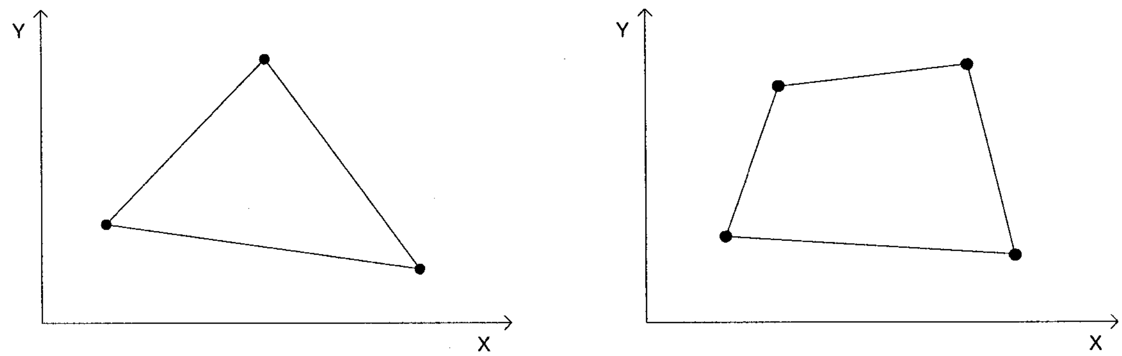

Figure 3.1 Examples of typical two-dimensional element.

The finite element equation is then integrated in the local coordinate system and by using the Jacobian matrix, this integration is interpreted into the global coordinate system to evaluate the parent element. In simulating both steady and unsteady flow model in domains with irregular geometry, since the method of discretization is related to the capability of how well the model approximates the continuous flow equations, the most careful attention is required in computational domain discretization.

3.3. Convection Dominated Flow Problem

The main problem of the numerical solution lies in the competition between the elliptic and hyperbolic character of the differential equation. In modeling of the flow problems, if the convection term is dominant, the problem will behave mostly as hyperbolic equation. For example, considering the following 1-D steady convection and diffusion equation as

$$U\frac{d\phi}{dx}-\frac{d}{dx}\left(k\frac{d\phi}{dx}\right)=0 \tag{3.3.1}$$

Using the Galerkin formulation, Equation (3.3.1) can be given in a discretization form as

$$\phi \approx \sum N_i\tilde{\phi}_i = N\tilde{\phi} \tag{3.3.2}$$

where N_k are shape functions and $\tilde{\phi}$ represent a set of unknown variables

In matrix form,

$$K_{ij}\tilde{\phi}_j = 0 \tag{3.3.3}$$

where,

$$K_{ij} = \int_0^L W_i U\frac{dN_j}{dx}dx + \int_0^L \frac{dW_i}{dx}k\frac{dN_j}{dx}dx \tag{3.3.4}$$

Assume that it is defined over the range of $0<x<L$.

Using linear shape functions, standard Galerkin weighing function ($W_i = N_i$), and equal size element length of h, and constant values of U, k and Q yields the resulting stiffness matrix given by

$$k_e = \begin{bmatrix} \frac{k}{h}-\frac{U}{2} & -\frac{k}{h}+\frac{U}{2} \\ -\frac{k}{h}-\frac{U}{2} & \frac{k}{h}+\frac{U}{2} \end{bmatrix} \tag{3.3.5}$$

the assembled stiffness matrix can then be given as

$$K=\begin{bmatrix} \frac{k}{h}-\frac{U}{2} & -\frac{k}{h}+\frac{U}{2} & 0 & 0 & & & \\ -\frac{k}{h}-\frac{U}{2} & \frac{2k}{h} & -\frac{k}{h}+\frac{U}{2} & 0 & & & \\ & -\frac{k}{h}-\frac{U}{2} & \frac{2k}{h} & -\frac{k}{h}+\frac{U}{2} & & & \\ & & & & & & \\ & & & & -\frac{k}{h}-\frac{U}{2} & \frac{2k}{h} & -\frac{k}{h}+\frac{U}{2} \\ & & & & 0 & -\frac{k}{h}-\frac{U}{2} & \frac{k}{h}+\frac{U}{2} \end{bmatrix} \tag{3.3.6}$$

Due to the convective terms, the matrix in Equation (3.3.6) is nonsymmetric. Also, it is not diagonally dominant as convective terms dominate and $U/2$ is larger than k/h. From Equation (3.3.6), the differential form of equation can be written as follows.

$$\left(-\frac{k}{h}-\frac{U}{2}\right)\phi_{i-1}+\frac{2k}{h}\phi_i+\left(-\frac{k}{h}+\frac{U}{2}\right)\phi_{i+1}=0 \tag{3.3.7}$$

The element Peclet number Pe is defined as

$$Pe=\frac{Uh}{k} \tag{3.3.8}$$

Then Equation (3.3.7) can be rewritten as

$$\left(-\frac{Pe}{2}-1\right)\tilde{\phi}_{i-1}+2\tilde{\phi}_i+\left(\frac{Pe}{2}-1\right)\tilde{\phi}_{i+1}=0 \tag{3.3.9}$$

Equation (3.3.9) is identical to the usual central finite difference approximation which can be obtained by using

$$\frac{d\phi}{dx}\approx\frac{\tilde{\phi}_{i+1}-\tilde{\phi}_{i-1}}{2h} \tag{3.3.10}$$

and

$$\frac{d^2\phi}{dx^2} \approx \frac{\tilde{\phi}_{i+1} - 2\tilde{\phi}_i + \tilde{\phi}_{i-1}}{h^2} \tag{3.3.11}$$

The accuracy of the nodal point deteriorates as the Peclet number increases and especially for $Pe \to \infty$, the solution is purely oscillatory. To overcome the bad approximation, motivated by the fact that the propagation of information is in the direction of velocity U, adapting one-sided finite difference approximation for the first derivatives from finite difference formulation as

$$\frac{d\phi}{dx} = \frac{\tilde{\phi}_i - \tilde{\phi}_{i-1}}{h} \tag{3.3.12}$$

Substituting above Equation (3.3.12) into central difference Equation (3.3.9) yields

$$(-Pe-1)\tilde{\phi}_{i-1} + (2+Pe)\tilde{\phi}_i - \tilde{\phi}_{i+1} = 0 \tag{3.3.13}$$

3.3.1. Petrov-Galerkin method

One of the applications of the upwind approximation to the finite element method is Petrov-Galerkin method. The notable difference between standard Galerkin method and Petrov-Galerkin method lies in the type of the weighting functions that is $W_i \neq N_i$. The weighting function is given as

$$W_i = N_i + \alpha W_i^* \tag{3.3.14}$$

where W_i^* is such that

$$\int_{\Omega_r} W_i^* dx = \pm \frac{h}{2} \tag{3.3.15}$$

The sign depends on whether U is a velocity directed towards or away from the node.

The most convenient form of W_i^* is the following simple definition which is a discontinuous function

$$\alpha W_i^* = \alpha \frac{h}{2} \frac{dN_i}{dx} \text{ (sign } U) \tag{3.3.16}$$

With the above weighting functions, the approximation is equivalent to Equation (3.3.9) given by

$$\left[\frac{-Pe(\alpha+1)}{2} - 1\right]\tilde{\phi}_{i-1} + \left[2 + \alpha(Pe)\right]\tilde{\phi}_i + \left[\frac{-Pe(\alpha-1)}{2} - 1\right]\tilde{\phi}_{i+1} = 0 \tag{3.3.17}$$

As it can be seen from Equation (3.3.17), with $\alpha = 0$, the standard Galerkin method can be obtained. For $\alpha = 1$, the full upwind discrete equation becomes available. The value of α for the one-dimensional case is chosen as

$$|\alpha| = \alpha_{\text{Opt}} = \coth \frac{|Pe|}{2} - \frac{2}{Pe} \tag{3.3.18}$$

If the value of α is given as bigger than α_{Crit}, oscillatory solution will not be present. The value of α_{Crit} can be given by

$$\alpha_{\text{Crit}} = 1 - \frac{2}{|Pe|} \tag{3.3.19}$$

If using the standard Galerkin method, oscillation will occur when

$$|Pe| > 2 \tag{3.3.20}$$

3.3.2. Comparison of the standard Galerkin and Petrov-Galerkin method

In this section, a simple example of a typical convection and diffusion equation is solved using 3 different methods (standard Galerkin, fully upwind Petov-Galerkin, and optimized Petov-Galerkin). The solution obtained from each method will be compared with its analytical solution for various Peclet numbers. The equation is given as (After Zienkiewicz and Taylor, 2000)

$$U\frac{d\phi}{dx} - k\frac{d^2\phi}{dx^2} = 0 \tag{3.3.21}$$

and the boundary condition is $\phi = 0, \quad x = 0; \quad \phi = 1, \quad x = L$. The analytical solution of Equation (3.3.21) is given as follows

$$\phi = \frac{1 - e^{Ux/k}}{1 - e^{UL/k}} \tag{3.3.22}$$

Figure 3.2 shows the solution for Equation (3.3.21) with a corresponding Peclet number given as 2.0. For this relatively low Peclet number of less than 2.0, the Galekin formulation works just fine. The Galerkin FEM solution line follows analytical solution pretty well without any fluctuations. Figure 3.2(b) presents the solution in which Peclet number is 5.0.

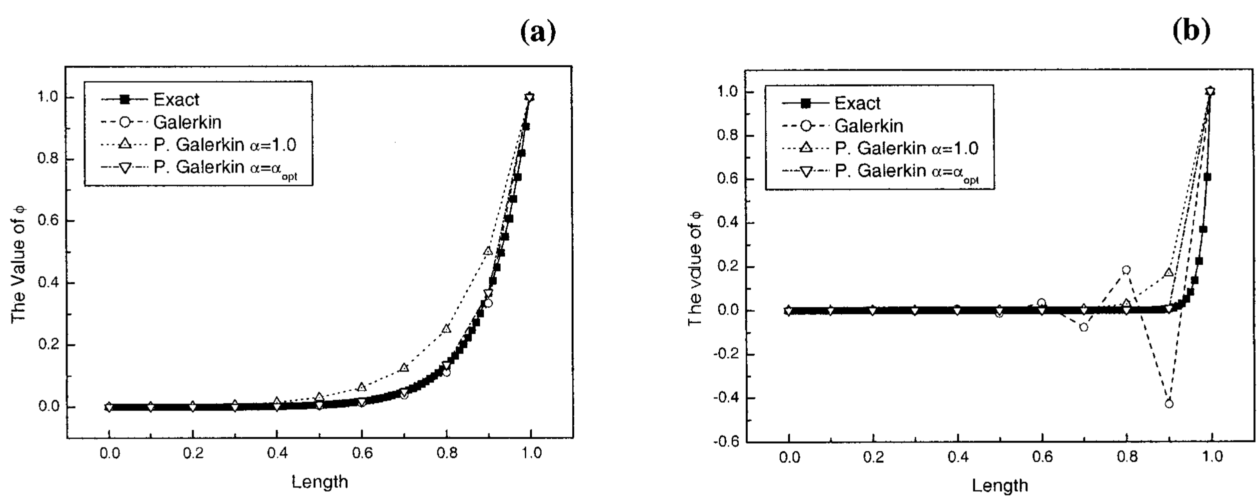

Figure 3.2 Applications for various Peclet numbers.

While the solution using the standard Galerkin formulation presents severe oscillations, the results using Petrov-Galerkin are more realistic. The oscillations become more severe when the Peclet number increases. Using the Petrov-Galerkin formulation, the result will be stable for the entire region.

Next, compare the results using Petrov-Galerkin formulation with its optimal value of α and with full upwind method $(\alpha = 1.0)$. It shows discrepancies between the analytical solutions for the latter case. Whereas the discrepancies are pronounced between the analytical solution and the solution using the full upwind method, the solution using optimal value of α shows good agreement with analytical solution regardless to the range of the Peclet number. For this upwind approximation with optimal value of α, more realistic results can be obtained through the entire range of Peclet numbers.

3.3.3. Application Petrov-Galerkin for multi-dimensional cases

Using Equation (3.3.19), the application of Petrov-Galerkin method is finding optimal value of α. For the two-dimensional case, the Peclet parameter is defined as

$$Pe = \frac{\mathbf{U}h}{k} \qquad \mathbf{U} = \begin{Bmatrix} U_1 \\ U_2 \end{Bmatrix} \tag{3.3.23}$$

Since these are a vector quantity, the upwinding interpretation will be directional properties. According to Hughes and Brooks (1982), the convection and the balancing diffusion are only in the direction of resultant velocity. Take account of this, it can be accomplished by taking the individual weighting functions as follows

$$\begin{aligned} W_k &= N_k + \alpha W_k^* = N_k + \frac{\alpha h}{2} \frac{U_1(\partial N_k/\partial x_1) + U_2(\partial N_k/\partial x_2)}{|\mathbf{U}|} \\ &\equiv N_k + \frac{\alpha h}{2} \frac{U_i}{|\mathbf{U}|} \frac{\partial N_k}{\partial x_i} \end{aligned} \tag{3.3.24}$$

where, α can be found for each element similar to the case of 1 dimensional problem as

$$\alpha = \alpha_{Opt} = \coth\frac{Pe}{2} - \frac{2}{Pe} \tag{3.3.25}$$

with

$$Pe = \frac{|\mathbf{U}|h}{k}$$

and $|\mathbf{U}| = \left(U_1^{\,2} + U_2^{\,2}\right)^{1/2}$ or $\sqrt{U_i U_i}$

These expressions are under the assumption that the velocity components are constant in a particular element and that the element length can be reasonably defined. Following Equation (3.3.24), the Petrov-Galerkin weighting function shows the following form of

$$W_i = N_i + \frac{\alpha\bar{h}}{2|U|}\left(u\frac{\partial N_i}{\partial x} + v\frac{\partial N_i}{\partial y}\right) \tag{3.3.26}$$

This weighting function provides an extension of one-dimensional weighting functions and there is no component of any cross-flow diffusion, which means diffusion in the direction orthogonal to the flow is not taken into account. That is, balancing diffusion is only in the direction of the flow. For this reason, it is called Streamline-Upwind-Petrov-Galerkin (SUPG) method. Also, for the application of the incompressible fluid flow equation, the α in Equation (3.3.25) can be found using cell Reynolds number instead of Peclet number

$$\alpha = \coth\frac{\gamma}{2} - \frac{2}{\gamma} \text{ and } \gamma = \mathrm{Re}|\mathbf{U}|\bar{h} \tag{3.3.27}$$

For the two- and three-dimensional computations, for practical reason, the Petrov-Galerkin weighting functions are applied for the convective and source terms only, while the shape function is used as weighting function for the diffusion terms (Heinrich, 1999).

This Petrov-Galerkin algorithm can be considered as a particular case of a more generalized Galerkin-Least-Suare (GLS) method (Hughes et. al., 1989).

3.4. The Penalty Function

The independent variable, P, which appears in the governing equations, can be solved using the penalty function approach. The penalty approach is incorporated to enforce the constraints of the incompressibility (Zienkiewicz, 1989). This approach also can be written in matrix form so that the non-hydrostatic pressure P is defined as

$$P^{(n+1)} = P^{(n)} - \lambda\left(\frac{\partial U}{\partial x} + \frac{\partial V}{\partial y}\right) \tag{3.4.1}$$

One of the main advantages of the penalty function is to reduce the number of variables and satisfy the continuity equation automatically when the solution is converged. Regarding to the model formulation, the mixed interpolation scheme is introduced to eliminate pressure oscillation in computing those values of P. The term, mixed interpolation refers to a scheme in which a lower order of interpolation method is incorporated for pressure than for the velocity components (P is evaluated for elements instead of individual nodes for which velocity is evaluated).

Many researchers solve shallow water equations as well as Navier-Stokes equations by finite element method using the same order of interpolation for both the velocity components and pressure (water surface elevation in shallow water equation) term. Using the equal-order interpolation, they report that there are significant problems to obtain free of oscillation on the water surface elevation solutions. Past researchers found that the use of equal order interpolation causes spurious oscillations in the pressure. Various approaches have been proposed to resolve this problem. One of the widely used methods for eliminating the oscillation in pressure terms is the use of mixed interpolation scheme in which lower order of interpolation for the pressure than the velocity components.

3.5. Two-dimensional Navier-Stokes Equations

The governing equation with the substitution of the stress terms with function of velocities, using Cartesian coordinate, two dimensional, steady state, can be rewritten as follows.

The continuity equation

$$\frac{\partial U}{\partial x}+\frac{\partial V}{\partial y}=0 \tag{3.5.1}$$

The x-direction momentum equation

$$U\frac{\partial U}{\partial x}+V\frac{\partial U}{\partial y}=-\frac{\partial}{\partial y}\left(\frac{P}{\rho}\right)+\frac{\partial}{\partial y}\left(2\nu_T\frac{\partial U}{\partial y}\right)+\frac{\partial}{\partial y}\left[\nu_T\left(\frac{\partial U}{\partial y}+\frac{\partial V}{\partial x}\right)\right]+F_x+\left[\frac{\partial}{\partial z}\left(\frac{\tau_s}{\rho}\right)\right]_{z=H} \tag{3.5.2}$$

The y-direction momentum equation

$$U\frac{\partial V}{\partial x}+V\frac{\partial V}{\partial y}=-\frac{\partial}{\partial y}\left(\frac{P}{\rho}\right)+\frac{\partial}{\partial x}\left[\nu_T\left(\frac{\partial U}{\partial y}+\frac{\partial V}{\partial x}\right)\right]+\frac{\partial}{\partial y}\left(2\nu_T\frac{\partial V}{\partial y}\right)+F_y+\left[\frac{\partial}{\partial z}\left(\frac{\tau_n}{\rho}\right)\right]_{z=H} \tag{3.5.3}$$

where, U and V are the longitudinal and lateral surface velocity, respectively; P is the mean pressure, ν_T is the turbulent viscosity; $F_x = g\ sin\theta$ and $F_y = 0.0$ are body forces in the x and y directions respectively; g is the gravitational acceleration; θ is the average water surface slope in the longitudinal direction; z is vertical distance from channel bed; H is the average flow depth; τ_s, τ_n are the longitudinal and lateral turbulent shear stresses respectively; and ρ is the fluid density.

The two last terms of shear stress appear in equations (3.5.2) and (3.5.3) are evaluated at the water surface in the x, and y directions, respectively. These stress terms are related to the effects of the vertical variation of the turbulent shear stress at the surface. These stress terms can be expressed in terms of the surface velocity U and V, and the friction factor f according to,

$$\frac{\tau_s(z)}{\rho} = \nu_T \frac{\partial U}{\partial z} \qquad (3.5.4)$$

and

$$\frac{\tau_n(z)}{\rho} = \nu_T \frac{\partial V}{\partial z} \qquad (3.5.5)$$

where, ν_t = kinematic eddy viscosity; and k = turbulent kinetic energy.

Assuming a power law variation of the longitudinal velocity in the vertical direction, a general relationship can be defined as

$$\frac{U(z)}{U_{av}} = \frac{1+m}{m}\left(\frac{z}{H}\right)^{1/m} \qquad (3.5.6)$$

where,

$$m = \kappa\sqrt{\frac{8}{f}} \qquad (3.5.7)$$

in which, $U(z)$ = the longitudinal local velocity as a function of vertical distance from bed; U_{av} = the depth averaged longitudinal velocity; and f = the Darcy-Weisbach friction factor.

An expression for the vertical variation of the turbulent viscosity can be written as

$$\nu_T = \kappa V_* z\left(1-\frac{z}{H}\right) \qquad (3.5.8)$$

where, κ = von Kármán's constant; V_* = shear velocity ($\sqrt{gRS_E}$); R = the hydraulic radius; S_E = energy gradient slope. Substituting Equation (3.5.4) through (3.5.6) into the term which defines the vertical variation of the longitudinal shear stress terms in Equation (3.5.2) yields

$$\left(\frac{\partial}{\partial z}\left(\frac{\tau_s}{\rho}\right)\right)_{z=H} = -\frac{\kappa}{H}\frac{1+m}{m^2}|U|U\sqrt{\frac{f}{8}} \tag{3.5.9}$$

Similarly, the term for the vertical variation of the lateral turbulent shear stress in Equation (3.5.3) becomes

$$\left(\frac{\partial}{\partial z}\left(\frac{\tau_n}{\rho}\right)\right)_{z=H} = -\frac{\kappa}{H}\frac{1+m}{m^2}|V|V\sqrt{\frac{f}{8}} \tag{3.5.10}$$

3.5.1. Discretization form of the x-momentum equation

Next, the weak form of the previous governing equation is used to place in a form suitable for obtaining approximate solution. In order to obtain the weak form, the X-direction momentum equation is multiplied by the weighting function δU and integrating over the computational domain to yield

$$\begin{aligned} f_U &= \int_A \delta U\left(U\frac{\partial U}{\partial x}+V\frac{\partial U}{\partial y}-G_x-F_x\right)dA+\int_A \delta U\frac{\partial P}{\partial x}dA \\ &-\int_A \delta U\left[\frac{\partial}{\partial x}\left(2\nu_T\frac{\partial U}{\partial x}\right)+\frac{\partial}{\partial y}\left\{\nu_T\left(\frac{\partial U}{\partial y}+\frac{\partial V}{\partial x}\right)\right\}\right]dA \end{aligned} \tag{3.5.11}$$

where, $G_x = -\frac{\kappa}{H}\frac{1+m}{m^2}U|U|\sqrt{\frac{f}{8}}$, and $F_x = g\sin\theta$

Applying integration by part formula to the pressure term and to the second derivative forms of the last two terms yields

$$f_U = \int_A \delta U\left(U\frac{\partial U}{\partial x} + V\frac{\partial U}{\partial y} - G_x - F_x\right)dA + \int_A \frac{\partial(\delta UP)}{\partial x}dA - \int_A \frac{\partial \delta U}{\partial x}PdA$$
$$-\int_A \frac{\partial}{\partial x}\left\{\delta U\left(2\nu_T\frac{\partial U}{\partial x}\right)\right\}dA - \int_A \frac{\partial}{\partial y}\left\{\delta U\nu_T\left(\frac{\partial U}{\partial y} + \frac{\partial V}{\partial x}\right)\right\}dA \tag{3.5.12}$$
$$+\int_A\left(\frac{\partial \delta U}{\partial x}2\nu_T\frac{\partial U}{\partial x}\right)dA + \int_A \frac{\partial \delta U}{\partial y}\nu_T\left(\frac{\partial U}{\partial y} + \frac{\partial V}{\partial x}\right)dA$$

Using the divergence theorem, this equation can be rewritten as follows

$$f_U = \int_A \delta U\left(U\frac{\partial U}{\partial x} + V\frac{\partial U}{\partial y} - G_x - F_x\right)dA + \int_\Gamma (\delta UP)n_x d\Gamma - \int_A \frac{\partial \delta U}{\partial x}PdA$$
$$-\int_\Gamma \delta U\left\{\left(2\nu_T\frac{\partial U}{\partial x}\right)n_x + \nu_T\left(\frac{\partial U}{\partial y} + \frac{\partial V}{\partial x}\right)n_y\right\}d\Gamma \tag{3.5.13}$$
$$+\int_A\left(\frac{\partial \delta U}{\partial x}2\nu_T\frac{\partial U}{\partial x}\right)dA + \int_A \frac{\partial \delta U}{\partial y}\nu_T\left(\frac{\partial U}{\partial y} + \frac{\partial V}{\partial x}\right)dA$$

where, Γ= the coordinate along the boundary of the domain, and n_x, n_y =directional cosines of the *i* and *j* unit vectors, respectively.

The line integration is performed along the boundaries of the channel. For the boundary of which the directional cosine n_x, U should be zero. In addition, along the boundary without lateral discharge, which has the directional cosine n_y, both derivatives of U and V equal to zero, i.e.

$$\int_\Gamma (\delta UP)n_x d\Gamma = 0 \tag{3.5.14}$$

$$\int_\Gamma \delta U\left(2\nu_T\frac{\partial U}{\partial x}\right)n_x d\Gamma = 0 \tag{3.5.15}$$

$$\int_\Gamma \delta U\nu_T\left(\frac{\partial U}{\partial y} + \frac{\partial V}{\partial x}\right)n_y d\Gamma = \int_\Gamma \delta U\nu_T\left(\frac{\partial U}{\partial y}\right)n_y d\Gamma \tag{3.5.16}$$

Since along the wall, $V = 0$ and $\nu_T\dfrac{\partial U}{\partial y}$ term can be replaced by $\dfrac{\tau_w}{\rho}$ and

$$\frac{\tau_w}{\rho} = -V_*|V_*| = -C_w|U|U \tag{3.5.17}$$

where, $C_w = \dfrac{\kappa^2}{\left(\ln E\dfrac{yV_*^2}{\nu}\right)}$ or simply $\dfrac{f_w}{8}$

All of the line integral terms vanish after substituting above Equations (3.5.14), (3.5.15), and (3.5.16) into Equation (3.5.13). After substitution of penalty function (Equation (3.4.4)) for the pressure term in Equation (3.5.14), we obtain

$$\begin{aligned} f_U &= \int_A \delta U\left(U\frac{\partial U}{\partial x} + V\frac{\partial U}{\partial y} - G_x - F_x\right)dA - \int_A \frac{\partial \delta U}{\partial x}\left\{P - \lambda\left(\frac{\partial U}{\partial x} + \frac{\partial V}{\partial y}\right)\right\}dA \\ &+ \int_A\left(\frac{\partial \delta U}{\partial x}2\nu_T\frac{\partial U}{\partial x}\right)dA + \int_A \frac{\partial \delta U}{\partial y}\nu_T\left(\frac{\partial U}{\partial y} + \frac{\partial V}{\partial x}\right)dA + \int_\Gamma \delta U C_w|U|Un_y d\Gamma \end{aligned} \tag{3.5.18}$$

The resulting finite element equation can be written as

$$\begin{aligned} f_U &= \int_A N_i\left(U\frac{\partial N_j}{\partial x}U_j + V\frac{\partial N_j}{\partial y}U_j - G_x - F_x\right)dA \\ &- \int_A \frac{\partial N_i}{\partial x}\left\{P - \lambda\left(\frac{\partial N_j}{\partial x}U_j + \frac{\partial N_j}{\partial y}V_j\right)\right\}dA + \int_A\left(\frac{\partial N_i}{\partial x}2\nu_T\frac{\partial N_j}{\partial x}U_j\right)dA \\ &+ \int_A \frac{\partial N_i}{\partial y}\nu_T\left(\frac{\partial N_j}{\partial y}U_j + \frac{\partial N_j}{\partial x}V_j\right)dA + \int_\Gamma N_i C_w|U|N_j U_j n_y d\Gamma \end{aligned} \tag{3.5.19}$$

The derivative forms of the x-momentum equation with respect to U and V for the entries of the Jacobian (or tangential) matrix are written as follows.

$$\begin{aligned} \frac{\partial f_U}{\partial U_j} &= \int_A N_i\left(N_j\frac{\partial U}{\partial x} + U\frac{\partial N_j}{\partial x} + V\frac{\partial N_j}{\partial y} - \frac{\partial G_x}{\partial U_j} - \frac{\partial F_x}{\partial U_j}\right)dA + \int_A \frac{\partial N_i}{\partial x}\lambda\frac{\partial N_j}{\partial x}dA \\ &+ \int_A \frac{\partial N_i}{\partial x}2\nu_T\frac{\partial N_j}{\partial x}dA + \int_A \frac{\partial N_i}{\partial y}\nu_T\frac{\partial N_j}{\partial y}dA + \int_\Gamma N_i C_w|U|N_j n_y d\Gamma \end{aligned} \tag{3.5.20}$$

$$\frac{\partial f_U}{\partial V_j} = \int_A N_i N_j\frac{\partial U}{\partial y}dA + \int_A \frac{\partial N_i}{\partial x}\lambda\frac{\partial N_j}{\partial y}dA + \int_A \frac{\partial N_i}{\partial y}\nu_T\frac{\partial N_j}{\partial y}dA \tag{3.5.21}$$

Derivative forms of G_x and F_x terms with respect to U can be written as following equation in detail. The derivative forms of these functions with respect to V are equal to 0.

$$\frac{\partial G_x}{\partial U_j} = \int_A \frac{\kappa}{H} \frac{1+m}{m^2} N_i N_j 2|U| \sqrt{\frac{f}{8}} \tag{3.5.22a}$$

$$\frac{\partial F_x}{\partial U_j} = 0 \tag{3.5.22b}$$

3.5.2. Discretization form of the y-momentum equation

Similar to the process followed to obtain the weak form of the x-momentum equation, the weak form of the y-momentum equation is obtained by choosing the weighting function as δV, and by multiplying the y-momentum equation and integrating over each element to yield

$$\begin{aligned} f_V &= \int_A \delta V \left(U \frac{\partial V}{\partial x} + V \frac{\partial V}{\partial y} - G_y - F_y \right) dA + \int_A \delta V \frac{\partial P}{\partial y} dA \\ &- \int_A \delta V \left[\frac{\partial}{\partial y} \left(2\nu_T \frac{\partial V}{\partial y} \right) + \frac{\partial}{\partial x} \left\{ \nu_T \left(\frac{\partial U}{\partial y} + \frac{\partial V}{\partial x} \right) \right\} \right] dA \end{aligned} \tag{3.5.23}$$

where, $G_Y = -\frac{\kappa}{H} \frac{1+m}{m^2} V|V| \sqrt{\frac{f}{8}}$, and $F_y = 0$ (3.5.24)

Similar to the x-momentum equation, applying integration by parts to the pressure term and the second derivative of the last two terms yields the following equation.

$$f_V = \int_A \delta V \left(U \frac{\partial V}{\partial x} + V \frac{\partial V}{\partial y} - G_y - F_y \right) dA + \int_A \frac{\partial(\delta VP)}{\partial y} dA - \int_A \frac{\partial \delta V}{\partial y} PdA$$
$$- \int_A \frac{\partial}{\partial y} \left\{ \delta V \left(2\nu_T \frac{\partial V}{\partial y} \right) \right\} dA - \int_A \frac{\partial}{\partial x} \left\{ \delta V \nu_T \left(\frac{\partial U}{\partial y} + \frac{\partial V}{\partial x} \right) \right\} dA \qquad (3.5.25)$$
$$+ \int_A \left(\frac{\partial \delta V}{\partial y} 2\nu_T \frac{\partial V}{\partial y} \right) dA + \int_A \frac{\partial \delta V}{\partial x} \nu_T \left(\frac{\partial U}{\partial y} + \frac{\partial V}{\partial x} \right) dA$$

Using the divergence theorem, Equation (3.4.25) can be given as

$$f_V = \int_A \delta V \left(U \frac{\partial V}{\partial x} + V \frac{\partial V}{\partial y} - G_y - F_y \right) dA + \int_\Gamma (\delta VP) n_y d\Gamma - \int_A \frac{\partial \delta V}{\partial y} PdA$$
$$- \int_\Gamma \delta V \left\{ \left(2\nu_T \frac{\partial V}{\partial y} \right) n_y + \nu_T \left(\frac{\partial U}{\partial y} + \frac{\partial V}{\partial x} \right) n_x \right\} d\Gamma \qquad (3.5.26)$$
$$+ \int_A \left(\frac{\partial \delta V}{\partial y} 2\nu_T \frac{\partial V}{\partial y} \right) dA + \int_A \frac{\partial \delta V}{\partial x} \nu_T \left(\frac{\partial U}{\partial y} + \frac{\partial V}{\partial x} \right) dA$$

where, Γ= the coordinate along the boundary of the domain, and n_x, n_y =directional cosines of the *i* and *j* unit vectors, respectively.

Along the channel boundary of which directional cosine is n_y, V should be zero. In addition, along the boundary without lateral discharge, which has the directional cosine n_x, both derivatives of U and V is equal to zero. These are shown as following equations

$$\int_\Gamma (\delta VP) n_y d\Gamma = 0 \qquad (3.5.27)$$

$$\int_\Gamma \delta V \left(2\nu_T \frac{\partial V}{\partial y} \right) n_y = 0 \qquad (3.5.28)$$

$$\int_\Gamma \delta V \nu_T \left(\frac{\partial U}{\partial y} + \frac{\partial V}{\partial x} \right) n_x d\Gamma = \int_\Gamma \delta V \nu_T \left(\frac{\partial V}{\partial x} \right) n_x d\Gamma \qquad (3.5.29)$$

Since along the wall, $U = 0$ and $\nu_T \dfrac{\partial V}{\partial x}$ term can be replaced by $\dfrac{\tau_w}{\rho}$, it is possible to write

$$\frac{\tau_w}{\rho} = -V_*|V_*| = -C_w|V|V \tag{3.5.30}$$

where, $C_w = \dfrac{\kappa^2}{\left(\ln E \dfrac{yV_*^2}{\nu}\right)}$ or simply $\dfrac{f_w}{8}$

All of the line integral terms in Equation (3.5.26) vanish after substituting above Equations (3.5.27), (3.5.28), and (3.5.29) into Equation (3.5.26). After substitution of the penalty function (Equation (3.3.4)) for the pressure term, Equation (3.5.26) can be rewritten as

$$\begin{aligned} f_U &= \int_A \delta V\left(U\frac{\partial V}{\partial x} + V\frac{\partial V}{\partial y} - G_y - F_y\right)dA - \int_A \frac{\partial \delta V}{\partial y}\left\{P - \lambda\left(\frac{\partial U}{\partial x} + \frac{\partial V}{\partial y}\right)\right\}dA \\ &+ \int_A\left(\frac{\partial \delta V}{\partial y}2\nu_T\frac{\partial V}{\partial y}\right)dA + \int_A \frac{\partial \delta V}{\partial x}\nu_T\left(\frac{\partial U}{\partial y} + \frac{\partial V}{\partial x}\right)dA + \int_\Gamma \delta V C_w|V|Vn_x d\Gamma \end{aligned} \tag{3.5.31}$$

Using the finite element formulation, Equation (3.5.31) can be written as follows

$$\begin{aligned} f_V &= \int_A N_i\left(U\frac{\partial N_j}{\partial x}V_j + V\frac{\partial N_j}{\partial y}V_j - G_y - F_y\right)dA \\ &- \int_A \frac{\partial N_i}{\partial y}\left\{P - \lambda\left(\frac{\partial N_j}{\partial x}U_j + \frac{\partial N_j}{\partial y}V_j\right)\right\}dA + \int_A\left(\frac{\partial N_i}{\partial y}2\nu_T\frac{\partial N_j}{\partial y}V_j\right)dA \\ &+ \int_A \frac{\partial N_i}{\partial x}\nu_T\left(\frac{\partial N_j}{\partial y}U_j + \frac{\partial N_j}{\partial x}V_j\right)dA + \int_\Gamma N_i C_w|V|N_j V_j n_x d\Gamma \end{aligned} \tag{3.5.32}$$

To find Jacobian matrix entries, the derivative form of the Equation (3.5.32) is obtained. The first order differential form of the y-momentum equation with respect to U yields

$$\frac{\partial f_V}{\partial U_j} = \int_A N_i N_j \frac{\partial V}{\partial x}dA + \int_A \frac{\partial N_i}{\partial y}\lambda\frac{\partial N_j}{\partial x}dA + \int_A \frac{\partial N_i}{\partial x}\nu_T\frac{\partial N_j}{\partial y}dA \tag{3.5.33}$$

Similarly, derivative form of the y-momentum equation with respect to V yields

$$\frac{\partial f_V}{\partial V_j} = \int_A N_i \left(U \frac{\partial N_j}{\partial x} + N_j \frac{\partial V}{\partial y} + V \frac{\partial N_j}{\partial y} - \frac{\partial G_y}{\partial V_j} - \frac{\partial F_y}{\partial V_j} \right) dA + \int_A \frac{\partial N_i}{\partial y} \lambda \frac{\partial N_j}{\partial y} dA$$
$$+ \int_A \frac{\partial N_i}{\partial y} 2 v_T \frac{\partial N_j}{\partial y} dA + \int_A \frac{\partial N_i}{\partial x} v_T \frac{\partial N_j}{\partial x} dA + \int_\Gamma N_i C_w |V| N_j n_x d\Gamma \tag{3.5.34}$$

Derivative forms of G_Y and F_Y terms with respect to U are 0 and derivative forms with respect to V can be written as

$$\frac{\partial G_y}{\partial V_j} = \int_A \frac{\kappa}{H} \frac{1+m}{m^2} N_i N_j 2|V| \sqrt{\frac{f}{8}} \tag{3.5.35}$$

3.6. General Computational Procedure

The algorithm is written using the Galerkin method and Cartesian *x-y* coordinates where *x*-direction is main flow (longitudinal) direction and *y*-direction is lateral direction. To formulate governing finite element equations, the weak form of the governing equation is obtained. In the weak form of these equations, the second derivatives are converted to the first derivative forms by applying the integration by parts where the weighting functions are interpreted as shape functions following the Gelerkin method.

These functions are numerically integrated for each element using the Gaussian quadrature. This process is carried out for all of the elements comprising the computational domain. These elements form a non-uniform continuous mesh through the computational domain. The integration of individual elements results in a local matrix which is then added to form a global matrix. In the Galerkin method, the weighting functions are interpreted as dependent variables as

$$\int_A \delta\phi \{F(\phi)\} dA = 0 \tag{3.6.1}$$

where, A = the computational domain area for differential equation, and $F(\phi)$ = the arbitrary governing partial differential equation which has variable ϕ.

Due to the nonlinear characteristics of the Navier-Stokes flow equations, an iterative solution scheme such as the Newton-Raphson method is employed in order to find a unique solution of the global matrix. The basic formation of Newton-Rhapson method can be written as

$$\int_A \delta\phi \left\{ \frac{\partial F(\phi)}{\partial \phi} \Delta\phi \right\} dA = -\int_A \delta\phi \{F(\phi)\} dA \tag{3.6.2}$$

Proceeding each iteration, corrections to the variable, $\Delta\phi$, which can be interpreted in this model as velocity component corrections to U and V (ΔU and ΔV, respectively), are obtained. The previous velocity estimates are updated using these corrections until the continuity equation is satisfied. In matrix form, this procedure can be expressed in consecutive iterative manner as follows

$$\begin{bmatrix} U \\ V \end{bmatrix}^{n+1} = \begin{bmatrix} U \\ V \end{bmatrix}^{n} + \theta \begin{bmatrix} \Delta U \\ \Delta V \end{bmatrix}^{n+1} \tag{3.6.3}$$

where, 6 is the relaxation coefficient and the superscripts (n) and $(n+1)$ refer to the previous and current iteration numbers respectively. The iteration process is continued until the maximum difference between the previous and current solution lies within the specified tolerance.

After generation of a mesh domain using 4-node quadrilateral elements, as a pre-process to solving the governing equation, a mesh-renumbering scheme is employed in order to reduce the bandwidth of the global matrix. This scheme reduces the global matrix bandwidth using the frontal wave concept, which connects nodes in the same element to the previously selected nodes to form the waves. This mesh renumbering scheme not only saves storage space but also reduces the computational time dramatically.

3.7. Model Verification and Application

The verification of the FEM Surface Flow Model has been conducted in two stages. In the first stage the model is verified utilizing abutments placed perpendicular to oncoming flows. The second stage verifies the model qualitatively in the presence of skewness.

Straight Abutments

In this section, model verification is presented for the straight abutment case using the laboratory experiments conducted by Molinas, Kheireldin, and Wu (1998). The experimental configuration is summarized into 3 categories according to the different protrusion ratio which is given 10%, 20%, and 30% and assigned to be A, B, and C run respectively. The abutment length ratio (abutment length /channel width) is fixed as 0.4.

For comparison of the shear amplification with the measured values, compute the shear stress in the channel contraction along the centerline of abutment and normalized by the approach shear. Figure 3.3 shows the computed shear amplification with respect to the abutment protrusion ratio and compared with measured data points. From the experimental study, in the channel contraction, shear amplification is found to be 1.1~1.4 in the A-runs, 1.6~2.0 for B-runs, and 2.7~3.0 in the C-runs. The computed values show good agreement with measured data and fall into the variation range within 10% error. Figure 3.4 compares computed and measured values in direct.

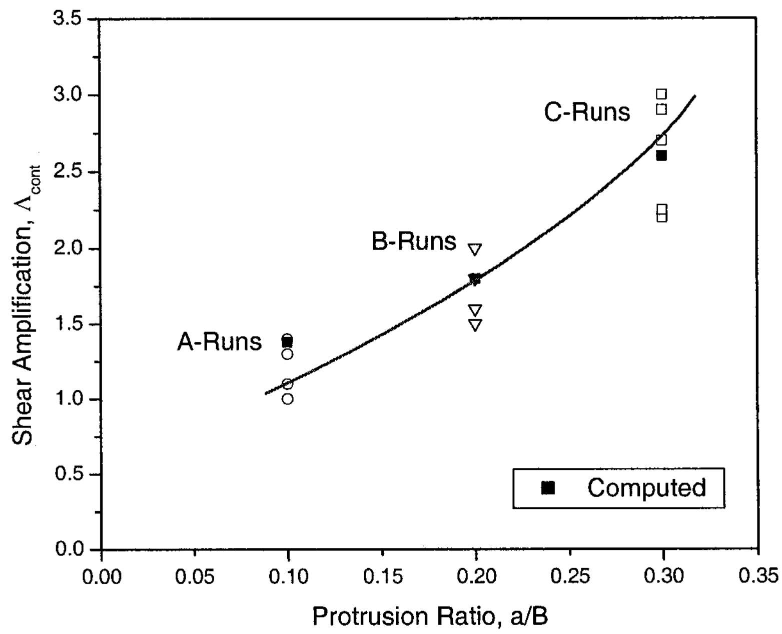

Figure 3.3 Variation of shear amplification with respect to protrusion ratio.

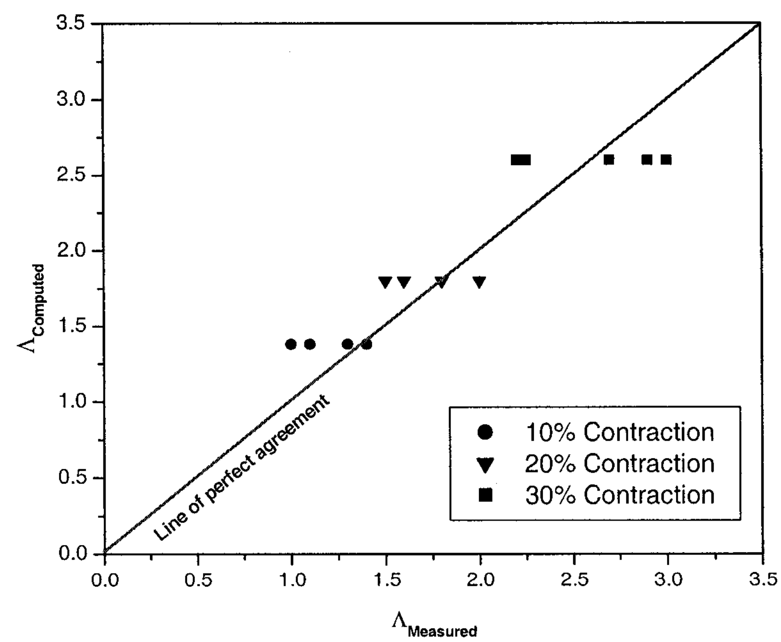

Figure 3.4 Comparison of computed values with measured shear amplifications.

According to Molinas, Kheireldin, and Wu (1998), the maximum shear stress obtained in the abutment nose is referred as local increase and at this location, the shear amplification is pronounced by the turning angle. The analysis of the shear stress in the contracted reach found that the turning angle effect was negligible and no longer extended through the channel contractions. Molinas and Hafez (2000) also did numerical analysis on the velocity amplification at the abutment nose using the straight abutment. This study extended their analysis to cover the velocity amplification in the channel contraction of the skewed abutment.

Skewed Abutments

Experimental data for flow distribution around skewed abutments are very limited. These data are generally collected in connection with abutment scour studies and relate the scour at the nose region to approach flow conditions. Kwan (1984) collected and presented one such experimental data set. Kwan's experimental study evaluates the abutment skewness effect on the maximum scour hole depth around abutment nose by using 4 different protrusion length cases with angle variations of $45^\circ, 90^\circ$ and 135°, respectively (Figure 3.5(a)).

Kwan's experimental results show that the maximum scour depth is found at abutment nose takes place for the 90° case, rather than the 45° case or the 135° case. As Kwan mentions, the controversial part of his result is for the 135° case. According to the experimental studies done by other previous researchers (Ahmad, 1953; Laursen, 1958; Tison, 1962), the maximum scour depth should increase proportionally with the skewness angle. That is, the maximum scour depth should have been obtained for the 135° case.

According to Kwan conclusion, this discrepancy is due to the duration of experiments (in excess of 72 hours in Kwan's experiment versus 3 to 4 hours in previous studies).

Since the major factor affecting the scour depth is the magnitude of flow velocity, the maximum scour is expected to take place at a location where the maximum velocity occurs. For model verification, Kwan's experiments with $L/B = 0.3$ and $U_a/V_* = 12$ have been simulated by changing the inclination of model abutments between 30° and 150° with 10° increments. Figure 3.3(b) presents the computed results. In this figure, maximum nose velocities are plotted against the skewness angle. The model used in this study predicts maximum velocity for the 90° case; whereas maximum velocities corresponding to the other two cases (45° and 135°) are less than the 90° case. This finding shows good agreement with Kwan (1984)'s experimental results. Figure 3.5(a) and 3.5(b) also shows that the smallest scour depths and velocities are found at $\theta = 45^\circ$ and $\theta = 30^\circ$, respectively. Following Kwan's conclusion, this finding is logical because at this inclination, the entrance to contracted reach is more streamlined to the flow. This geometrical inclination results in smaller normal flow velocity component to the abutment structure and weaker reverse flow.

Also from Figure 3.5, the perpendicular orientation $\theta = 90^\circ$ is shown to result in a larger scour depth and resultant velocity distribution than the $\theta = 135^\circ$ case, which agrees with Kwan's (1984) experimental study. However, the discrepancy to the maximum velocity remains within 15%, and the angle variation does not affect the maximum velocity significantly for a very thin abutment case.

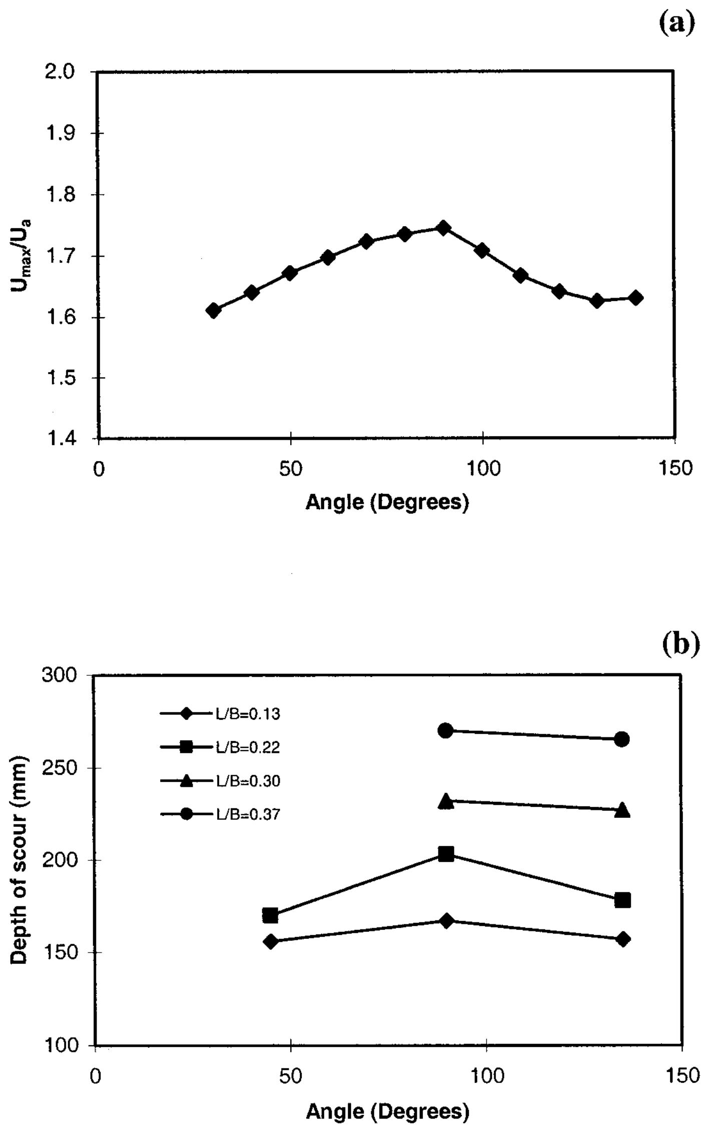

Figure 3.5 **Comparison between experimental and numerical results: (a) Kwan (1984) experiments; (b) numerical simulation for L/B=0.3 and U_a/V_*=12.**

3.8. Single Abutments

Symmetrically placed abutments with respect to the channel centerline can be simulated using single abutments with applying appropriate boundary conditions. For single abutments, a series of computer simulation runs to study the angle variation effects has been conducted. In these runs, the skewness angle has been changed by 10° increments while keeping a 30% projected contraction ratio (ratio of projected protrusion length perpendicular to flow to total channel width), σ , into the flow.

The range of skewness angle variation is kept between 30° and 150° to avoid secondary effects due to the abutment length. The entire computational mesh domain is constructed by using a nonuniform grid and composed of 4080 elements and 4239 nodal points using 4-node quadrilateral elements. To find and compare resultant flow velocity distributions, 3 plotting lines are selected along the contracted reach at the upstream, mid-point, and downstream end of the abutment placed perpendicular to approach flows (See Figure 3.6). After the model run, non-dimensional total velocities U_t / V_* are computed along these observation lines and used for the comparison.

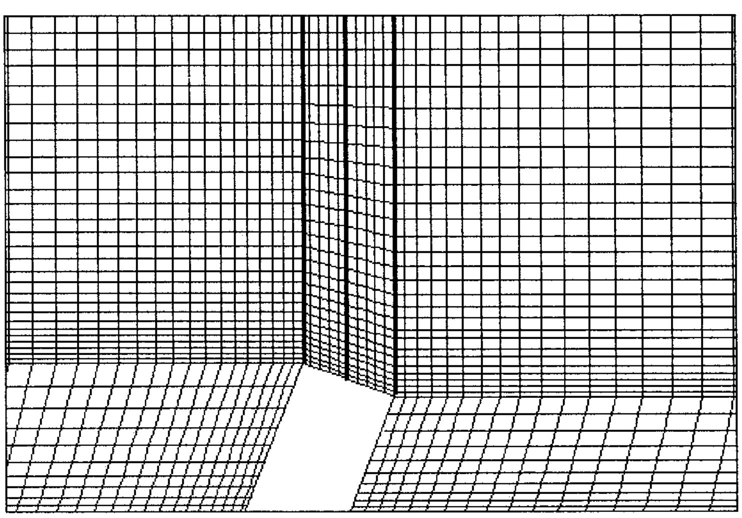

Figure 3.6 Plotting lines in the contracted reach for single abutments.

Each of the simulation runs was conducted using a projected contraction ratio of $\sigma = 30\%$ and fixed abutment length ratio, L/B, of 0.1, where $L =$ abutment length along the flow and $B =$ channel width. Simulation runs were repeated for 3 different Darcy-Weisbach friction factors, f, values of 0.08, 0.02 and 0.0088, respectively. The boundary conditions applied in these runs are

- At the upstream boundary where, $x = 0$: $U = u_0$, $V = 0$, where u_0 is given.
- Along the wall containing the abutment where, $y = 0$: wall boundary conditions.
- Along the wall representing the centerline, opposite to the wall containing the abutment where $Y = 1.0$: $V = 0$ and longitudinal boundary shear is zero.
- At the downstream boundary: uniform flow conditions with $\partial U/\partial x, \partial V/\partial y = 0$

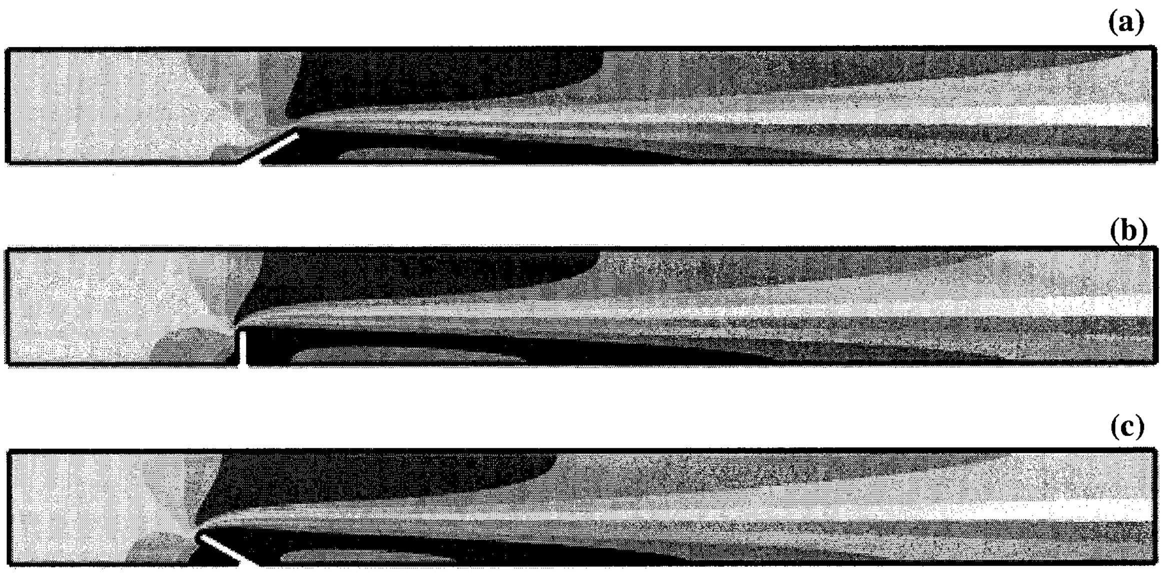

Figure 3.7 Total velocity distributions for single abutment for the case of f = 0.02: a) θ = 50°; b) θ = 90°; c) θ = 130°.

Computed Velocity distributions in the contracted reach using for 3 different skewness angles are shown in Figure 3.7. As shown in Figure 3.7(b), at 90° the reattachment length is longer than the two other cases which means that 90° case yields maximum nose velocity and results in maximum reattachment length. Comparing Figure 3.7(a) and Figure 3.7(c), where the skewness angle is less than 90° and greater than 90° show that the reattachment length is smaller than that of 90° case.

In Table 3.1, the maximum velocity in the contracted reach are listed and summarized for each run according to the angle variation in addition to 3 different friction factors. Maximum velocity proportionally increases with the skewness angle up to 90°. When skewness angle is between 90° and 130°, the maximum nose velocity decreases with skewness angle. Beyond the skewness angle of 130°, the maximum velocity increases again with angle increase. The reason is, at this large skewness angle, abutment length plays a major roll in diverting flows and causes the secondary effects to increase the magnitude of total velocity.

Figure 3.8 presents simulation result for the runs with 30% contraction ratio and a friction factor f of 0.02 . This figure represents the velocity profiles across the contracted reach due to the skewness angle of $50^\circ, 90^\circ$, and 130° cases, respectively. For the 50° case in Figure 3.8(a), the maximum velocity is obtained along the downstream plotting line. In Figure 3.8(b), for the 90° case, maximum velocity is obtained along the upstream plotting line and in Figure 3.8(c), for the 130° case, similar to the 50° case, the maximum velocity is obtained again at the downstream contracted reach. Comparing Figure 3.8(a) and 3.8(c), differences between each of maximum velocities along the contracted reach corresponding to the 130° case are more pronounced than that of the 50° case. However, do not show significant variation.

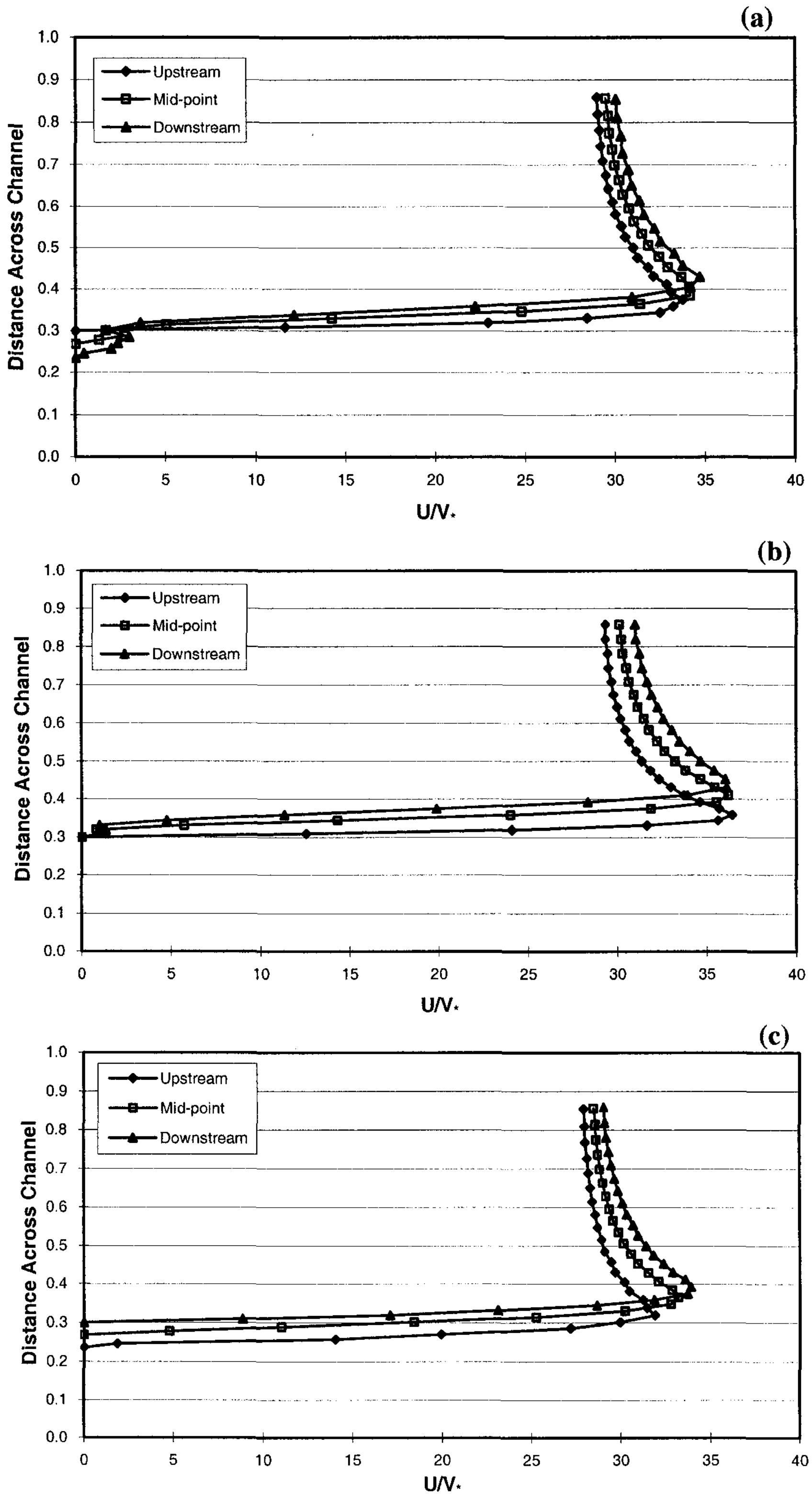

Figure 3.8 Resultant velocity distributions in the contracted reach due to single abutments for the case of $f = 0.02$: (a) $\theta = 50°$; (b) $\theta = 90°$; (c) $\theta = 130°$.

Table 3.1 Resultant maximum velocities for single abutments.

ϕ	Location	f = 0.08		f = 0.02		f = 0.0088	
		U_{max}/V_*	U_{max}/U_{app}	U_{max}/V_*	U_{max}/U_{app}	U_{max}/V_*	U_{max}/U_{app}
30°	Upstream	15.96	1.60	32.09	1.60	48.22	1.61
	Mid-Point	16.11	1.61	32.48	1.62	48.92	1.63
	Downstream	16.28	1.63	32.91	1.65	49.69	1.66
40°	Upstream	16.22	1.62	32.83	1.64	49.75	1.66
	Mid-Point	16.42	1.64	33.39	1.67	50.90	1.70
	Downstream	16.56	1.66	33.95	1.70	51.37	1.71
50°	Upstream	16.52	1.65	33.74	1.69	51.13	1.70
	Mid-Point	16.78	1.68	34.14	1.71	52.49	1.75
	Downstream	16.85	1.68	34.68	1.73	52.75	1.76
60°	Upstream	16.77	1.68	34.43	1.72	53.24	1.77
	Mid-Point	17.02	1.70	34.95	1.75	53.67	1.79
	Downstream	17.12	1.71	35.28	1.76	53.69	1.79
70°	Upstream	17.08	1.71	34.94	1.75	54.67	1.82
	Mid-Point	17.23	1.72	35.67	1.78	54.61	1.82
	Downstream	17.38	1.74	35.61	1.78	54.36	1.81
80°	Upstream	17.25	1.72	35.68	1.78	55.49	1.85
	Mid-Point	17.31	1.73	36.01	1.80	54.94	1.83
	Downstream	17.50	1.75	35.81	1.79	55.31	1.84
90°	Upstream	17.33	1.73	36.39	1.82	56.07	1.87
	Mid-Point	17.48	1.75	36.21	1.81	55.46	1.85
	Downstream	17.55	1.75	36.09	1.80	55.73	1.86
100°	Upstream	16.95	1.70	35.44	1.77	55.73	1.86
	Mid-Point	17.11	1.71	35.34	1.77	54.44	1.81
	Downstream	17.18	1.72	35.30	1.77	54.09	1.80
110°	Upstream	16.40	1.64	34.61	1.73	54.95	1.83
	Mid-Point	16.74	1.67	34.59	1.73	52.99	1.77
	Downstream	16.89	1.69	34.49	1.72	52.84	1.76
120°	Upstream	16.01	1.60	33.46	1.67	51.40	1.71
	Mid-Point	16.47	1.65	33.80	1.69	51.68	1.72
	Downstream	16.74	1.67	34.07	1.70	51.57	1.72
130°	Upstream	15.67	1.57	31.91	1.60	48.86	1.63
	Mid-Point	16.37	1.64	33.21	1.66	50.62	1.69
	Downstream	16.71	1.67	33.74	1.69	51.69	1.72
140°	Upstream	15.65	1.56	31.05	1.55	46.42	1.55
	Mid-Point	16.43	1.64	32.94	1.65	50.16	1.67
	Downstream	16.82	1.68	34.21	1.71	51.82	1.73
150°	Upstream	15.91	1.59	31.47	1.57	46.84	1.56
	Mid-Point	16.63	1.66	33.32	1.67	50.22	1.67
	Downstream	16.97	1.70	34.70	1.73	52.71	1.76

3.9. Double Abutments

The second series of simulation runs were conducted using pairs of abutments. For the velocity distribution in the skewed contracted reach, model runs are conducted for various abutment geometries reflecting the angle variations. In constructing abutment geometries, due to the unsymmetrical skewed abutment crossing, while one abutment makes an angle less than 90° with the approach flow, the other abutment makes a complementary angle greater than 90°. That is, the summation of both side always equal to 180°. For this reason, the results from the single abutment runs, where the wall not containing the abutment acts as a plane of symmetry, cannot be extended for the skewed double abutments. For this study, new mesh geometry is constructed using 3440 elements and 3574 nodal points. The abutment geometry and the velocity plotting lines along the abutment contracted reach are allowed to vary along with the angle of inclination while keeping the projected contraction ratio constant.

Resultant velocities are obtained along the 3 plotting lines shown in Figure 3.9 similar to the single abutment case except that the contracted reach is skewed. These plotting lines pass through the upstream, mid-point, and downstream of contracted reach to the flow direction. The abutment length ratio (L/B) is also fixed at 0.1 and the total projected contraction ratio was kept at 30% (the projected contraction by each two abutments has 15% projection ratio respectively).

The range of skewness angle variation was selected to vary between 50° and 130°, and is chosen from the practical aspects. The skewness angle range of variation for the abutment along the bottom wall was kept at 50° to 90° while skewness angle of the counter part abutment along the opposite wall was varied between 90° and 130°. With the exception of symmetrical boundary conditions along the top wall, all of the boundary conditions are kept same as the single abutment cases. To study channel roughness in the simulation runs, each skewness run is repeated with 3 different roughness friction factors ($f = 0.08, 0.02,$ and 0.0088). The numerical result for the velocity distributions of the entire channel is shown in Figure 3.10. Figure 3.10(a) represent for the case of skewness angle 70° and 110° case; Figure 3.10(b) represent for the case of 90° with the friction factor of $f = 0.02$.

The total velocity U_t $(= \sqrt{U^2 + V^2})$ distributions are computed and plotted along the observation lines to show the lateral velocity profiles across the upstream, mid-point and downstream end of the abutment. The maximum velocities computed in the contracted reach along the 3 plotting lines are given in Table 3.3. Total velocity distributions along each of the plotting lines at the upstream, mid-point and downstream end are shown in Figure 3.11 for $f = 0.02$. As shown in this figure, the difference of maximum velocities obtained from each plotting line in the contracted reach is pronounced for the case of skewness angles greater than 90°. For an example, the difference between maximum velocities corresponding to upstream, mid-point and downstream of the contracted reach for the 130° case (Figure 3.11(a)) is bigger than that of the 110° case (Figure 3.11(b)). As a result, similar to the single abutment cases, maximum velocity is obtained for the 90° case (Figure 3.11(c)) is the largest possible nose velocity.

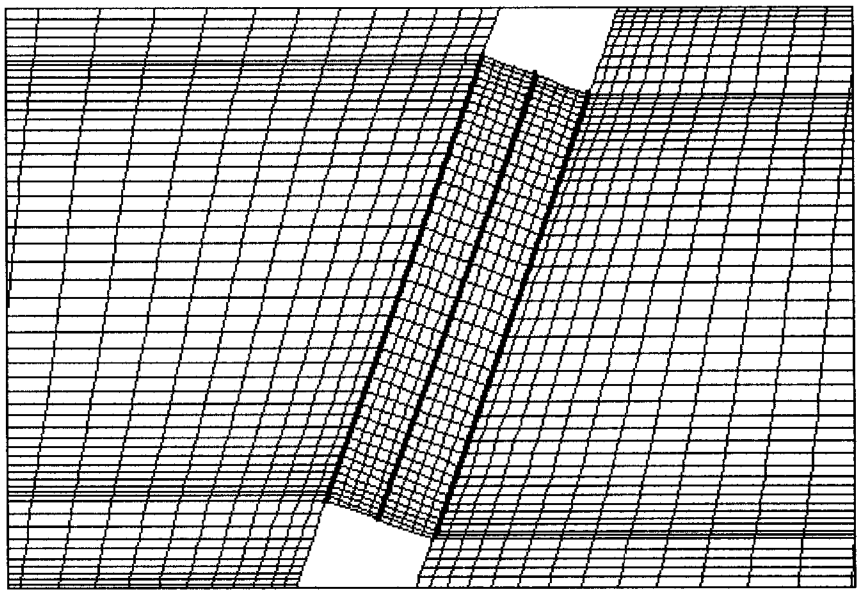

Figure 3.9 Plotting lines in the contracted reach for double abutments.

(a)

(b)

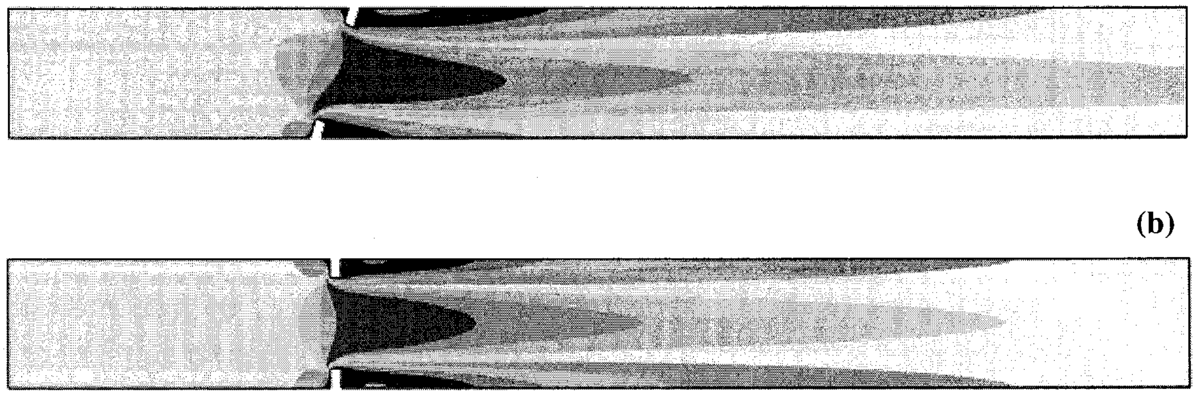

Figure 3.10 Velocity distributions for double abutments: (a) 70° and 110°; (b) 90°.

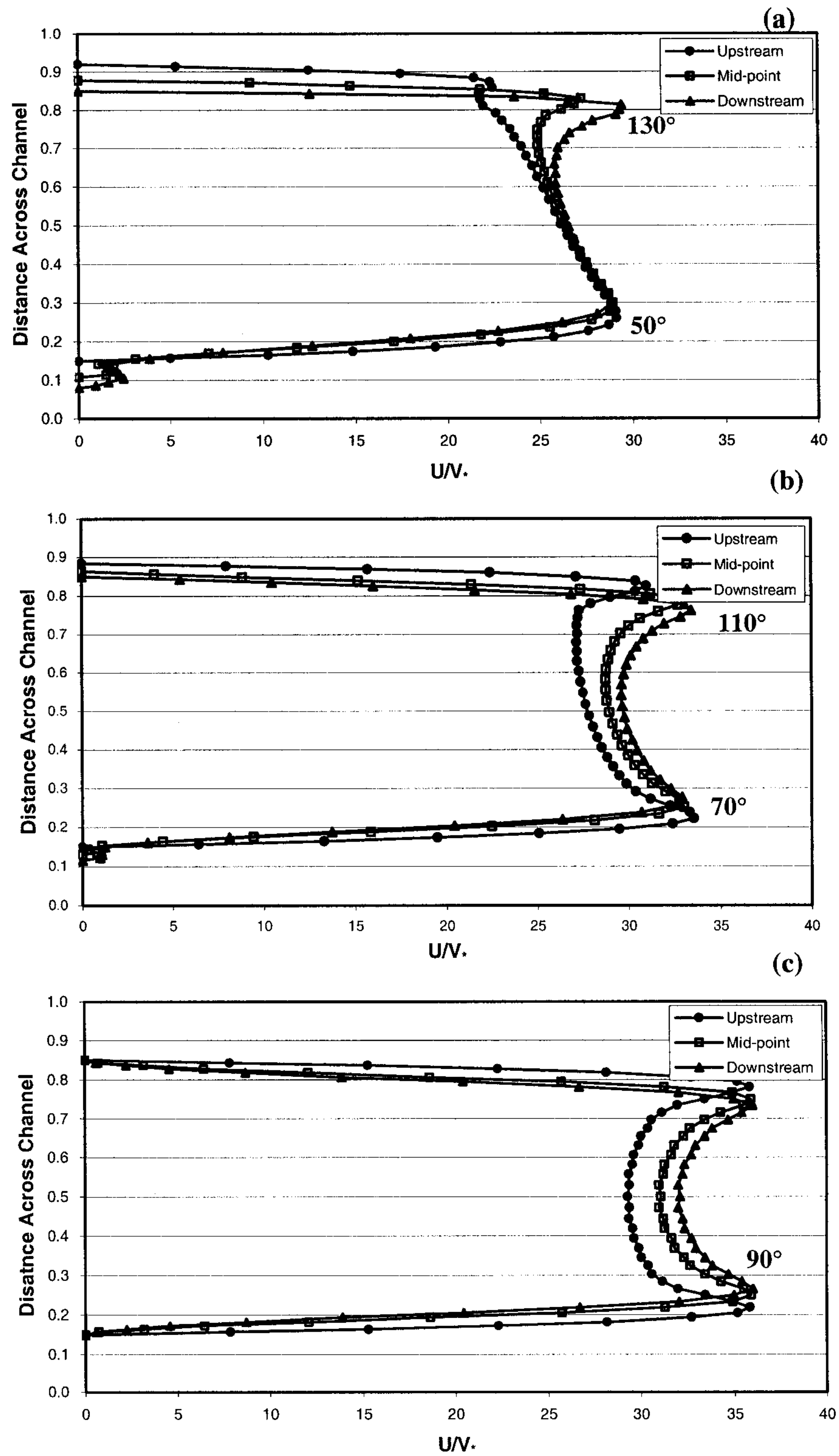

Figure 3.11 Velocity profiles for contracted reach for double abutments: (a) $\theta =$ 50° and 130°; (b) $\theta =$ 70° and 110°; (c) $\theta =$ 90°.

Table 3.2 Resultant maximum velocities for double abutments.

ϕ	Locations	$f = 0.08$		$f = 0.02$		$f = 0.0088$	
		U_{max}/V_*	U_{max}/U_{app}	U_{max}/V_*	U_{max}/U_{app}	U_{max}/V_*	U_{max}/U_{app}
50°	Upstream	14.40	1.44	29.14	1.46	45.69	1.52
	Mid-Point	14.30	1.43	28.80	1.44	45.37	1.51
	Downstream	14.21	1.42	28.79	1.44	45.39	1.51
60°	Upstream	15.18	1.52	31.79	1.59	49.07	1.64
	Mid-Point	15.08	1.51	31.33	1.57	47.97	1.60
	Downstream	15.06	1.51	31.20	1.56	48.14	1.60
70°	Upstream	15.98	1.60	33.55	1.68	51.67	1.72
	Mid-Point	15.90	1.59	33.00	1.65	50.86	1.70
	Downstream	15.88	1.59	32.90	1.65	50.66	1.69
80°	Upstream	16.77	1.68	34.98	1.75	53.55	1.78
	Mid-Point	16.76	1.68	34.67	1.73	53.33	1.78
	Downstream	16.82	1.68	34.46	1.72	53.42	1.78
90°	Upstream	17.19	1.72	35.84	1.79	54.56	1.82
	Mid-Point	17.51	1.75	35.89	1.79	54.77	1.83
	Downstream	17.52	1.75	35.99	1.80	54.85	1.83
100°	Upstream	16.25	1.63	33.59	1.68	51.34	1.71
	Mid-Point	16.97	1.70	34.52	1.73	52.43	1.75
	Downstream	17.19	1.72	34.66	1.73	52.26	1.74
110°	Upstream	15.12	1.51	30.99	1.55	47.61	1.59
	Mid-Point	16.23	1.62	32.88	1.64	50.02	1.67
	Downstream	16.65	1.66	33.42	1.67	50.57	1.69
120°	Upstream	13.70	1.37	28.07	1.40	42.23	1.41
	Mid-Point	15.35	1.54	30.87	1.54	46.69	1.56
	Downstream	16.07	1.61	31.88	1.59	48.40	1.61
130°	Upstream	12.24	1.22	22.46	1.12	36.41	1.21
	Mid-Point	14.34	1.43	27.24	1.36	42.82	1.43
	Downstream	15.37	1.54	29.42	1.47	45.22	1.51

3.10. Analysis on the Maximum Velocity

The maximum velocity amplifications corresponding to each angle are summarized and presented in Figure 3.12 along the 3 observation lines for both single and double abutment cases. From this figure, it can be seen that the maximum computed velocity amplifications are obtained for abutments placed perpendicular to the flow for both cases. The difference between maximum velocities corresponding to skewed single and double abutments can be up to 35 % especially for double abutments. The difference of velocity profiles along the plotting lines is smallest for $\theta = 90^\circ$, and increases with excessive deviation from 90° case.

Table 3.3 summarized for maximum velocities only for double abutments corresponding to 3 different friction factors. As a result, the maximum total velocity increases proportionally with the skewness angle up to 90°; beyond 90°, it decreases. Based on these results, a nonlinear regression analysis was conducted to relate the maximum total velocity to skewness angle for different roughness values using a fixed projection ratio of $\sigma = 0.3$. The derived relationship is a Lorenzian-type function. The coefficients of this relationship are listed in Table 3.3 with the correlation coefficients, r^2. The proposed velocity amplification equation with skewness angle correction, k_θ, derived from the nonlinear statistical analysis is

$$\frac{U_{nose}}{U_{app.}} = \frac{\alpha F(\sigma, f)}{\left\{1 + \left[\frac{(\theta - \beta)}{\gamma}\right]^2\right\}} = k_\theta F(\sigma, f) \qquad (3.9.1)$$

where, θ = skewness angle in radians.

Table 3.3 Coefficients of Equation (3.9.1) from nonlinear statistical analysis.

f	Coefficients	Upstream	Mid-point	Downstream
0.08	$F(\sigma,f)$	1.5948	1.6134	1.6249
	α	1.06	1.06	1.06
	β	1.4649	1.5876	1.6648
	γ	1.3173	1.5308	1.6767
	r^2	0.9757	0.9670	0.9704
0.02	$F(\sigma,f)$	1.6806	1.6672	1.6619
	α	1.06	1.06	1.06
	β	1.4505	1.5438	1.5941
	γ	1.1562	1.3731	1.5126
	r^2	0.9700	0.9840	0.9820
0.0088	$F(\sigma,f)$	1.7061	1.6910	1.6861
	α	1.06	1.06	1.06
	β	1.4370	1.5287	1.5660
	γ	1.2300	1.4599	1.5967
	r^2	0.9845	0.9810	0.9652

The values of the function $F(\sigma,f)$ given in Table 3.3, correspond to the straight abutment case ($\theta=90^\circ$). The coefficient α is a constant and β controls the angle which maximum velocity amplification takes place. As can be seen from Table 3.3, the parameter β increases in the direction of flow, going from upstream to downstream. Accordingly, maximum amplification takes place further downstream with increasing β. The parameter γ controls the rate of variation of velocity amplification with angle; as its value increases, velocity variation with skewness angle becomes smaller.

The functional behavior of Equation (3.9.1) is shown in Figure 3.13 for different friction factors. Figure 3.13(a) is for $f=0.08$; Figure 3.13(b) is for $f=0.02$; and Figure 3.13(c) is for $f=0.0088$, respectively. The variation of the friction factor f for a given skewness affects the maximum velocity amplification. Figure 3.14 is given to show the relationship between friction factor, f, and maximum velocity amplification.

In general, the smaller value of friction factor (smoother boundary), f, results in higher total velocity regardless of angle. Therefore, skewness effect is independent of f, and friction effects can be accommodated by $F(\sigma, f)$ alone.

In deriving Equation (3.9.1), the contraction ratio σ is kept constant at 0.3 and the function $F(\sigma, f)$ represents the maximum velocity for the perpendicular case. This relationship can be combined with the equation derived by Molinas and Hafez (2000) for abutment nose velocity amplification for straight abutments. Molinas and Hafez related maximum velocity amplification to contraction ratio and the roughness factor according to

$$\frac{U_{nose}}{U_a} = \frac{1-\sigma^2 \ln f/2}{1-\sigma} \tag{3.9.2}$$

where, U_{nose} is the total velocity at the abutment nose; U_a is the approach velocity at the inlet. Since U_{nose} for the 90° case represents $U_{\max}$ at the upstream, it is possible to replace U_{nose} with $U_{\max}$ which is the maximum velocity at the upstream, mid-point, and downstream along the abutment. The combined equation can be written as

$$\frac{U_{\max}(\theta)}{U_a} = \frac{\alpha(1-\sigma^2 \ln f/2)}{1-\sigma}\left\{1+\left[\frac{(\theta-\beta)}{\gamma}\right]^2\right\}^{-1} \tag{3.9.3}$$

where, 6 = skewness angle in radians.

and values of the coefficients α, β, and γ for different roughness coefficients can be combined and take average values. This results in an expression for skewness angle correction, k_θ, and independent of friction factor f. The combined values are listed as follows.

- Upstream: $\alpha = 1.06$; $\beta = 1.4508$; $\gamma = 1.2345$
- Mid-point: $\alpha = 1.06$; $\beta = 1.5534$; $\gamma = 1.4546$
- Downstream: $\alpha = 1.06$; $\beta = 1.6083$; $\gamma = 1.5953$

The maximum velocity amplifications from Equation (3.9.3) and the results from the FEM model are compared in Figure 3.15 using the above listed values of α, β, and γ. The agreement between Equation (3.9.3) and the FEM model is very close and the deviation is within ±3 %.

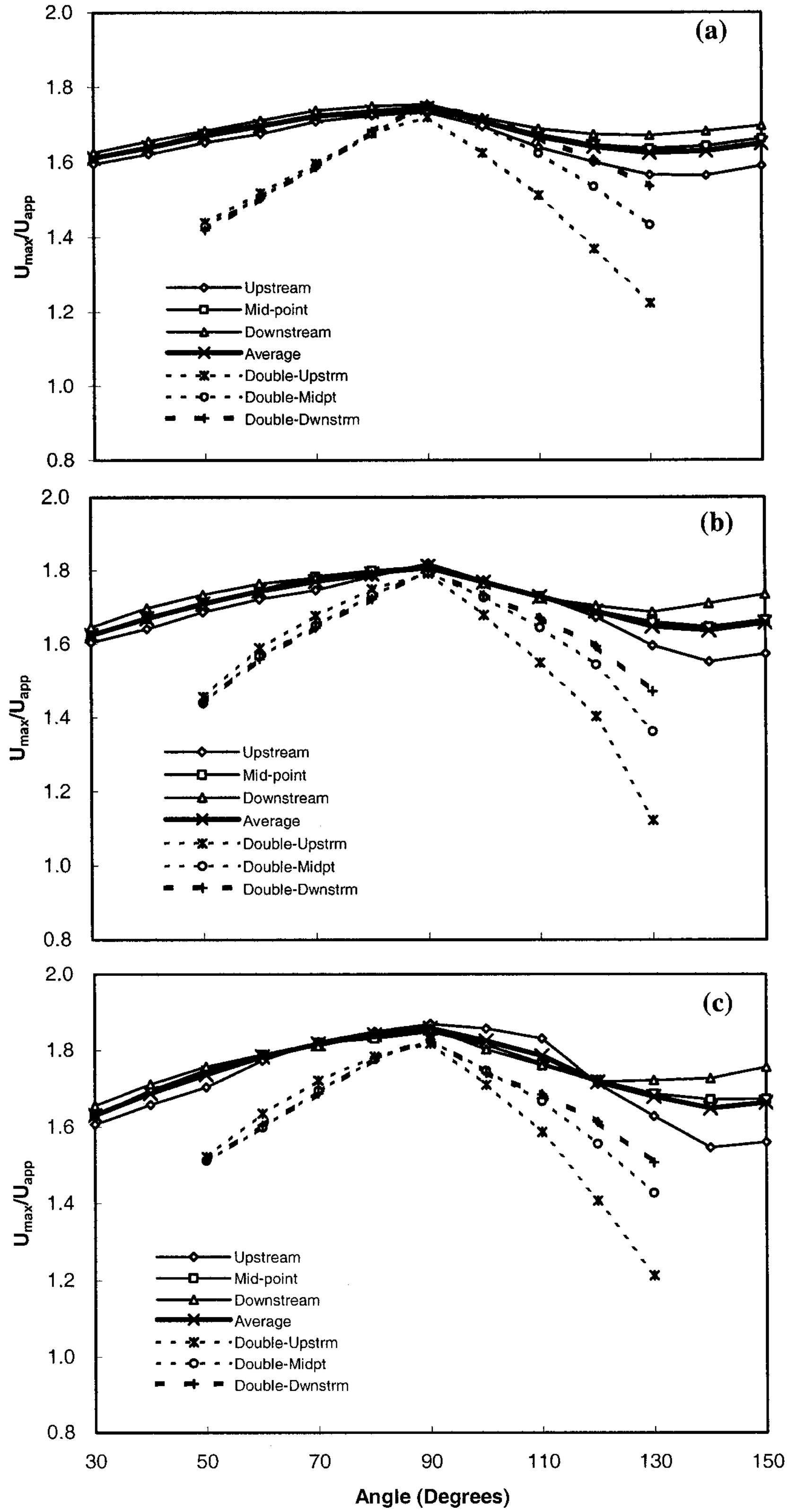

Figure 3.12 Variation of velocity amplification with skewness: (a) $f = 0.08$; (b) $f = 0.02$; (c) $f = 0.0088$.

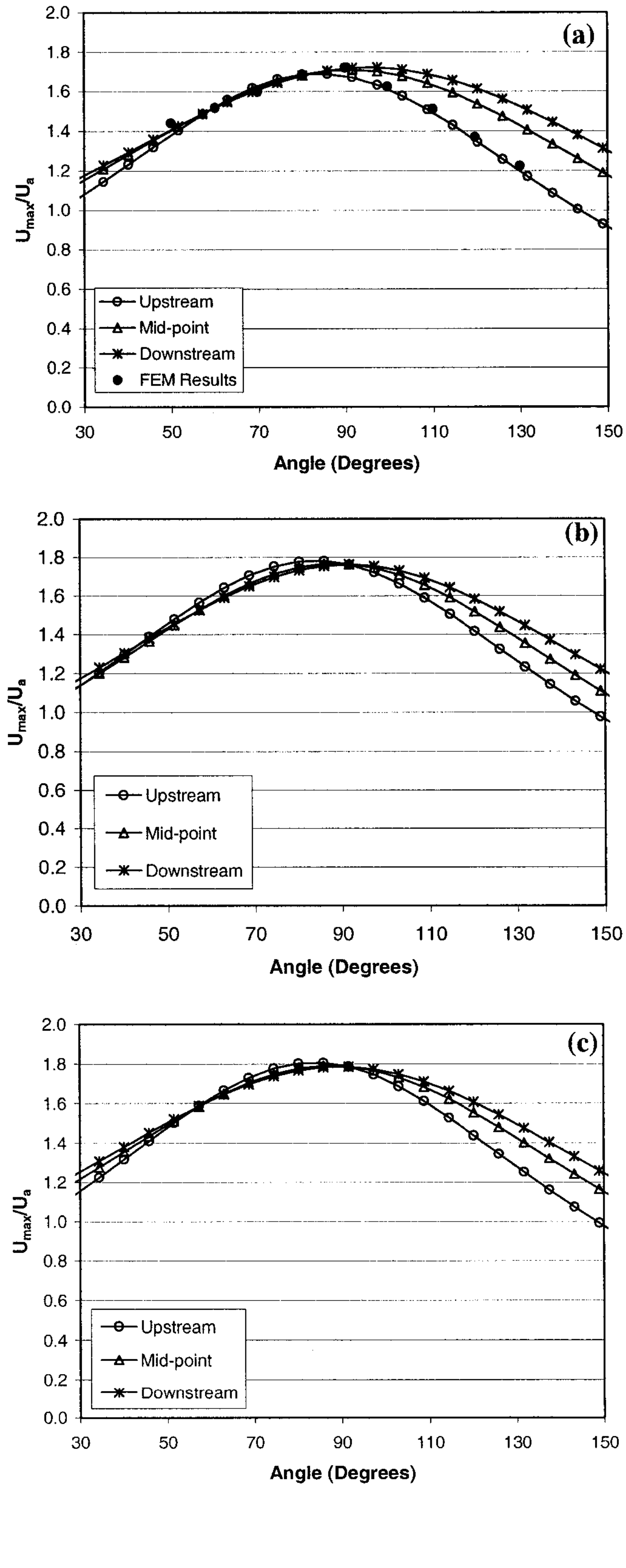

Figure 3.13 Variation of maximum velocities with skewness angle using Equation (3.9.3) with: (a) $f = 0.08$; (b) $f = 0.02$; and (c) $f = 0.0088$.

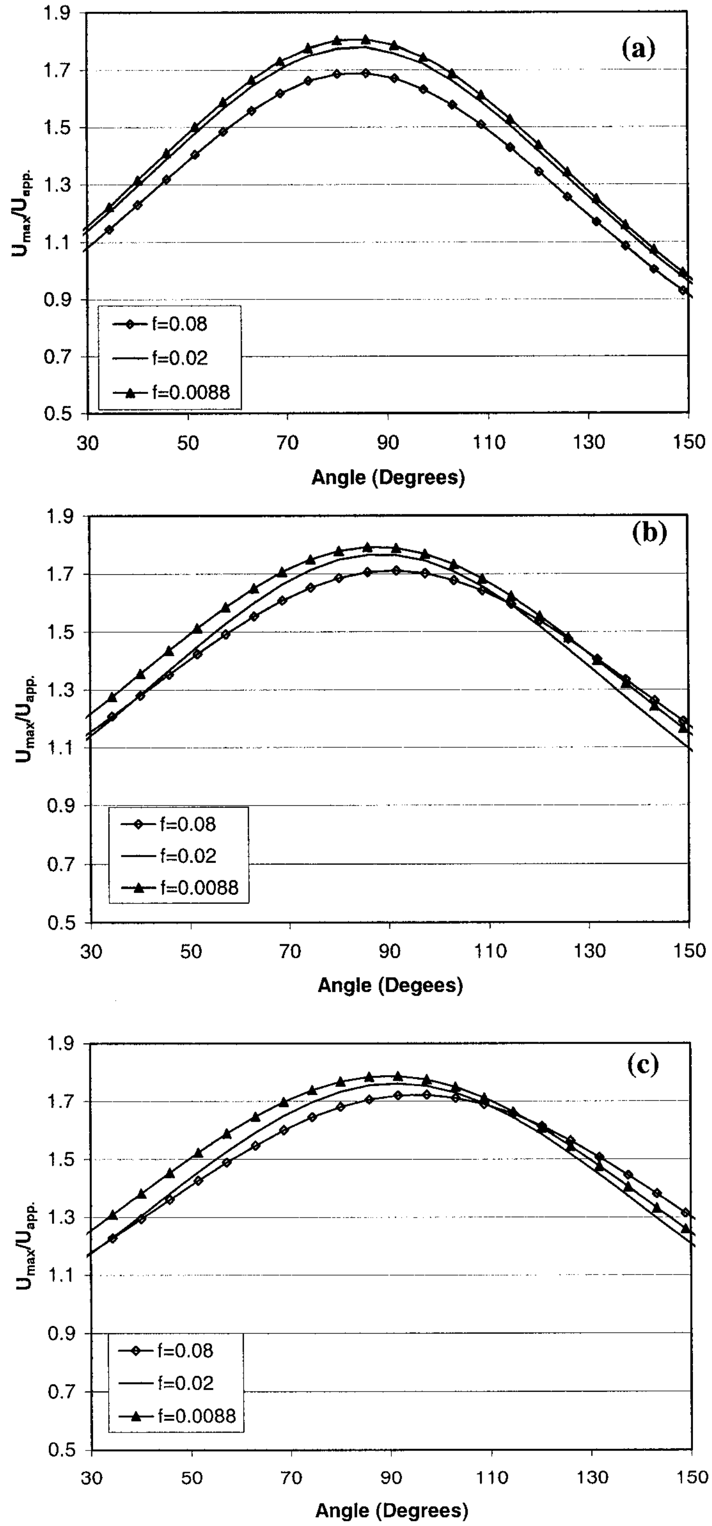

Figure 3.14 Relationship between maximum velocities and skewness angle from Equation (3.9.3) for different *f* values at: (a) upstream; (b) mid-point; and (c) downstream station.

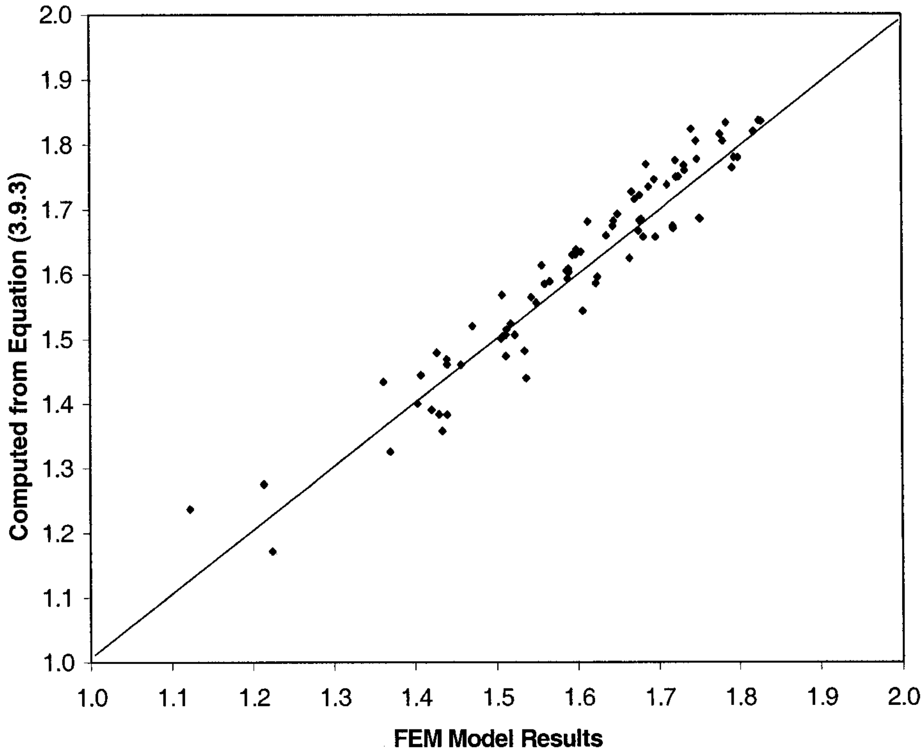

Figure 3.15 Comparison of maximum velocities computed from the FEM model and from Equation (3.9.3).

3.11. Summary

In this chapter, using upwind finite element scheme to solve the Navier-Stokes equations, a finite element hydro-dynamic model is proposed and applied for the analysis of the flow distributions in the contracted reach due to bridge abutments. The notable difference between the upwind scheme and standard scheme lies in the choice of the weighting function. The upwind scheme introduces the balancing diffusion terms into the convection terms and it provides numerical stability to reduce numerical oscillations encountered in convection dominated flow problems.

The model application is on the flow distributions in the channel contractions assuming that bridge abutments are not always perpendicular. The flow distribution analysis focuses on the contracted reach due to the single and double abutment placed with skewness. In the analysis, flow velocity profile is obtained along the 3 different plotting to investigate and compare the maximum velocity variations due to the skewness angle change.

As a conclusion for single abutment cases, the maximum velocities corresponding to the skewness angle increased proportionally according to the angle variations up to 90°. Beyond the perpendicular angle to the flow direction, the maximum value decreases with angle increase. When the skewness angle is greater than 90°, the possible maximum velocities are little less than that of 90°. It is also found that the friction factor does not alter the trends of flow velocity distribution significantly. From the double abutment runs, the skewness angle affects the velocity distributions more than single abutment cases. The difference between maximum nose velocities corresponding to the angle of 50° and 90° is approximately 25 percent and the difference between 90° and 130° is 30 percent. The peak value of velocities obtained for the perpendicular case for single and double abutments. The skewness angle effect plays more significant role double abutment cases regardless of the same contraction ratio in both cases.

An analytical expression is derived to express the maximum velocity in terms of contraction ratio, friction factor, and skewness angle. Based on numerical results, this equation is obtained from nonlinear regression. The range of the discrepancy between this analytical equation and numerical result is within ±3 % error.

CHAPTER 4

4. SEDIMENT TRANSPORT MODELING IN CHANNEL CONTRACTIONS

This chapter presents the model algorithm for the sediment transport using the finite element upwind scheme. Separate sediment transport models for bed load and suspended load transport are developed and applied to the Mississippi River after model verification. Solving the sediment continuity equation, the bed load transport model is proposed to conduct numerical simulation for bed elevation changes in the channel contractions. Also, the suspended load transport model is developed to determine concentration distributions and the propagation of the suspended load in the flow domain. For the algorithm, finite element upwind scheme is employed to provide numerical stability to the convection dominated flow such as the flow in channel contractions and the model application is focused on the real time simulation of the suspended load transport.

The hydrodynamic model can determine shear stress distribution from the flow velocity to identify the potential of the scour on the channel bed. Therefore, by applying the bed load transport equations, it is possible to predict the movement of the particles on channel bottom. From the bed load transport theory introduced in Chapter 2, the particle will not move until the shear stress exceeds the threshold condition. Thus, the bedload transport equation can be expressed mathematically in terms of the difference between the shear stress and critical shear stress.

While the bed load transport frequently occurs in contact with channel bed, the fine material such a silts and clay particles move in suspended state. These fine materials are called as suspended load and its transport process is well explained by the convection and diffusion equation. The simulation result in each time step shows the propagation of suspended load in 2-dimensional plane view. The model is applicable not only for continuous but also for non-continuous load. In addition, the model can predict the propagation of the suspended load as well as contaminants or heat transfer with proper modification. Since the flow in the channel contraction is highly convective, upwind finite element formulation is incorporated into the model development to provide numerical stability.

4.1. Bed load Transport

The scour problem is due to the removal of the channel bed materials where the magnitude of shear stress exceeds the critical shear stress that initiates particle motion. Usually in higher shear zones, such as in the channel contractions, the scour process is predominant. In computing the scour depth, it is necessary to determine the amount of the sediment transported due to excess shear stress. The eroded bed materials from high shear zones are expected to be deposited or remain in suspended state where the shear stress is less than the weight of particle. These processes result in channel bed evolution and it can be described by solving the sediment continuity equation linked with the bed load transport equation.

4.1.1. The sediment continuity equation

A typical two-dimensional sediment continuity equation is given as follow

$$(1-\lambda)\frac{\partial Z}{\partial t}+\frac{\partial q_{sx}}{\partial x}+\frac{\partial q_{sy}}{\partial y}=0.0 \tag{4.1.1}$$

where, $\lambda =$ porosity, $Z =$ bed elevation, q_{sx} = the amount of sediment due to the x-component of the flow velocity, q_{sy} = the amount of sediment due to the y-component of the flow velocity.

When the water flows past a rigid boundary of hydraulic structures, the fluid viscosity and the accompanying velocity gradient can cause tangential friction force which exerts a dynamic force on that boundary. This tangential force referred to shear stress. In open channel flows, the shear stress can be computed from

$$\tau = \gamma_f R S_E \tag{4.1.1}$$

where, γ_f = specific weight of the fluid, $R =$ the hydraulic radius, S_E = slope of the energy grade line.

The amount of sediment corresponding to a certain level of shear stress can be determined by relating the transport to an excess shear stress defined as the difference between shear stress and the critical shear stress according to

$$\begin{array}{ll} q_s = \alpha(\tau - \tau_c)^\beta & \tau_c \le \tau < \tau_c' \\ q_s = 0 & \tau < \tau_c \\ q_s = q_{\max} & \tau \ge \tau_c' \end{array} \tag{4.1.2}$$

where, τ_c = critical shear stress required to set bed materials into the motion; τ_c' = limiting shear stress beyond which no additional bed load transport takes place; and τ = shear stress due to the flow velocity.

In open channel flows, using Manning's roughness coefficient n, the definition of the energy slope is

$$S_E = \rho g \frac{n^2 |V| V}{(H + h)^{4/3}} \tag{4.1.3}$$

The shear stress τ can be obtained by substituting Equation (4.1.3) into (4.1.1).

$$\tau = \rho g \frac{n^2 |V| V}{(H + h)^{1/3}} \tag{4.1.4}$$

where, $n =$ Manning's roughness coefficient.

From Equation (2.8.31), and using particle diameter d_{90} for which 90 percent of bed material is finer by weight, it is possible to relate roughness to bed material size.

$$n = \frac{d_{90}}{26} \tag{4.1.5}$$

The critical shear stress τ_c is defined from the Shields diagram and is expressed as

$$\tau_c = A(\rho_s - \rho) g d \tag{4.1.6}$$

where, ρ_s = sediment density, g = gravity acceleration, d = sediment diameter and the coefficient A can be determined following Yalin's suggestion (1972),

$$\tau_c = (\rho_s - \rho) g d_{50} \theta_c \tag{4.1.7}$$

with

$$\begin{aligned}
\theta_c &= 0.24 d_*^{-1} && \text{for} \quad 1 < d_* \le 4 \\
\theta_c &= 0.14 d_*^{-0.64} && \text{for} \quad 4 < d_* \le 10 \\
\theta_c &= 0.04 d_*^{-0.1} && \text{for} \quad 10 < d_* \le 20 \\
\theta_c &= 0.013 d_*^{0.29} && \text{for} \quad 20 < d_* \le 150 \\
\theta_c &= 0.055 && \text{for} \quad d_* > 150
\end{aligned} \tag{4.1.8}$$

where, $d_* = d_{50} \left[\frac{(G-1) g}{v_m^2} \right]^{1/3}$

In the presence of strong streamline curvatures such as those encountered near abutment noses, some corrections to shear stress are necessary. Tingsanchali and Maheswaran (1990) used 2D depth averaged standard $\kappa - \varepsilon$ turbulence model for the correction of the effect of streamline curvature to solve the flow problem near groins protrusions. The following formulae have been used to compute the bottom shear stress around groins.

$$\tau_{bx} = \rho k_{bc} U \sqrt{U^2 + V^2} \tag{4.1.9a}$$

$$\tau_{by} = \rho k_{bc} V \sqrt{U^2 + V^2} \tag{4.1.9b}$$

The roughness coefficient, k_{bc}, in the above equation is obtained by correcting the given k_b with streamline curvature. The roughness factor, k_b, is related to Chézy roughness coefficient C according to

$$k_b = \frac{g}{C^2} \tag{4.1.10}$$

The Chézy C is related to a commonly used Darcy-Weisbach friction factor f using the following relationship between velocity and shear stress

$$\frac{U}{V_*} = \frac{U}{\sqrt{\tau/\rho}} = \sqrt{\frac{8}{f}} = \frac{C}{\sqrt{g}} \tag{4.1.11}$$

Tingsanchali and Maheswaran (1990) modified Johnston (1960)'s 3D flow correction in order to find appropriate shear stress at the tip of a groin. The resulting corrected roughness factor is given as

$$k_{bc} = k_b \sqrt{1 + \tan^2(M_\alpha \alpha_o)} \tag{4.1.12}$$

where, $M_\alpha = \alpha_w / \alpha_o$; α_w = turning angle between bottom stream line and the main flow direction (or the surface stream line direction); and α_o = turning angle between the main flow and the upstream approach flow direction. The experimental study conducted by Rajanatnam and Nwachukwu (1983) defined the variation of the ratio α_w / α_o along the flow with distance. Rajanatnam and Nwachukwu (1983) stated that the values of α_o at the nose were relatively constant for the range of their experimental conditions.

Applying the curvature correction accounts for the turning angle in the nose region of abutments gives closer results to measured stresses at the nose region of the abutment. Using Rajanatnam and Nwachukwu (1983)'s experimental data, Tingsanchali and Maheswaran (1990) found the correction coefficient M_α in Equation (4.1.12) to be equal to 2. Since Equation (4.1.12) is a tangential function of the turning angle, if the angle α_o is around 45°, the value of corrected friction factor k_{bc} will be infinitely large, which is impossible. Tingsanchali and Maheswaran (1990) addressed that the correction coefficient M significantly improves the computed bottom shear stress near the tip of the groin; however, this formulation does not alter the computed velocity field significantly.

Molinas and Kheireldin (1998) investigated the shear stress amplification at the abutment nose region for abutments placed perpendicular to flow. They defined the shear amplification factor Λ_{nose} as the ratio of nose shear stress in excess of approach shear stress as

$$\Lambda_{nose} = \frac{\tau_{nose} - \tau_{app}}{\tau_{app}} = \frac{\rho k_{bc} V_{nose}^2}{\rho k_b V_{app}^2} - 1 \qquad (4.1.13)$$

For the present analysis, the shear stress distribution is obtained by using the hydrodynamic model. These results are compared with the laboratory experimental study done by Kheireldin (1994) that was conducted in a recirculating flume with an adjustable slope. Molinas, Kheireldin and Wu (1998) presented the result of their shear stress analysis for vertical wall abutments and found that the high shear stress amplification is found at the nose of the abutment.

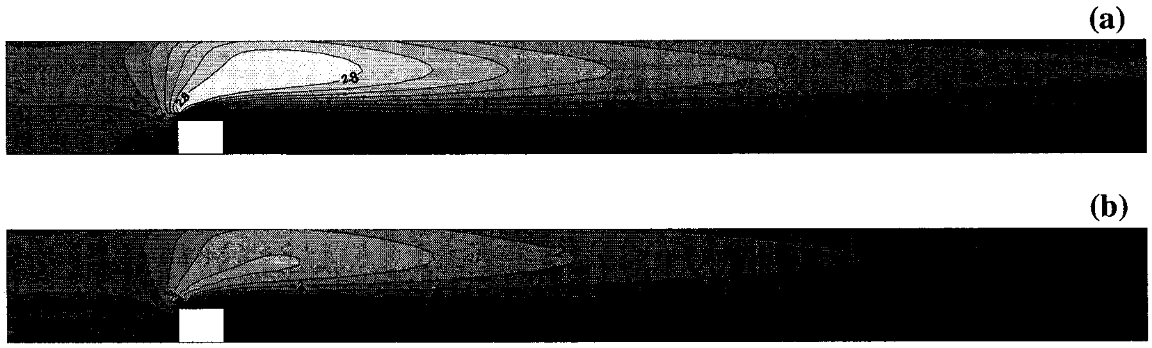

Figure 4.1 Shear stress distributions (a) without curvature correction (b) with curvature correction.

For the case of 0.3 contraction ratio, they reported the maximum value of the amplification factor Λ_{nose} to be as high as 8 ~ 9. In the present numerical simulations, amplification ratios are close to the experimental results when the curvature correction is applied in the abutment nose region according to Molinas et al (1998). Figure 4.1 shows shear stress distributions with and without curvature corrections. From this figure, the curvature correction yields a maximum amplification ratio of 8.42. Without curvature correction, the ratio of the maximum amplification factor is 3.21.

4.1.2. Finite element formulation of the governing equation

For finite element discretization, multiplying the weighting function to the sediment continuity equation yields

$$\delta Z\left[\dot{Z}+\frac{\partial q_{sx}}{\partial x}+\frac{\partial q_{sy}}{\partial y}\right]=0.0 \tag{4.1.14}$$

where,

$$\dot{Z}=(1-\lambda)\frac{dZ}{dt} \tag{4.1.15}$$

Using the finite element approximation, obtains each term as

$$\dot{Z}=\lfloor N\rfloor\{\dot{Z}\} \tag{4.1.16}$$

$$\frac{\partial q_{sx}}{\partial x}=\left\lfloor\frac{\partial N}{\partial x}\right\rfloor\{q_{sx}\} \text{ and } \frac{\partial q_{sy}}{\partial y}=\left\lfloor\frac{\partial N}{\partial y}\right\rfloor\{q_{sy}\} \tag{4.1.17}$$

Substituting these finite element approximations into the weak form yields the following finite element equation for an element

$$\delta J_e=\int_{Ve}\lfloor\delta Z\rfloor\{N\}\lfloor N\rfloor\{\dot{Z}\}dV+\int_{Ve}\lfloor\delta Z\rfloor\{W\}\left\lfloor\frac{\partial N}{\partial x}\right\rfloor\{q_{sx}\}dV+\int_{Ve}\lfloor\delta Z\rfloor\{W\}\left\lfloor\frac{\partial N}{\partial y}\right\rfloor\{q_{sy}\}dV \tag{4.1.18}$$

Adapting the Petrov-Galerkin weighting function,

$$W_i=N_i+\frac{H_x}{2}\frac{dN_i}{dx} \tag{4.1.19a}$$

or,

$$W_i=N_i+\frac{H_y}{2}\frac{dN_i}{dy} \tag{4.1.19b}$$

where, H_x and H_y are the element lengths in x and y directions, respectively.

The second and third integral terms in Equation (4.1.18) are easily obtained by using the finite element formulation. The first integral term in Equation (4.1.18) which is in front of the time derivative term is defined as the capacity matrix and is given by

$$[C]_e = \int_{V_e} \{N\}\lfloor N \rfloor dV \tag{4.1.20}$$

The sediment continuity equation for the entire domain becomes

$$[C]\{\dot{Z}\} + \{Q'\} = 0 \tag{4.1.21}$$

Once the unsteady term $\dot{Z}$ is known, it is possible to integrate with respect to time in order to obtain Z at a later time. Applying simple Eulerian integration it gives

$$\{Z\}_{t+\Delta t} = \{Z\}_t + \{\dot{Z}\}_t \Delta t \tag{4.1.22}$$

that is,

$$\{\dot{Z}\}_t = \frac{1}{\Delta t}[\{Z\}_{t+\Delta t} - \{Z\}_t] \tag{4.1.23}$$

Substituting Equation (4.1.23) into Equation (4.1.21) gives

$$\frac{[C]}{\Delta t}[\{Z\}_{t+\Delta t} - \{Z\}_t] = -\{Q'\} \tag{4.1.24}$$

Finally, solving Equation (4.1.24) for $\{Z\}_{t+\Delta t}$ to obtain

$$\{Z\}_{t+\Delta t} = -\{Q'\}\frac{\Delta t}{[C]} + \{Z\}_t \tag{4.1.25}$$

The Equation (4.1.23) is simply the forward difference approximation of $\{\dot{Z}\}$ at time t. This method corresponds to the explicit method used in finite difference approximations.

4.1.3. Lumped capacitance matrix

In order to obtain $\{\dot{Z}\}$ from equation (4.1.21), it is necessary to invert the capacitance matrix $[C]$. Equation (4.1.21) for a specific time step t is given in matrix form as

$$[C]\{\dot{Z}\}_t = -\{Q'\}_t \tag{4.1.26}$$

As it can be seen from above equation, if the capacitance matrix $[C]$ is diagonal, $\{\dot{Z}\}$ can be easily obtained by back substitution. In an effort to achieve this convenience, several methods are available for capacitance matrix diagonalization.

The physical interpretation of this approximation is that a distributed capacitance is replaced by many point capacitances. This is similar to replacing a distributed source by point sources. As long as total lumped capacitance is the same as the total capacitance of the element, changing the character of the material from one that has a continuously distributed capacitance to one that has many closely placed point capacitances should not alter the gross behavior being modeled. Therefore, convergence is expected when such an approximation is used. The concept and details on the lumped matrix is explained in Appendix C.

4.2. Suspended Load Transport

The total sediment load usually defines the sum of the bed load and suspended load. In this section, the governing equation for suspended sediment transport is solved using the finite element method. The suspended load is defined as that part of sediment load carried in suspension without contact with the bed. Sediment particles are brought into suspension when flow velocities are sufficiently large to keep the mass of particles from settling on the bed. In high velocity zones, increased flow velocity due to channel contractions will accelerate transport processes and diffusions. This section presents finite element algorithm with model verification and discusses the problems which encountered in the convection dominated flow.

4.2.1. Finite element formulation

As previously discussed in Chapter 2, well known convection diffusion equation is employed as its governing equation to explain the suspended load transport. The two dimensional convection and diffusion equation can be written as

$$\frac{\partial \phi}{\partial t}+U\frac{\partial \phi}{\partial x}+V\frac{\partial \phi}{\partial y}=\frac{\partial}{\partial x}\left[\varepsilon_x\frac{\partial \phi}{\partial x}\right]+\frac{\partial}{\partial y}\left[\varepsilon_y\frac{\partial \phi}{\partial y}\right]+Q \tag{4.2.1}$$

where, Q, ε_x, and ε_y are the source term and turbulent mixing coefficients respectively and, can be a function of *x*, *y*, and *t*. First, multiplying Equation (4.2.1) by the weighting function gives

$$\int_V \delta\phi\left\{\frac{\partial \phi}{\partial t}+U\frac{\partial \phi}{\partial x}+V\frac{\partial \phi}{\partial y}-\frac{\partial}{\partial x}\left[\varepsilon_x\frac{\partial \phi}{\partial x}\right]-\frac{\partial}{\partial y}\left[\varepsilon_y\frac{\partial \phi}{\partial y}\right]-Q\right\}dV \tag{4.2.2}$$

$$\int_V \delta\phi\left\{\frac{\partial \phi}{\partial t}+U\frac{\partial \phi}{\partial x}+V\frac{\partial \phi}{\partial y}-Q\right\}dV-\int_V \delta\phi\left\{\frac{\partial}{\partial x}\left[\varepsilon_x\frac{\partial \phi}{\partial x}\right]+\frac{\partial}{\partial y}\left[\varepsilon_y\frac{\partial \phi}{\partial y}\right]\right\}dV \tag{4.2.3}$$

Applying the integration by part to the diffusion terms

$$\int_V uv'=\int_S uv-\int_V u'v \tag{4.2.4}$$

the weak form of this Equation (4.2.3) is obtained as

$$\int_V \delta\phi\left\{\frac{\partial \phi}{\partial t}+U\frac{\partial \phi}{\partial x}+V\frac{\partial \phi}{\partial y}-Q\right\}dV+\int_V\left\{\frac{\partial \delta\phi}{\partial x}\varepsilon_x\frac{\partial \phi}{\partial x}+\frac{\partial \delta\phi}{\partial y}\varepsilon_y\frac{\partial \phi}{\partial y}\right\}dV-\int_S \delta\phi q ds=0.0 \tag{4.2.5}$$

By considering ϕ and $\partial\phi/\partial t$ as two independent variables and defining $\dot{\phi}$ as

$$\dot{\phi}=\frac{\partial \phi}{\partial t} \tag{4.2.6}$$

The finite element approximation for ϕ and $\dot{\phi}$ are

$$\phi(x,y) = \lfloor N \rfloor \{\phi\} \quad (4.2.7a)$$

$$\dot{\phi}(x,y) = \lfloor N \rfloor \{\dot{\phi}\} \quad (4.2.7b)$$

where $\dot{\phi}$ represent represents the nodal point values for the derivative of ϕ with respect to time. Note that we have two variables associated with each node, ϕ and $\dot{\phi}$. Substitution of these finite element approximations into the weak form gives, for a single element,

$$\begin{aligned}\delta J_e &= \int_{Ve} \lfloor \delta\phi \rfloor \{N\} \lfloor N \rfloor \{\dot{\phi}\} dV - \int_{Ve} \lfloor \delta\phi \rfloor \{N\} Q dV \\ &+ \int_{Ve} \lfloor \delta\phi \rfloor \{N\} [B] \lfloor N' \rfloor \{\phi\} dV + \int_{Ve} \lfloor \delta\phi \rfloor \{N'\} [R] \lfloor N' \rfloor \{\phi\} dV - \int_{S} \lfloor \delta\phi \rfloor \{N\} q dS\end{aligned} \quad (4.2.8)$$

where, the matrices $[B]$ and $[R]$ are given as follows, respectively.

$$[B] = \begin{bmatrix} U & 0 \\ 0 & V \end{bmatrix} \text{ and } [R] = \begin{bmatrix} \varepsilon_x & 0 \\ 0 & \varepsilon_y \end{bmatrix} \quad (4.2.9)$$

Since the convective terms are incorporated into the matrix $[B]$, applying the Petrov-Galerkin formulation to the convective terms results in

$$\begin{aligned}\delta J_e &= \int_{Ve} \lfloor \delta\phi \rfloor \{N\} \lfloor N \rfloor \{\dot{\phi}\} dV - \int_{Ve} \lfloor \delta\phi \rfloor \{W\} Q dV \\ &+ \int_{Ve} \lfloor \delta\phi \rfloor \{W\} [B] \lfloor N' \rfloor \{\phi\} dV + \int_{Ve} \lfloor \delta\phi \rfloor \{N'\} [R] \lfloor N' \rfloor \{\phi\} dV - \int_{S} \lfloor \delta\phi \rfloor \{N\} q dS\end{aligned} \quad (4.2.10)$$

Note that the weighting function W in Equation (4.2.10) is

$$W_i = N_i + \frac{\alpha h}{2|\mathbf{U}|}\left(U \frac{\partial N_i}{\partial x} + V \frac{\partial N_i}{\partial y} \right) \quad (4.2.11)$$

where, $\alpha = \coth \gamma/2 - 2/\gamma$ and $\gamma = \mathrm{Pe}|\mathbf{U}|\overline{h}$

The weighting function W from Equation (4.2.11) is applied for the convective and source terms while the shape function is used as the weighting for the diffusion terms. It should be noted that when transient algorithm and bilinear elements are used, it suffices to weight the convective terms in the right-hand-side with the above weighting functions. For this reason, it is desirable to use a second-order time stepping scheme. However, for many engineering applications a first-order-method is sufficient.

The governing equation can be summarized in a finite element matrix form as

$$\delta J_e = \lfloor \delta\phi \rfloor [C]_e \{\dot{\phi}\}_e - \lfloor \delta\phi \rfloor \{Q\}_e + \lfloor \delta\phi \rfloor [K]_e \{\phi\} \tag{4.2.12}$$

where, $[K]_e$ is the element stiffness matrix which includes the line integral components. δJ_e is the contribution to the weak form from element "*e*". Summation of all such contributions from elements and surface segments gives,

$$J = \lfloor \delta\phi \rfloor [C] \{\dot{\phi}\} - \lfloor \delta\phi \rfloor \{Q\} + \lfloor \delta\phi \rfloor [K] \{\phi\} \tag{4.2.13}$$

In order for this equation to be zero for all $\delta\phi$,

$$[C]\{\dot{\phi}\} + [K]\{\phi\} = \{Q\} \tag{4.2.14}$$

Note that the number of equations equals the number of values for either ϕ or $\dot{\phi}$, but not both. Therefore, these equations govern the relationship between the two variables, meaning that if ϕ were known, one could solve for $\dot{\phi}$. On the other hand, if $\dot{\phi}$ were known, the equation can be solved for ϕ. For the steady state case, $\dot{\phi}$ is known (i.e. equal to zero), and the equation can be solve for ϕ.

4.2.2. Mixed boundary conditions

For mixed boundary conditions, e.g. those that arise in heat transfer problems,

$$q = C_h(\phi_a - \phi) \tag{4.2.15}$$

It is only necessary to substitute the above equation for q into the finite element equations. That is,

$$
\begin{aligned}
\{q_s\} &= \int_S \{N_s\} q(s)\, ds \\
&= \int_S \{N_s\} C_h (\phi_a - \phi) ds \qquad (4.2.16) \\
&= \int_S \{N_s\} C_h \phi_a\, ds - \int_S \{N_s\} C_h \phi\, ds
\end{aligned}
$$

Here, however, the last integral has the yet undetermined values of ϕ on the boundary.

$$\int_S \{N_s\} C_h \phi ds = \int_S \{N_s\} C_h \lfloor N_s \rfloor \{\phi\} ds \qquad (4.2.17)$$

Therefore, substituting the finite element approximation for this function results in

$$[k_s]\{\phi\} = \int_S \{N_s\} C_h \lfloor N_s \rfloor \{\phi\} ds \qquad (4.2.18)$$

This new surface stiffness matrix must be assembled into the global stiffness matrix in the same manner as the element stiffness matrices are assembled. The integral involving the known external concentration gives a source type term for each node along the element's side and is assembled into the RHS matrix.

It is now necessary to decide how C_h, convective coefficient, will be specified. For many applications it would be acceptable to assume that C_h is constant along an element side. However, for a more general formulation, C_h can be approximated with the shape functions and its values at the nodal points along the side of the element. Thus, for a 3-node element, C_h can be made to vary linearly along an element side, and for a 6-node element, C_h can be made to have a parabolic distribution.

When nodal values are used to specify values of boundary parameters to be used in a surface integration, e.g. *q(s)* or *h(s)*, nonzero values signal that a surface integration is necessary. During the integration of the element stiffness matrix, it is only necessary to search along each side of the current element to ascertain if there are nonzero values.

If not, then that side is either not an external boundary or, if it is, there are no distributed quantities to be integrated. Some difficulties arise at corner points since they can be associated with either of two sides. If both sides represent external boundaries, or if the distributed quantity to be integrated is nonzero on both sides, then the corner value should be the average value. If one of the two sides is not an external boundary, the non-boundary side can be determined by examining the remaining nodes along that side. For an element side to be recognized as an external boundary where a surface integration is required, all nodal point values of the specific parameter must be zero. The unlikely situation is that one of the numerical values happens to be zero along a side that it is not identically zero. Then, it must be specified as a very small number, close to zero, but not exactly equal to zero.

4.2.3. Turbulent mixing coefficients for suspended load transport

Let us consider the case of one dimensional turbulent mixing in a channel in longitudinal x direction and mass m of sediment or spill without settling or reaction at time zero at the x = 0.0. The governing one-dimensional equation will be given without a convection term as

$$\frac{\partial C}{\partial t} = \varepsilon_t \frac{\partial^2 C}{\partial x^2} \tag{4.2.19}$$

this relationship is sometimes referred as Fick's law. The analytical solution to this equation gives the concentration in terms of longitudinal distance and time as follows

$$C(x,t) = \frac{m}{A\sqrt{4\pi\varepsilon_t t}} e^{\frac{-x^2}{4\varepsilon_t t}} \tag{4.2.20}$$

where, the mass $m = \int_V C_{mg/l} dV$ is the volume integral of the concentration given through the cross sectional area A. The solution is a bell shaped curve with mean value of zero and a variance of $\sigma_t^2 = 2\varepsilon_t t$. If a conservative substance of lump sum were discharged to a water body, the properties of this normal distribution will be increased with time and its tendency to spread from the center of mass can be obtained from

$$\sigma_t = \sqrt{2\varepsilon_t t} \tag{4.2.21}$$

Turbulent mixing and dispersion are described by the coefficient of which the unit is L^2/T. The mixing is a three-dimensional process, where the vertical mixing coefficient is ε_z, the lateral mixing coefficient is ε_y, and the longitudinal dispersion coefficient is ε_x. These parameters are given as empirical functions of the variable HV_*. The vertical mixing coefficient is approximated by the turbulent eddy viscosity, i.e.

$$\varepsilon_z \cong 0.067HV_* \tag{4.2.22a}$$

where, H is depth, V_* is shear velocity.

The above equation is also correspondent to Equation (2.5.3) and Fisher et al. (1979) developed the following formula

$$\varepsilon_y \cong 0.15hV_* \text{ in straight channel} \tag{4.2.22b}$$

$$\varepsilon_y \cong 0.6hV_* \text{ in natural channel} \tag{4.2.22c}$$

$$\varepsilon_x \cong 250hV_* \text{ or } 0.011\frac{U^2B^2}{hV_*} \tag{4.2.22d}$$

where, h is flow depth, V_* is shear velocity of $\sqrt{gRS}$, and B is channel width.

4.3. Model Validation

This section presents model validation for the components of the finite element model for bed load and suspended load is presented. The bed load transport component is tested using the experimental data collected by Tanguy et al. (1987); and the suspended sediment transport component is verified using a case where an analytical solution existed. Bed load transport component verification simulates the erosion of channel bed material in a channel contraction due to the presence of the groin until equilibrium state is reached. The computed results are compared with the maximum scour depth obtained from experiments. The suspended transport model is tested using 1-D analytical equation by assuming a case where the vertical velocity and diffusion coefficients are zero.

4.3.1. Model verification of bed load transport

Using the experimental results given by Tanguy et al. (1987), the bed load transport model is verified. The parameters and experimental configurations for model verification are given as follows.

The channel width = 1.85 m, channel length = 20 m, height of the groin = 0.6m, flow discharge = 60 l/s, depth of the flow = 0.2 m, bed layer thickness = 0.2 m, respectively. From the geometrical condition of the flume, the contraction ratio of the flow area is approximately 30 %. The flow velocity of the channel inlet is computed as

$$V = \frac{Q}{A} = \frac{0.06}{0.2 \times 1.85} = 0.162 \text{ m/s} \tag{4.3.1}$$

The computational result for the flow distribution is shown in Figure 4.2. In this case, the groin is located at 3m. away from the channel inlet. The mean diameter of the sand covering the bed is given as 0.32 mm, and the critical shear stress can be computed from Equation (4.1.14). Using van Rijn's bed load transport equation, the amount of sediment that can be transported is determined from

$$q_b = 0.053\left[\left(\frac{\rho_s}{\rho}-1\right)g\right]^{0.5} d_{50}^{1.5} d_*^{-0.3} T^{2.1} \tag{4.3.2}$$

where, $d_* = d_{50}\left[(s-1)\frac{g}{v_m^2}\right]^{\frac{1}{3}}$, $T = \frac{\tau - \tau_c}{\tau_c}$

The channel bed elevation is assumed as 70 m. The plane-view contour with 3-dimensional wire frame is shown in Figure 4.3 at the end of numerical simulation. The maximum scour depth at the nose region is computed as 8.9 cm, while the maximum scour depth measured in the experiment is 11 cm. Considering the complexity of flows at the nose region (truly 3D) and the fact that the present model is used a truly 3-dimensional model, the discrepancy of 20% is encouraging. Away from the local maximum scour region, the agreement is much closer. Since the focus of this study is not the nose region, the results are acceptable.

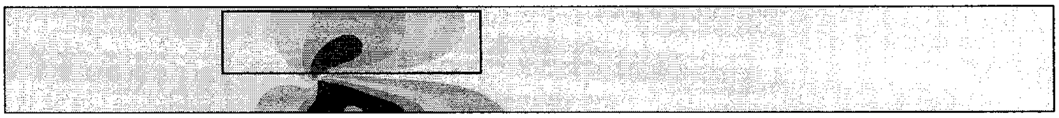

Figure 4.2 Velocity distributions and zone of the analysis.

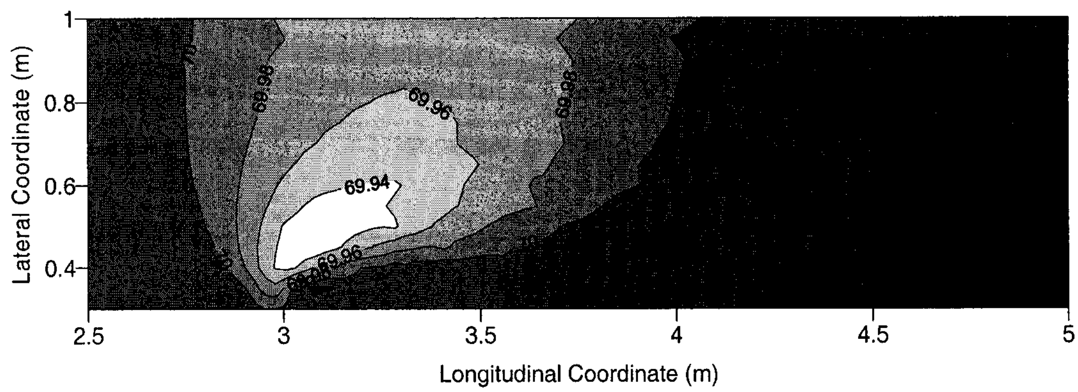

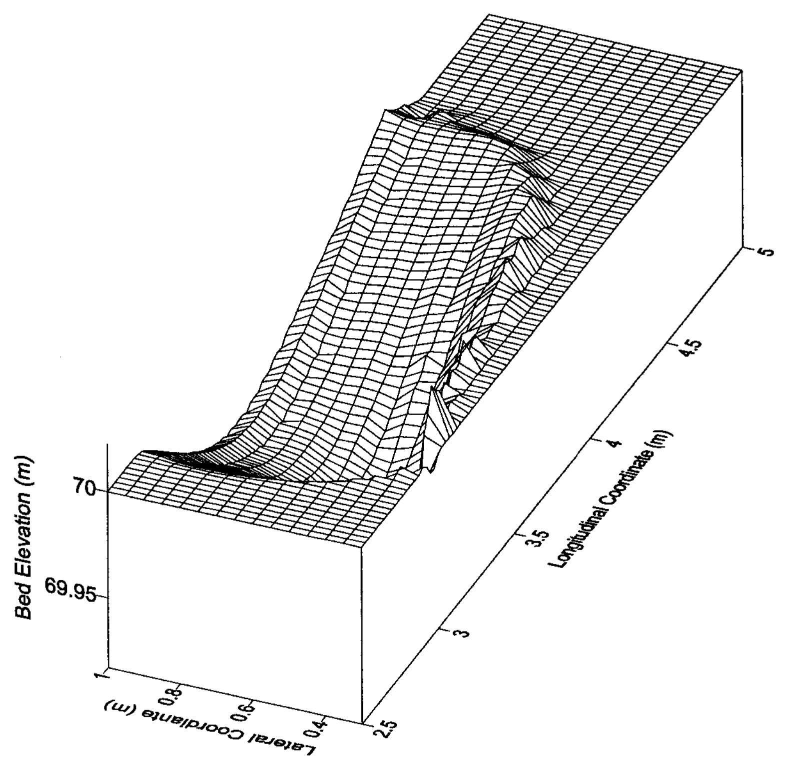

Figure 4.3 **Channel bed topographies in the contracted reach.**

4.3.2. Model validation and discussion of suspended load transport

The model is verified using a straight rectangular channel with uniform inflow conditions. By assuming $V=0$ and $\varepsilon_y=0$ in Equation (4.2.1), one-dimensional analytical equation is applicable for model validation. With addition of convective term into Equation (4.2.20), the analytical expression for one-dimensional convection and diffusion equation can be given as

$$C(x,t)=\frac{m}{A\sqrt{4\pi\varepsilon_t t}}e^{\frac{-(x-Ut)^2}{4\varepsilon_t t}} \tag{4.3.3}$$

In the example problem for model verification, a spill of 5 kg suspended load is assumed to occur about 500 m below channel inlet. The straight channel used in the example is assumed to have the following characteristics: cross sectional area A = 60 m^2, depth = 1m, width = 60 m, flow velocity U = 2400 m/hr, diffusion coefficient ε_t = 150,000 m^2/hr, and flow discharge = 144,000 m^3/hr, (After Chapra, 1997)

After substituting the above parameters, Equation (4.3.3) becomes the follwing equation which will be used for model verification.

$$C(x,t)=\frac{5000}{60\sqrt{4\pi(150{,}000)t}}e^{\frac{-(x-500-2400t)^2}{4(150{,}000)t}} \tag{4.3.4}$$

Values for time and location are substituted into this formula to generate the solid lines of Figure 4.4 for 0.2 hr, 0.4 hr, and 0.6 hr. Finite element solution, using the time step 0.01 hr., marked as horizontal dash for 0.2 hr, 0.4 hr, and 0.6 hr. respectively uses 100m element length. Figure 4.4(a) gives the comparison of the solution using standard Galerkin scheme without numerical diffusion, and Figure 4.4(b) shows the solution with numerical diffusion given as

$$E_n = -\frac{U^2 \Delta t}{2} \tag{4.3.5}$$

Using the above equation, the total mixing coefficient employed for the solution of Figure 4.4(b) is 150,000+28,800=178,800 m^2/hr. Figure 4.4(c) shows the solution using Petrov-Galerkin scheme without considering numerical diffusion. The initial concentration can be given for these runs as

$$C(500) = \frac{m}{B\Delta x H} = \frac{5000}{60(100)1} = 0.833 mg / l \tag{4.3.6}$$

Comparing the series of curves in Figure 4.4, it can be seen that standard Galerkin method shows high accuracy only when the additional numerical dispersion is considered. Comparing Figures 4.4(b) and 4.4(c), the accuracy of Petrov-Galerkin method is shown not to be better than the standard Galerkin scheme with numerical dispersions especially at the peak values. However, as shown in Figure 4.4(a), without introducing any of numerical dispersion, Petrov-Galerkin results are better than those obtained from standard Galerkin method.

The discrepancy between analytical and numerical solutions is due to not only spatial but also time domain discretization. As discussed in Appendix E, in order to overcome the error due to time domain discretization, central difference scheme is known to be better than backward or forward difference methods. However, even using the simple forward difference method, the solution of the Petrov-Galerkin scheme is found to be very acceptable and reliable in engineering problems.

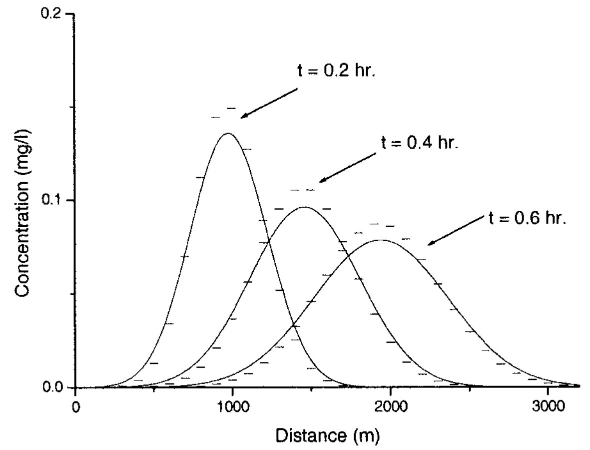

Figure 4.4(a) Standard Galerkin without numerical diffusion.

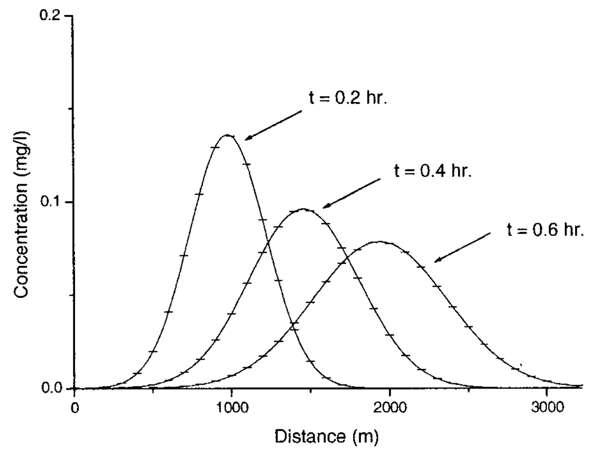

Figure 4.4(b) Standard Galerkin with numerical diffusion.

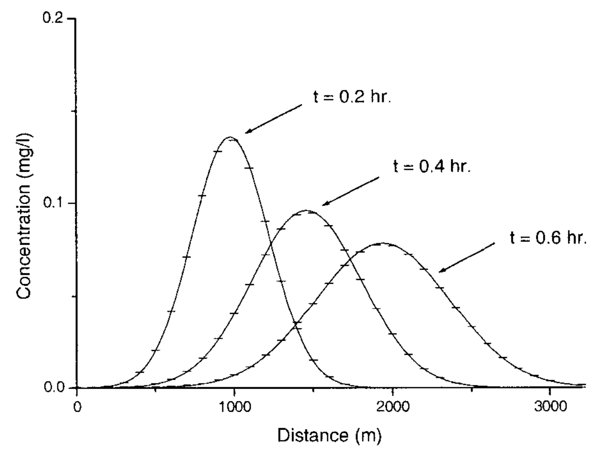

Figure 4.4(c) Petrov-Galerkin without numerical diffusion.

4.4. Model Application on the Mississippi River

By applying the newly developed sediment transport model to a natural river case, numerical simulation on the bed load and suspended load transport is conducted in this section. In this example, the model application is done for a reach in the Mississippi River located near St. Louis, Missouri and Hartford, Illinois (shown in Figure 4.5). The length of study reach is approximately 6517.8 m and the average channel width is about 457.2 m. Figure 4.6 shows finite element mesh provided by the mesh generation program. The mesh domain includes 3794 elements and 3980 nodal points. The boundary condition of the modeling case is when the flow discharge is 10,046.5 cms: The approach average velocity is 1.93 m/sec, shear velocity is given as 0.109 m/sec, and the average flow depth is approximately 12.5m.

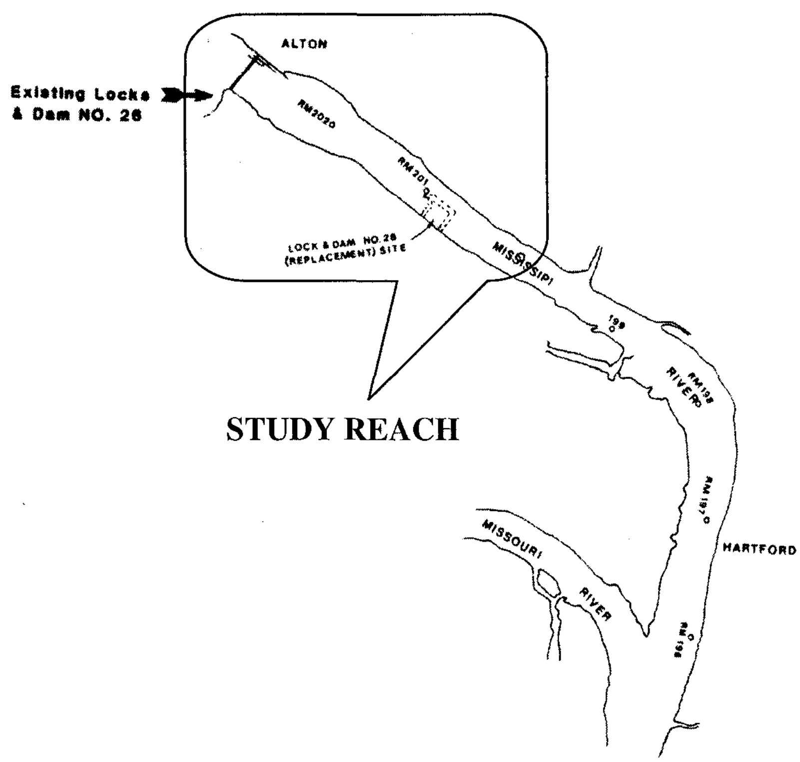

Figure 4.5 Location and plan view of the study reach.

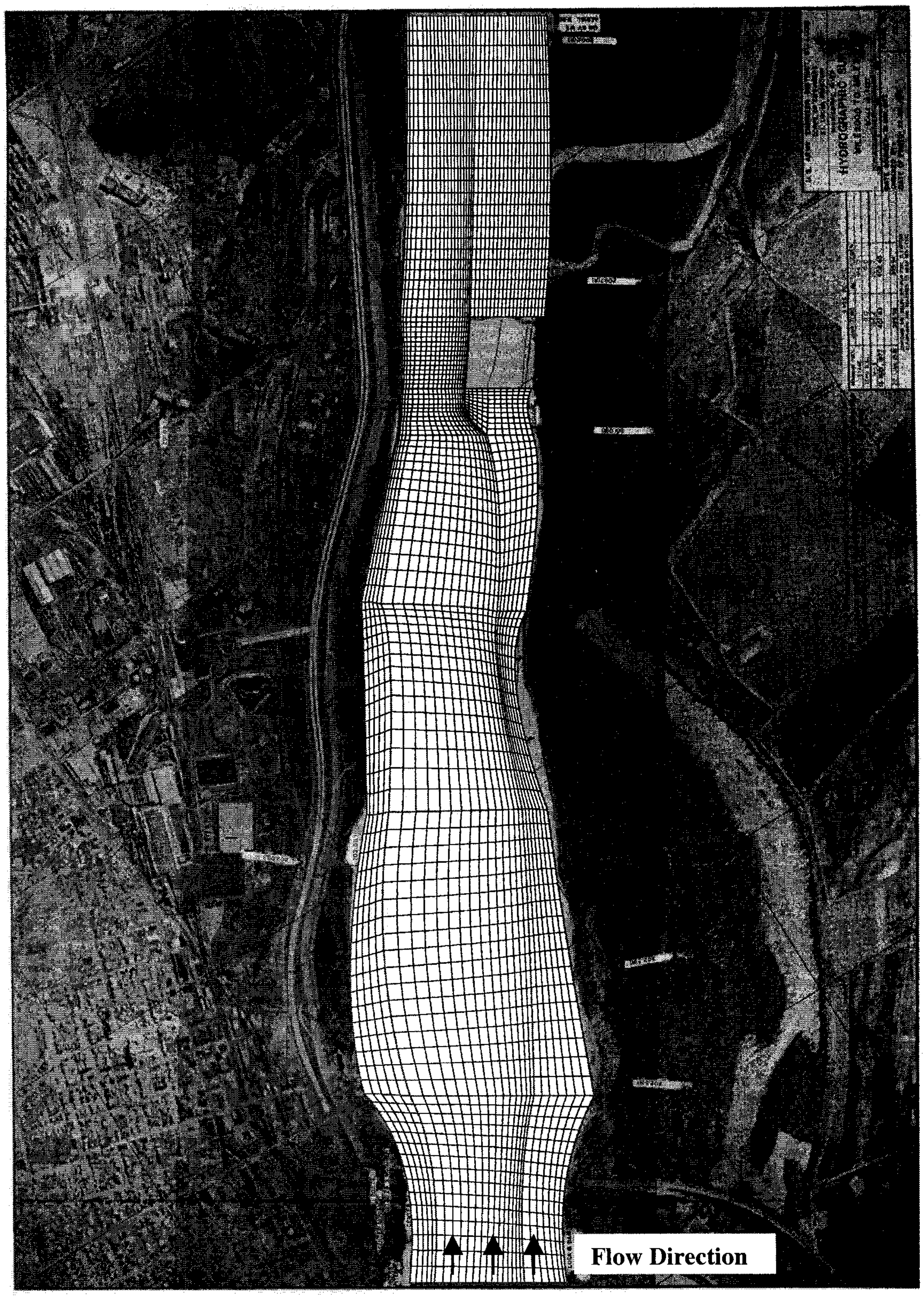

Figure 4.6 Mesh generation for the study reach in the Mississippi River.

4.4.1. Flow velocity distributions

Figure 4.7 shows the velocity distribution of the study reach. At the beginning portion of the channel inlet, the geometrical shape is similar to a sudden expansion channel so that the flow velocity profile across the channel width exhibits concave type of parabolic distribution. The flow velocity at both ends is greater than the flow velocity at center point. Similar shape of the velocity profile is measured in the experimental study of sudden expansion channels conducted by Loukrou (1979). However, as the flow propagates and approaches the contracted zone, the shape of velocity profile is gradually change into a convective type that is a typical fully developed velocity profile in open channel flows.

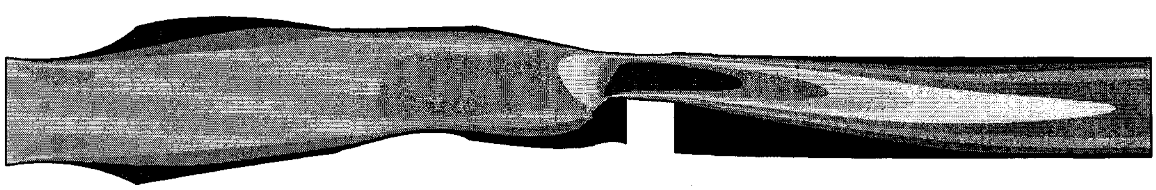

Figure 4.7 Flow velocity distributions in the study reach of the Mississippi River.

The coffer dam reduces the flow area by almost 50% of the average channel width. Even for this severe contraction, the present hydrodynamic model successfully solves the motions of flow. The maximum total velocity through the entire reach is computed as 5.398 m/sec; that is more than 2.5 times to the initial approach flow velocity. Other than the flow velocity components, the flow depth is also taken into account in the hydraulic application. In order to compute the water surface elevation, some modification was incorporated to this model. The following formulation is employed for the flow depth computation.

$$\begin{aligned} &\rho(\text{density}) \rightarrow h(\text{depth}) \\ &u_i(\text{velocity}) \rightarrow U_i(\text{mean velocity}) \\ &p(\text{pressure}) \rightarrow \tfrac{1}{2} g(h^2 - H^2) \end{aligned} \tag{4.4.1}$$

where, $H =$ averaged value of the flow depth

Since the water surface elevation is obtained from the summation of flow depth and channel bottom elevation, the channel bottom elevation is computed from the given bed slope which is measured as 0.0001. Using the above equation, the maximum difference of the water surface elevation in the contracted zone yields 0.18~0.213 m which is in good agreement with the measured range of 0.213~0.274 m.

4.4.2. Application of the bed load transport model

The contraction ratio of the study reach due to the coffer dam is approximately 50% and most of scour process occurs in the contracteds zone. The computational time step is chosen as 100 seconds and the results are plotted at 1 day (24 hour), 3 days (72 hour), and 10 days from the initial run. Since the present analysis is focused on channel contractions and the result is shown in Figure 4.8(a), (b), and (c) respectively pertain to contracted zone. The initial bed elevation is assumed to be 110 m (361 feet) and after 24 hour the maximum scour depth is computed as 5.13 ft as shown in Figure 4.8 (a); and after 3 days (72 hours) the maximum computed scour depth is 10.4 ft as shown in Figure 4.8 (b); and after 10 days of simulation, scour is computed to be 18.45 ft as shown in Figure 4.8 (c).

In this simulation, the van Rijn equation (4.3.2) is employed for bed load transport equation with an assumed porosity ratio of 0.6. As shown in this Figure 4.8, the maximum scour is taken place in the nose region of the structure where the velocity gradient is largest. Comparing figures 4.8(a), 4.8(b), and 4.8(c) it can be seen that the scour process gradually propagates toward downstream of the contracted zone until it approaches equilibrium condition. In order to take account the reduction of shear stress with the progression of scour process, the continuity equation was incorporated into shear stress computations by reducing velocities through deepening of flows.

Measured and computed bed elevation contours are shown in Figure 4.9 in order to facilitate evaluation of numerical results. These results show very close agreement. Scour at the entrance of the contracted each near the coffer dam is a fully three-dimensional process. The vertical velocity in depth direction exhibits an eddy zone in the vertical plane as well as in the horizontal plane cause a spiral flow. Basically, since the fundamental assumption of this model is solely dependent on two-dimensional configuration, fully three-dimensional process is not taken into account. However, by incorporating the continuity equation into the shear stress formulation in the algorithm, the scour depth development through time is realistically simulated. As a result, the numerical result shows good agreement with measured data for bed elevation distributions in the channel contraction.

The model is able to determine the foundation depth in the process of hydraulic structure design and compute the ultimate scour depth under equilibrium conditions. Additionally, the model provides valuable information in identifying zone of severe bed elevation changes through time under various flow conditions.

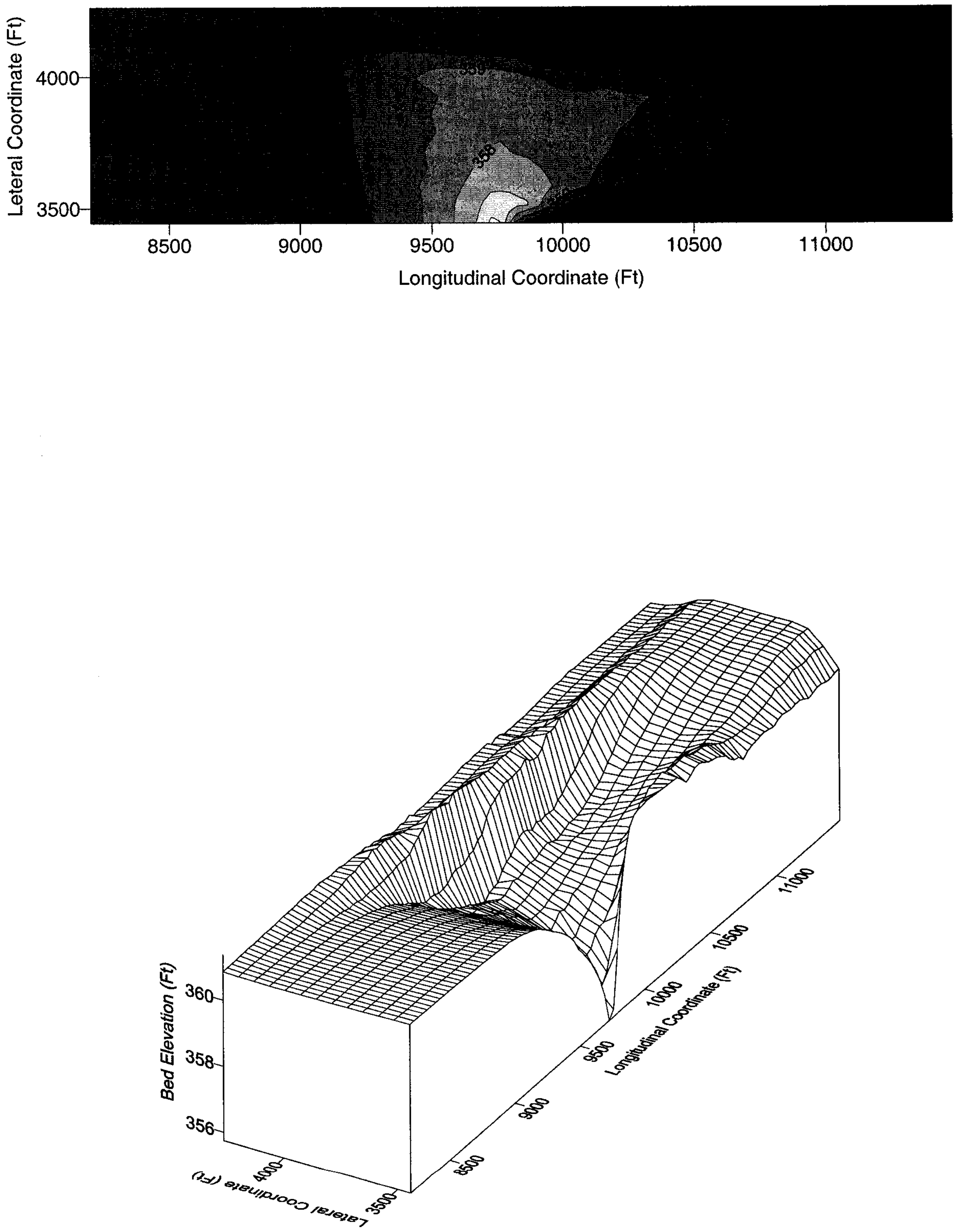

Figure 4.8(a) Bed elevation distributions in contracted reach after 1 day (24 hours).

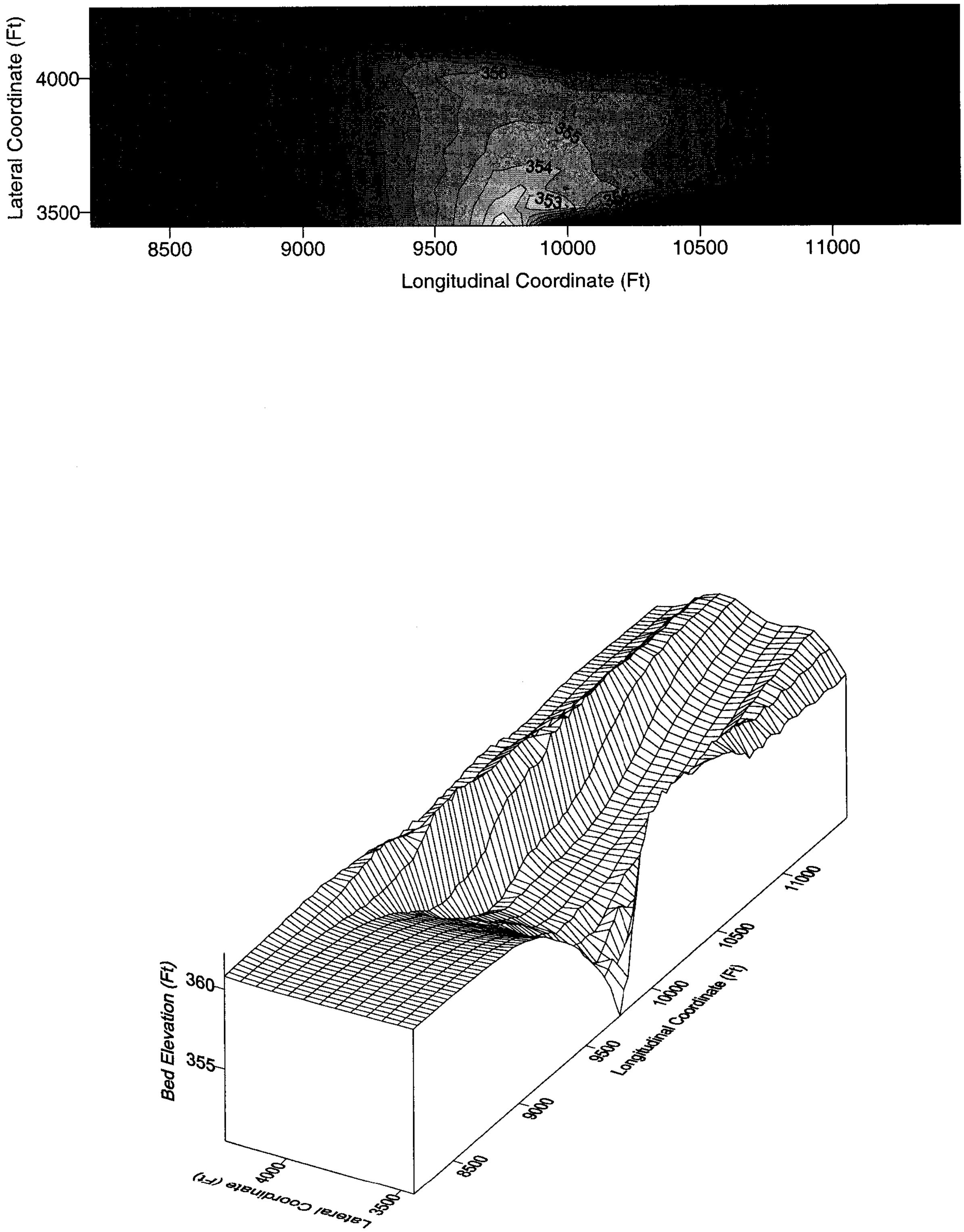

Figure 4.8(b) Bed elevation distributions in contracted reach after 3 days (72 hours).

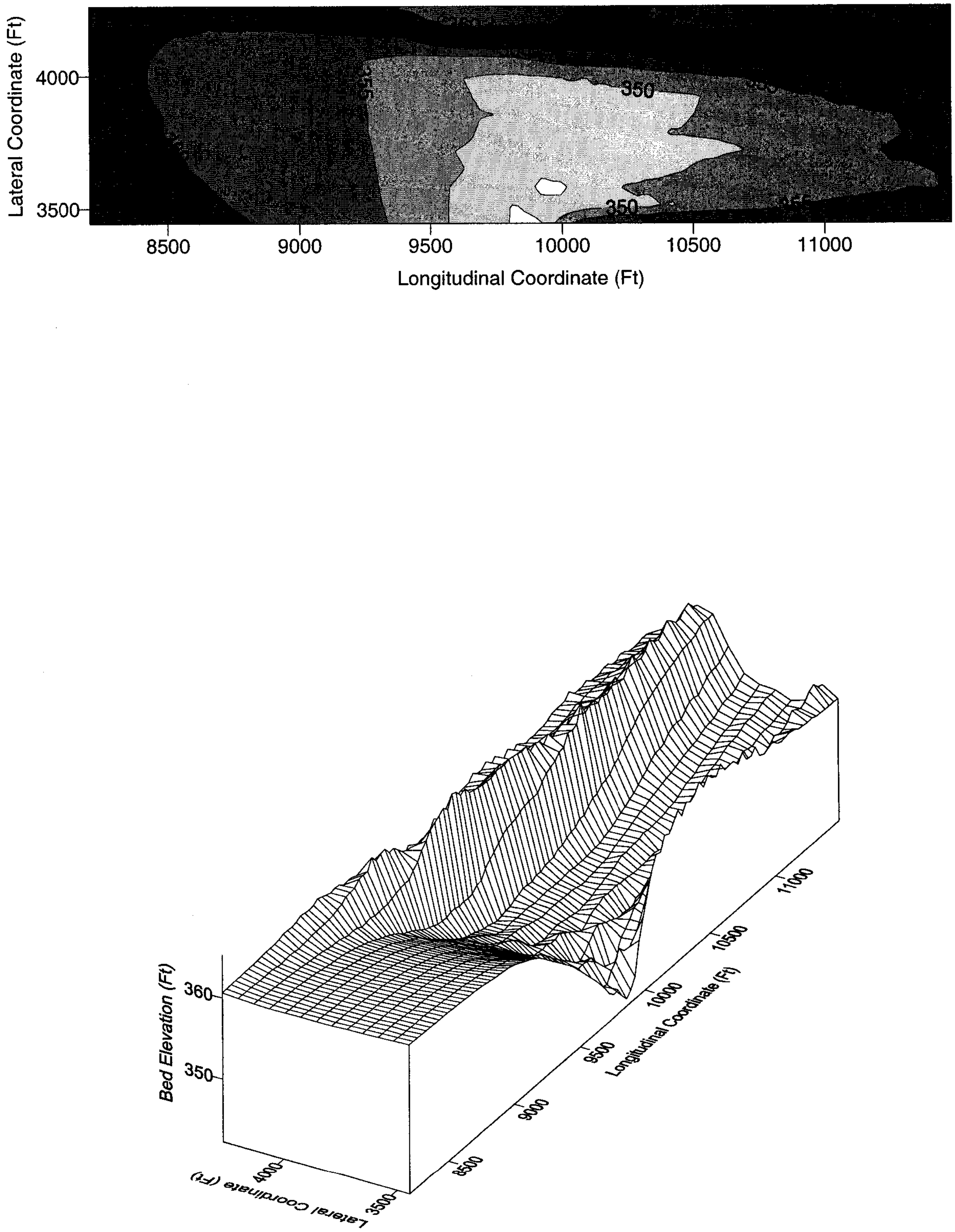

Figure 4.8(c) Bed elevation distributions in contracted reach after 10 days.

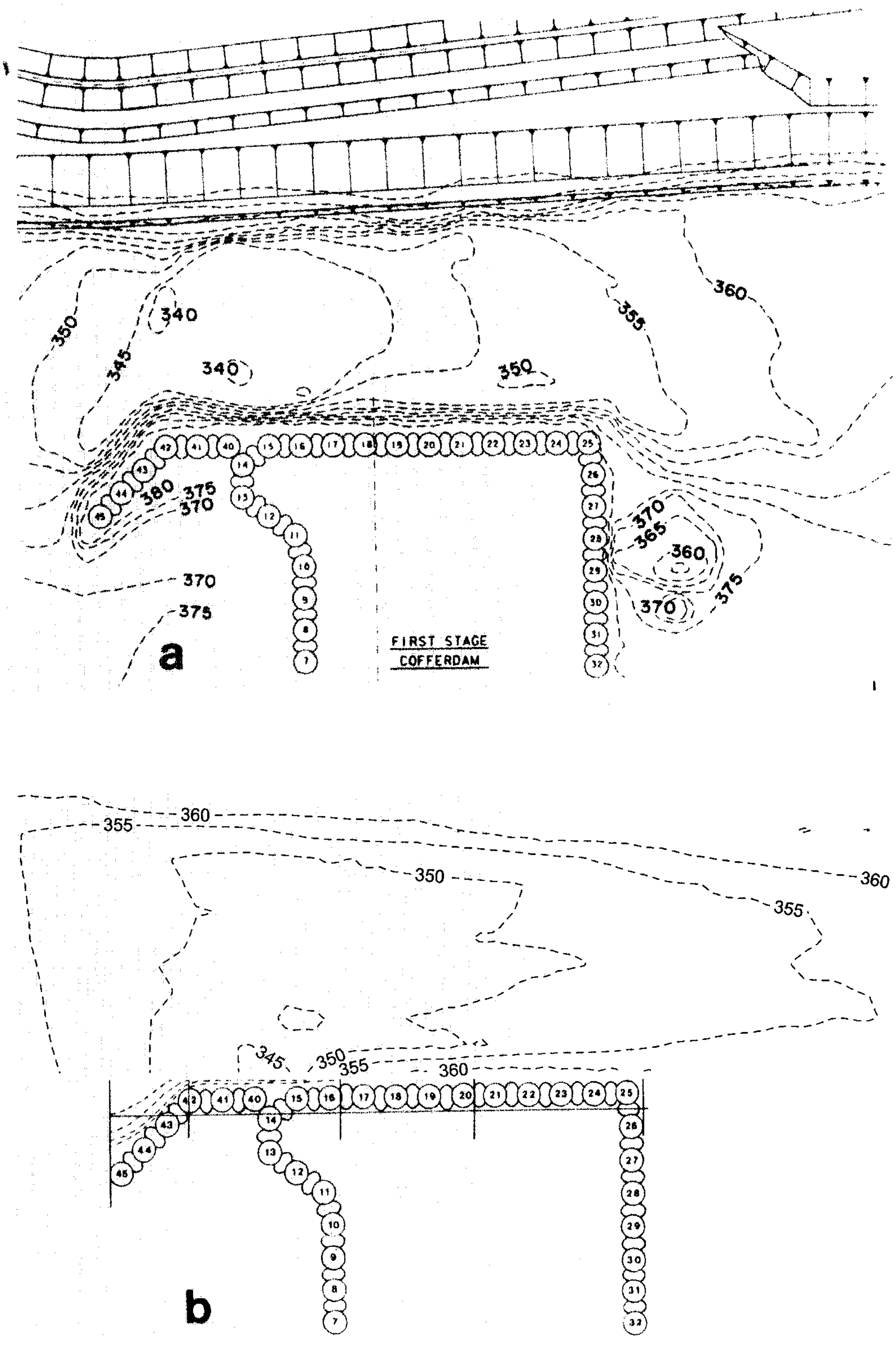

Figure 4.9 **Comparison between measured (a) and computed (b) bed elevation.**

4.4.3. Application of the suspended load transport model

The model simulation of the suspended transport is also conducted to investigate variations of the suspended load concentration in the study reach through time and space. The velocity components U and V from the governing equation is obtained according to the flow velocity distribution computations explained in section 4.4.1 of this chapter. Due to existence of the contracted reach, the flow velocity dramatically increases and the corresponding suspended load transport procedure very actively accelerates as the flow approaches the contracted region. In the model runs, the diffusion coefficients in the x, y directions are obtained by Equation (4.4.22) as 333.2 m^2/s and 1.42 m^2/s respectively.

The fundamental assumption of the numerical simulation is that the initial sediment concentration in the river remains at 70mg/l and the external source, for example such as dredging or accidental spill, introduces the 90mg/l concentration of suspended load from the channel inlet. Sediment is introduced to the channel continuously for 20 seconds and vanishes after this initial 20 seconds. This configuration can be easily implemented by expressing the external source as function of time variable using the mixed boundary condition explained in section 4.2.2. The concept of the mixed boundary condition allows the model to handle not only the continuous but also time variable suspended load inflow into the river system. For transient term computation, lumped matrix is employed for mass matrix diagonalization that provides easy matrix manipulation. The numerical simulation was very successful and stable in simulating the suspended load movement even in river system with a high contracted reach. However, the field measurement of the passage of suspended load wave is very difficult. In this study, full model verification using the field data could not be achieved due to the lack of measured data. Instead, model verification was accomplished using the analytical solution.

As mentioned before, this model gives the solution of convection and diffusion equation and is useful for wide range of application on the hydraulic problems other than suspended load transport such as contaminant transport and water quality problems. For an example of the proper modification to the water quality modeling, the source term of the governing equation can be replaced by the product of concentration and reaction rate. The model can also be used in the design of hydraulic structure to minimize the impacts of incoming suspended load. In addition, this model is useful for proper operation of the water intake facilities through the real time simulation to predict approximate concentration of spilled contaminants at a specific location where the water intake systems are installed.

The numerical results are briefly shown in Figure 4.10, and more detailed results are given in Appendix I. The time interval used in the simulation was 100 seconds. Following the shape of distributions of suspended load concentration, it is possible to predict a velocity profile across the channel width. For example, as shown in Appendix I, at 200, 300 seconds, from the sediment propagation, the velocity profile would be a concave type of parabolic distribution. As the cloud of introduced suspended load approaches to the Lock & Dam No. 26 site, the velocity profile gradually changed to be a convective type which is commonly encountered in open channels. The shape of the cloud changes completely and covers almost entire reach when it passes through the contracted reach as shown in the figure corresponding to 1500 seconds. The suspended sediment cloud is gradually diluted and vanished through time and space. As the suspended load propagates and passes through the study reach, due to the mixing process, the concentration distribution covers wide range while the concentration of suspended load decreases.

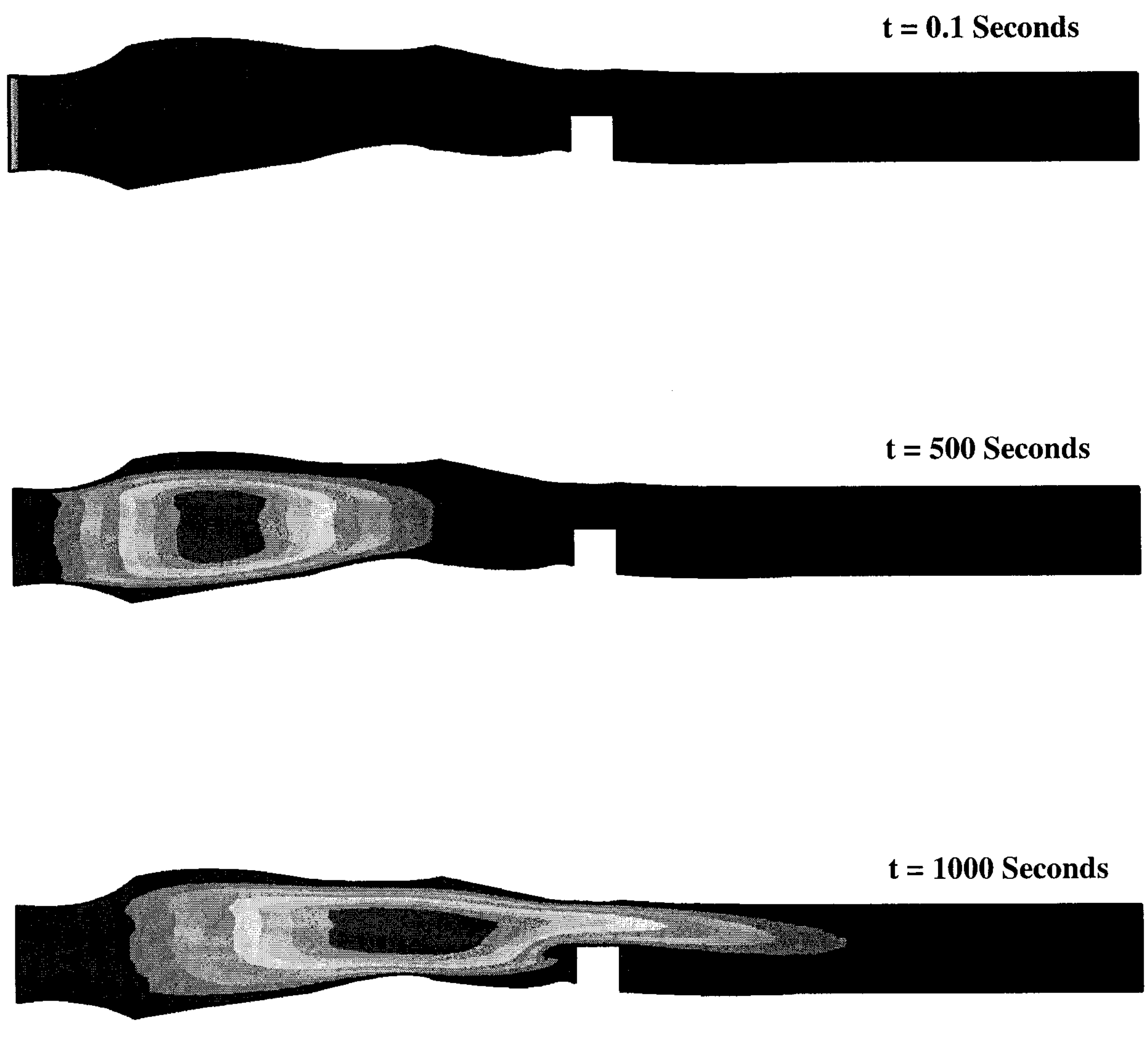

Figure 4.10 Numerical results of the suspended load transport model.

4.5. Summary

In this chapter, a sediment transport model was developed and the model application was conducted on the Mississippi River for Lock & Dam No. 26 (replacement) site. The contraction ratio in this reach is approximately 50 %. Approach flow velocities are increased about 2.5 times due to channel contraction. The flow velocity distribution is directly incorporated into the bottom shear stress distribution. By solving sediment continuity equation for bed load transport, it is possible to compute the bed elevation changes due to contractions.

Since the scour process is commonly encountered in contracted channel reaches, the analysis focuses on the contraction zones. Using finite element scheme, a numerical model is developed and applied for the analysis of scour depth and the trend of bed elevation distributions in this region. Lumped matrix concept was employed for the treatment of unsteady term to provide the diagonalization of the mass matrix in an efficient manner. The fundamental assumption of the modeling condition is that the flow remains in steady state, while the variation of channel bed elevation is unsteady. Through the comparison between measured data and numerical results, the model proved to be able to successfully predict the channel bed elevation changes.

Suspended load transport is also covered in this chapter by solving the convection and diffusion equation using the finite element method. Other than suspended load transport, this model has several other applications in open channel flow. Model verification was conducted through comparison with analytical solution. In model verification, Petrov-Galerkin proved to be a more efficient scheme than standard Galerkin scheme in the treatment of the convective terms by adding the balancing diffusion. In addition, by adapting mixed boundary concepts, the suspended load transport model can handle not only the case of continuous load but also the case of time-variable load. The results of numerical simulation are shown in two-dimensional horizontal plan view and allow predicting the suspended load concentration distributions and spatial propagation through time.

CHAPTER 5

5. SUMMARY, CONCLUSIONS, AND RECOMMENDATIONS

This study presents a finite element algorithm to solve the governing equations of flow motions as well as sediment transport equations with a series of numerical simulation for the flow, bed load transport and suspended load transport. The analysis focuses on modeling flows and sediment transport in channel contractions. The algorithm of the model is developed using finite element upwind scheme to provide numerical stability and verified with analytical solutions and the laboratory experiments. The upwind scheme is capable of reducing the numerical oscillation which occurs in convection dominated flow problems such as the flow in channel contractions.

Using hydrodynamic component of the model, the flow distribution analysis focuses on the velocity distribution of channel contractions due to skewed abutments. After a series of numerical simulations, an empirical equation is derived for the maximum velocity in terms of skewness angle and contraction ratio. Using the sediment transport model, investigate the scour problem as well as suspended load transport in channel contractions. The bed load transport model solves sediment continuity equation, and the suspended load transport model solves 2-dimensional convection and diffusion equation. After model verification, the practical usage of the model is demonstrated through the numerical simulation of the bed elevation change and passage of a suspended load wave. The model application was conducted on a stretch of the Mississippi River where a severe channel contraction occured due to the coffer dam construction.

5.1. Flow Distribution Analysis of Channel Contractions

A proposed 2-dimensional finite element model solves the Navier-Stokes equations to find flow velocity. In the algorithm of the numerical model, employing the penalty function, the global stiffness matrix incorporates pressure term in terms of velocity. The advantage of penalty function is that the continuity condition is automatically satisfied without solving the additional equation. In order to find the solution of this nonlinear equation, the Newton-Raphson method is employed in iterative manner until the solution converges. Adapting Petrov-Galerkin scheme, the balancing diffusion in weighting function provides numerical stability. The model is used for the analysis of flow distribution in the contracted reaches with the presence of skewed abutments. Following items are drawn as conclusions after a series of numerical simulation.

1. In the model formulation of the upwind scheme, adding the differentiated form of shape function into the weighting functions provides some mathematical diffusion to the convective term. Comparing with the solution of the standard Galerkin scheme, this balancing diffusion term seems to introduce slight dissipative characteristics.
2. Petrov-Galerkin scheme is more desirable for convection dominated fluid flow problems since the solution using the standard Galerkin scheme yields some oscillations unless very fine mesh domain is provided.
3. For single abutments, when the skewness angle is less than 90°, the maximum velocity corresponding to the angle change, shows a little variation between maximum velocities computed along the 3 different observation lines. At

skewness angles bigger than 90°, the variation found more pronounced compare to the cases with the skewness angles less than 90°.

4. The skewness effect on the velocity amplification is important for the cases of double abutment. Comparing with the single abutment cases, the corresponding difference between each of maximum velocity according to the angle variation increased up to 30 %.
5. For double abutment cases, statistical analysis was conducted with respect to each maximum velocity corresponding to the each skewness angle. The proposed Equation (3.9.3) from the regression analysis can be used to find approximate maximum velocities from provided known angles, roughness factors and the approach velocities.
6. At 90° case, for both cases of single and double abutments, peak velocities are obtained. The experimental result from Kwan (1984) shows good agreement with present study for the case of single abutments. The corresponding maximum velocity increases with the angle increase up to 90° then beyond 90°, the value of maximum total velocity decreases regardless of the angle increase
7. The variation due to the friction factor is not significant for both cases. Smooth boundary condition (smaller f values) results in the values of U / V_* increase, and corresponding maximum velocities slightly higher than rough boundary conditions (larger f values).

5.2. Sediment Transport Analysis of Contracted Reaches

Applying the newly developed numerical model, investigate sediment transport along with flow distribution for the Mississippi River. During the phase 1 construction of Lock & Dam No. 26 (replacement), the contraction ratio of the study reach is approximately 50%. Based on the flow velocity computed using the hydrodynamic model, the numerical analysis conducted on bed elevation changes as well as suspended load transport. In order to maintain the consistency with the hydrodynamic model, the model solves the transport equations of the bed load and the suspended load using the finite element upwind scheme. In addition, since the transport equation is basically unsteady, the algorithm covers the methodology solving the unsteady term as well.

1. For the treatment of the unsteady term, lumped matrix is obtained from row summation of the capacitance matrix. In this approach, matrix solver is not required, since lumped matrix diagonalizes the capacitance matrix of the unsteady term.
2. Row summation diagonalization scheme provides a very useful tool in matrix manipulation and the accuracy of the scheme proves to be acceptable through the comparison with analytical solution.
3. The bed load transport equation to compute the sediment transport capacity has the exponential expression in terms of the excess shear stress defined as the difference between shear stress and critical shear stress. Critical shear stress is the minimum shear stress that can mobilize particles on channel bottom and can be obtained from the Shields diagram or piecewise continuous mathematical approximating function.

4. The computed scour depth at previous time step should be taken into account for the equilibrium state. The model algorithm incorporates total flow depth into the shear stress computation for the configuration.
5. Suspended load transport modeling was also included in this study. The developed model was verified using an analytical solution. From the comparison between analytical and numerical solutions, it is necessary to add the numerical diffusion in order to compensate the truncation error when using the standard Galerkin scheme. By applying the Petov-Galerkin scheme the discrepancy is resolved due to this numerical diffusion.
6. Employing the mixed boundary concept in model algorithm allows expressing the source term as well as externally introduced suspended load concentration in terms of time duration. This formulation provides more vigorous and realistic environment for numerical simulation.
7. The algorithm for the suspended load transport introduced in this study can provide the frame work for various applications encountered in open channel hydraulics such as water quality and contaminant transport problems.

5.3. Recommendations

The model application of the Mississippi River successfully demonstrated the usage of the newly developed sediment transport model. However, a few limitations still left a room for further modification on certain assumptions, parameter selections, and methodologies. The follows itemized model improvements as well as applications that are of interest to scientists and engineers working in this field.

1. Regardless of the advantage related to the numerical stability, further investigation on dissipative nature of the Petrov-Galerkin scheme is recommended.
2. The algorithm and computation for different elements, such as 8-noded or 9-noded elements need to be considered.
3. For a more comprehensive modeling of the flow distribution, turbulent closure such as the k-ε model is desirable.
4. Further investigation is recommended for the wall boundary conditions. Especially for walls that do not fit into the orthogonal x-y coordinate system, the axis rotation for the manipulation of the boundary angle is recommended.
5. The configuration of mesh adaptation is recommended for the modeling of fully unsteady flows such as flood inundation or tidal flow problems.
6. Besides the row summation method which is employed for the present study, various other matrix diagonalization schemes need to be investigated and tested other than which is employed for the present study.
7. For scour problems, additional analysis on vertical plane using the x-z coordinate system needs to be considered for the bed elevation analysis due to the submerged structures.
8. Special attention must be taken for the selection of turbulent diffusion coefficient for the suspended load transport modeling in actual river studies.

Appendix A. References

1. Ahmad, M. (1953), "Experiments on design and behavior of spur dikes." *Proceedings*, Minnesota International Hydraulics Convention, Minneapolis, MN.

2. Ahmed, F. and Rajaratnam N. (2000), "Observations on flow around bridge abutment.", *Journal of Engineering Mechanics*, ASCE, Vol. 126 (1), pp. 51-59.

3. Awazu, S. (1967), "On scour around spur dike.", *Proceedings*, 12th International Association for Hydraulic Research, Vol. 3, Fort Collins, CO, Paper No. C12, pp. 97-104.

4. Barnes, H. H., Jr. (1967). "Roughness characteristics of natural channels." U.S. Geological Survey Water-supply paper 1894.

5. Berger, R. C. and Stockstill, R. L. (1995). "Finite-element model for high-velocity channels." *Journal of Hydraulic Engineering*, ASCE, Vol. 121 (10), pp. 710-716.

6. Biglari, B. and Sturm, T. W. (1998). "Numerical modeling of flow around bridge abutments in compound channel." *Journal of Hydraulic Engineering*, ASCE, Vol. 124 (2), pp. 156-164.

7. Brooks, A. N. and Hughes, T.J.R. (1982). "Streamline upwind-Galerkin formulations for convection dominated flows with particular emphasis on the incompressible Navier-Stokes equations." *Computer Methods in Applied Mechanics and Engineering*, Vol. 32, pp. 199-259.

8. Brørs, B. (1999). "Numerical modeling of flow and scour at pipelines." *Journal of Hydraulic Engineering*, ASCE, Vol. 125 (5), pp. 511-523.

9. Chapra, S. C. (1997). *Surface Water-Quality Modeling*. New York, McGraw-Hill.

10. Chaudhry, M. H. (1993). *Open channel flow*. New Jersey, Prenctice-Hall.

11. Chien, N. (1956). "The present status of research on sediment transport." *Transaction*, ASCE Vol. (121), pp. 833-868.

12. Chow, V. T. (1959). *Open-channel hydraulics.* New York, McGraw-Hill.

13. Committee on Hydromechanics (1963). "Friction factors in open channel." *Journal of Hydraulics Division*, ASCE, Vol. 89 (2), pp. 97-143.

14. Cooley, R. L. and Moins, S. A. (1976). "Finite element solution of Saint-Venant equations." *Journal of Hydraulics Division*, ASCE, Vol. 102 (6), pp. 759-775.

15. Dendy, J. E. (1974). "Two-methods of Galerkin-type achieving optimal optimum L^2 rates of convergence for first-order hyperbolics." *SIAM Journal of Numerical analysis*, Vol. 11(3), pp. 637-653.

16. DuBoys, M. P. (1879). "Le Rhone et les rivieres a lit affoillable." *Annales de ponts et chausses*, Sec. 5, Vol. 18, pp. 141-195.

17. Durst F. and Rastogi A. K. (1979). "Theoretical and experimental investigations of turbulence flows with separation." *Turbulent Shear flows 1*, Springer-Velarg, pp. 208-219.

18. Einstein, H. A. (1942). "Formula for the transportation of bed-load." *Transactions of the ASCE*, Vol. 107.

19. Elder, J. W. (1959). "The dispersion of marked fluid in turbulent shear flow." *Journal of Fluid Mechanics*, Vol. 5 (4), pp. 544-560.

20. Exner, F. M. (1925). "Uber die wechsrlwirkung zwischen wasser und geshiebe in flussen." *Sitzenberichte der akademie der wissenschaften, wien*, Heft 3-4.

21. Finnie, J. I., and Jeppson R. W. (1991). "Solving turbulent flows using finite element." *Journal of Hydraulic Engineering*, ASCE, Vol. 117 (11), pp. 1513-1530.

22. Fisher, H. B. et al. (1979). *Mixing in inland and coastal waters* Academic Press, Orlando, Florida.

23. Garde, R. J., Subramanya, K., and Nambudripad, K. D. (1961). "Study of scour around spur-dikes." *Journal of Hydraulics Division*, ASCE, Vol. 87 (6), pp. 23-37.

24. Gill, M. A. (1972). "Erosion of sand beds around spur dikes." *Journal of Hydraulics Division*, ASCE, Vol. 98 (9), pp. 1587-1602.

25. Gresho, P. M. and Lee, R. L. (1981). "Don't suppress the wiggles-they're telling you something!" *Computers and Fluids*, Vol. (9), pp. 223-253.

26. Gray, W. G., and Lynch, D. R. (1979). "On the control of noise in finite element tidal computations: A Semi-implicit approach." *Computers and Fluids*, Vol. 7 pp. 47-67.

27. Heinrich, J.C., Huyakorn, P.S., Zienkiwiewicz, O.C., and Mitchell, A.R., (1977). "An upwind finite element scheme for two dimensional convective transport equation." *International Journal for Numerical Methods in Engineering*, Vol. (11), pp. 627-643.

28. Heinrich, J.C. and Pepper, D. W. (1999). *Intermediate Finite Element Method*, Philadelphia, TAYLOR & FRANCIS.

29. Heinrich, J. C. and Yu, C. C. (1988). "Finite element simulation of buoyancy driven flows with emphasis on natural convection in a horizontal circular

cylinder." *Computer Methods in Applied Mechanics and Engineering*, Vol. 69, pp.1-27.

30. Henderson, F. M. (1966). *Open channel flow*. New York, Macmillan.
31. Heubner K. H. and Thornton E. A. (1982). *The finite element method for engineers*, (2nd Ed.) John Wiley & Sons, New York.
32. Hughes, T.J.R., Taylor, R. L., and Levy, J. -F. (1978). "High Reynolds number, steady, incompressible flows by finite element method." *Finite Element Method in Fluid.* Vol. (3), pp. 55-72.
33. Jia, Y. and Wang S. S. Y. (2001). *Technical report of CCHE2D.*
34. Julien, P. Y. (1995). *Erosion and Sedimentation.* New York, Cambridge University Press.
35. Kalinske, A. A. (1947). "Movement of sediment as bed-load in rivers." *Transactions of the AGU*, Vol. 28(4).
36. Katopodes, N. D. (1984). "A dissipative Galerkin scheme for open-channel flow." *Journal of Hydraulics Division*, ASCE, Vol. 110 (4), pp. 450-465.
37. Keuning, D. H. (1976). "Application of finite element method to open channel flow." *Journal of Hydraulics Division*, ASCE, Vol. 102 (4), pp. 459-468.
38. King, I. P. (1976). "Finite element models for unsteady flow routing through Irregular channels." *Finite Element in Water Resources*, Pentech Press, London, pp. 4.165-4.184.
39. Krishnappan B. G. (1985) "Comparison of MOBED and HEC-6 river flow models." *Canadian journal of Civil Engineering*, Vol. 12 (3), pp. 464-471.

40. Krishnappan B. G. and Lau, Y. L. (1986). "Turbulence modeling of flood plain flows." *Journal of Hydraulic Engineering*, ASCE, Vol. 112 (4), pp. 251-267.

41. Kuhnle, R. A., Alonso, C. V., and Shields, F. D. (1999). "Geometry of scour holes associated with 90° spur dikes." *Journal of Hydraulic Engineering*, ASCE, Vol. 125 (9), pp. 972-978.

42. Kwan, T. F. (1984). "Study of abutment scour." *University of Auckland School of Engineering Report No. 328,* Department of Civil Engineering, University of Auckland, Auckland, New Zealand.

43. Launder, B. E. and Spalding, D. B. (1972). *Mathematical Models of Turbulence* London, Academic Press.

44. Launder, B. E. and Spalding D. B. (1974). "The numerical computation of turbulent flows." *Computer methods in applied mechanics and engineering*, Vol. 3, pp. 269-289.

45. Laursen, E. M. (1958). "Scour at bridge crossings" *Iowa Highway Research Board Bulletin*, No. 8.

46. Laursen, E.M. (1963). "Analysis of relief bridge scour." *Journal of Hydraulics Division*, ASCE, Vol. 89(3), pp. 93-118.

47. Li, Y. S. and Zhan, J. M. (1993). "An efficient three-dimensional semi-implicit finite element scheme for simulation of free surface flows." *International Journal for Numerical Methods in fluids*, Vol. (16) pp.187-198.

48. Li, Y. S. and Zhan, J. M. (1998). "Three-dimensional finite element model for stratified coastal seas." *Journal of Hydraulic Engineering*, ASCE, Vol. 124 (7), pp. 699-703.

49. Lim, S. (1997). "Equilibrium clear-water scour around an abutment." *Journal of Hydraulic Engineering*, ASCE, Vol. 123 (3), pp. 237-243.

50. Liu, K. H., Chang, F. M., and Skinner, M. M. (1961). "Effect of bridge constrictions on scour and backwater." *CER60HKL22*, Colorado State University, Civil Eng., Fort Collins, CO.

51. Mayerele, R., Toro, F. M. and Wang, S. S. Y. (1996). "Verification of a three dimensional numerical model simulation of the flow in the vicinity of spur dikes." *Journal of Hydraulic Research*, Vol. (33), pp. 243-256.

52. McGuirk, J. J. and Rodi, W. (1978). "A depth-averaged mathematical model for the near field of side discharges into open-channel flow." *Journal of Fluid Mechanics*, Vol. 86 (4), pp. 726-781.

53. Melville, B. W. (1992). "Local scour at bridge abutments." *Journal of Hydraulic Engineering*, ASCE, Vol. 118 (4), pp. 615-630.

54. Melville, B. W. (1997). "Pier and abutment scour: Integrated approach." *Journal of Hydraulic Engineering*, ASCE, Vol. 123 (2), pp. 125-136.

55. Meyer-Peter, E., and R. Muller (1948). "Folrmula for bed-load transport." *Proceedings of international association for hydraulic research, 2nd meeting, Stockholm.*

56. Molinas, A., and Kheireldin (1998). "Shear stress around vertical wall abutment." *Journal of Hydraulic Engineering*, ASCE, Vol. 124 (8), pp. 822-830.

57. Molinas, A., and Hafez, Y. (2000). "Finite element surface model for flow around vertical wall abutment." *Journal of Fluids and Structure*, Vol. (14), pp. 711-733.

58. Morgan, K., Hughes, T. G., and Taylor, C. (1977). "Investigation of a mixing length and a two-equation turbulence model utilizing the finite element method" *Applied Mathematical Modeling*, Vol. (1), pp. 395-400.

59. Naot (1984). "Response of channel flow to roughness heterogeneity." *Journal of Hydraulic Engineering*, ASCE, Vol. 110, pp. 1568-1587.

60. Ouillon, S., and Dartus, D. (1997). "Three dimensional computation of flow around groyne." *Journal of Hydraulic Engineering*, ASCE, Vol. 123, pp. 962-970.

61. Pinder, G. F., and Gray, W. G. (1977). "Finite element simulation in surface and subsurface hydrology." New York, Academic Press.

62. Raithby, G. D., Hallet, W. L., Crawford, T. L., and Slawson, P. R. (1978). "Measurements and predictions of turbulent recirculating flow over a rectangular depression." *Boundary-layer Meteorology*, Vol. 15 (2), pp. 181-194.

63. Rajaratnam, N., and Nwachukwu, B. (1983a). "Flow near groyne-like structures." *Journal of Hydraulics Division*, ASCE, Vol. 109 (3), pp. 463-480.

64. Rajaratnam, N., and Nwachukwu, B. (1983b). "Erosion near groyne-like structures." *Journal of Hydraulic Research*, IAHR, Vol. 21 (4), pp. 463-480.

65. Rastogi and Rodi (1978). "Predictions of heat and mass transfer in open channels." *Journal of Hydraulics Division*, ASCE, Vol. 104 (3), pp. 397-420.

66. Rodi, W. (1993). *Turbulence models and their application in hydraulics.* A state of the art review, Delft, the Netherlands, IAHR.

67. Schlichting, H. (1968). *Boundary-layer Theory (6^{th} ed.)*, New York, McGraw-Hill

68. Shamber, D. R. and Larock, B. E. (1981). "Numerical analysis of flow in sedimentation basins." *Journal of Hydraulics Division*, ASCE, Vol. 109 (10), pp. 575-591.

69. Shamber, D. R. (1982). "Solution methods for turbulent flow via finite element." Applying research to hydraulic practice: Conference of the hydraulic division of the ASCE, *Proceedings*, pp. 55-64.

70. Simons, D. B. and Senturk (1992). *Sediment transport technology*, WRP, Fort. Collins, CO.

71. Smith, R. M. (1984a). "On the finite element calculation of turbulent flow using the k-ε model." *International journal for numerical methods in fluids*, Vol. 4, pp. 303-319.

72. Smith, R. M. (1984b). "A practical method of two-equation turbulence modeling using finite element." *International journal for numerical methods in fluids*, Vol. 4, pp. 321-336.

73. Tanguy, J. M., Dhatt, G., Frenette, M., and Monadier, P. (1989). "Modelisation of solid bed-load transport with the finite element method." *La Houille Blanche*, Paris, France, Vol. 3-4, pp. 263-267 (in French).

74. Taylor, C., Hughes, T. G., and Morgan K. (1978). "Finite element solution of one-equation model of turbulent flow." *Journal of computational physics*, Vol. (29), pp. 163-172.

75. Taylor, C., Thomas C. E., and Morgan K. (1978). "Modeling flow over a backward-facing step using the F. E. M. and the two-equation model of

turbulence." *International journal for numerical methods in fluids*, Vol. (29), pp. 89-102.

76. Thomas, C. E., Morgan, K., and Taylor, C. (1981). "A finite element analysis of flow over a backward facing step." *Computers and Fluids*, Vol. 9(3), pp. 265-278.
77. Tingsanchali, T., and Maheswaran, S. (1990). "2-D depth averaged flow computation near groyne." *Journal of Hydraulic Engineering*, 116 (1), pp. 71-86.
78. Tisdale, T. S., Scarlatos, P. D. and Hamrick, J. M. (1998). "Streamline upwind finite-element method for overland flow." *Journal of Hydraulic Engineering*, ASCE, Vol. 124 (4), pp. 350-357.
79. Thompson, E. G. (1999). *Class Note of CE665 Finite Element Method*, Fort Collins, CO.
80. van Rijn, L. C. (1984). *Mathematical modeling of Morphological Process in the case of Suspended Transport*. Delft, the Netherlands.
81. Yalin and Karahan (1979). "Inception of sediment transport." *Journal of Hydraulics Division*, ASCE, Vol. 105 (HY11), pp. 1433-1443.
82. Yang, C. H. (1996). *Sediment transport, theory and practice* New York, McGraw-Hill.
83. Zaghloul, N. A. (1974). *Analytical and experimental investigation of flow around a spur-dike*, Ph. D. Dissertation, Civil Engineering Department, University of Windsor, Windsor, Ontario, Canada.
84. Zaghloul, N. A. (1983). "Local Scour around Spur Dikes." *Journal of Hydrology*, Vol. (60), pp. 123-140.

85. Zienkiewicz, O. C., and Heinrich, J. C. (1979). "A unified treatment of steady-state shallow water and two-dimensional Navier-Stokes equations-finite element penalty function approach." *Computer Methods in Applied Mechanics and Engineering*, Vol. 17/18, pp. 673-698.

86. Zienkiewicz, O. C., and Taylor, R. L. (2000). *The Finite Element Method.* Vol. 1, Vol. 3 (5th edition), MA, Butterworth-Heinmann.

Appendix B. Evaluation of Element Matrices

The terms of the finite element equations are evaluated by carrying out the usual integration appearing in term, in general, the terms in the element equations will contain integrals of the form

$$\int_{A^{(e)}} f\left(\phi, \frac{\partial \phi}{\partial x}, \frac{\partial \phi}{\partial y}\right) dxdy \tag{B.1}$$

where, $A^{(e)}$ is the area of the element and ϕ is the unknown variable. For the integration, all of the variables ($\phi, \partial\phi/\partial x$, $\partial\phi/\partial y$, and $dxdy$) are expressed using the shape function which is evaluated terms of ξ and η. This can be done as follows.

$$\phi = \sum_{i=1}^{4} N_i \phi_i \,, \quad \frac{\partial \phi}{\partial x} = \sum_{i=1}^{4} \frac{\partial N_i}{\partial x} \phi_i \,, \quad \frac{\partial \phi}{\partial y} = \sum_{i=1}^{4} \frac{\partial N_i}{\partial y} \phi_i \tag{B.2}$$

where, N_i is shape function for 4 node linear element which can be given as

$$N_i(\xi,\eta) = \frac{1}{4}(1+\xi\xi_i)(1+\eta\eta_i), \qquad i = 1, 2, 3, 4 \tag{B.3}$$

Therefore, it is necessary to express $\partial N_i/\partial x$ and $\partial N_i/\partial y$ in terms of ξ and η also. Applying the chain rule of differentiation, the equation is

$$\frac{\partial N_i}{\partial \xi} = \frac{\partial N_i}{\partial x}\frac{\partial x}{\partial \xi} + \frac{\partial N_i}{\partial y}\frac{\partial y}{\partial \xi} \tag{B.4}$$

$$\frac{\partial N_i}{\partial \eta} = \frac{\partial N_i}{\partial x}\frac{\partial x}{\partial \eta} + \frac{\partial N_i}{\partial y}\frac{\partial y}{\partial \xi} \tag{B.5}$$

or in the matrix form,

$$\begin{Bmatrix} \dfrac{\partial N_i}{\partial \xi} \\ \dfrac{\partial N_i}{\partial \eta} \end{Bmatrix} = \begin{bmatrix} \dfrac{\partial x}{\partial \xi} & \dfrac{\partial y}{\partial \xi} \\ \dfrac{\partial x}{\partial \eta} & \dfrac{\partial x}{\partial \eta} \end{bmatrix} \begin{Bmatrix} \dfrac{\partial N_i}{\partial x} \\ \dfrac{\partial N_i}{\partial y} \end{Bmatrix} = [J] \begin{Bmatrix} \dfrac{\partial N_i}{\partial x} \\ \dfrac{\partial N_i}{\partial y} \end{Bmatrix} \tag{B.6}$$

where $[J]$ defines a Jacobian matrix,

$$[J] = \begin{bmatrix} \dfrac{\partial x}{\partial \xi} & \dfrac{\partial y}{\partial \xi} \\ \dfrac{\partial x}{\partial \eta} & \dfrac{\partial y}{\partial \eta} \end{bmatrix} \tag{B.7}$$

Evaluating an element Jacobian matrix using the coordinate transformation, for the four-node quadratic element is as follows.

$$[J(\xi,\eta)] = \begin{bmatrix} \sum_{i=1}^{4} \dfrac{\partial N_i}{\partial \xi}(\xi,\eta)x_i & \sum_{i=1}^{4} \dfrac{\partial N_i}{\partial \xi}(\xi,\eta)y_i \\ \sum_{i=1}^{4} \dfrac{\partial N_i}{\partial \xi}(\xi,\eta)x_i & \sum_{i=1}^{4} \dfrac{\partial N_i}{\partial \xi}(\xi,\eta)y_i \end{bmatrix} \tag{B.8}$$

To define the derivative of ϕ, invert form of Equation (B.6) is to obtained, and this involves finding the inverse of the Jacobian matrix as

$$\begin{Bmatrix} \dfrac{\partial N_i}{\partial x} \\ \dfrac{\partial N_i}{\partial y} \end{Bmatrix} = [J]^{-1} \begin{Bmatrix} \dfrac{\partial N_i}{\partial \xi} \\ \dfrac{\partial N_i}{\partial \eta} \end{Bmatrix}, \qquad i = 1, 2, 3, 4 \tag{B.9}$$

Now with this equation express for $\partial\phi/\partial x$ and $\partial\phi/\partial y$ can be found directly. From equation (B.2)

$$\begin{Bmatrix} \dfrac{\partial \phi}{\partial x} \\ \dfrac{\partial \phi}{\partial y} \end{Bmatrix} = \begin{bmatrix} \dfrac{\partial N_1}{\partial x} & \dfrac{\partial N_2}{\partial x} & \dfrac{\partial N_3}{\partial x} & \dfrac{\partial N_4}{\partial x} \\ \dfrac{\partial N_1}{\partial y} & \dfrac{\partial N_2}{\partial y} & \dfrac{\partial N_3}{\partial y} & \dfrac{\partial N_4}{\partial y} \end{bmatrix} \begin{Bmatrix} \phi_1 \\ \phi_2 \\ \phi_3 \\ \phi_4 \end{Bmatrix} \tag{B.10}$$

using Equation (B.9)

$$\begin{Bmatrix} \dfrac{\partial \phi}{\partial x} \\ \dfrac{\partial \phi}{\partial y} \end{Bmatrix} = [J]^{-1} \begin{bmatrix} \dfrac{\partial N_1}{\partial \xi} & \dfrac{\partial N_2}{\partial \xi} & \dfrac{\partial N_3}{\partial \xi} & \dfrac{\partial N_4}{\partial \xi} \\ \dfrac{\partial N_1}{\partial \eta} & \dfrac{\partial N_2}{\partial \eta} & \dfrac{\partial N_3}{\partial \eta} & \dfrac{\partial N_4}{\partial \eta} \end{bmatrix} \begin{Bmatrix} \phi_1 \\ \phi_2 \\ \phi_3 \\ \phi_4 \end{Bmatrix} \tag{B.11}$$

and the element of area $dxdy$ has to be expressed in terms of $d\xi d\eta$ to complete the evaluation of integral. Calculus shown as follows.

$$dxdy = |J| d\xi d\eta \tag{B.10}$$

where, $|J|$ is the determinant of $[J]$. The operations indicated in equations (B.10) and it depend on the existence of $[J]^{-1}$ for each element of assemblage, and the coordinate mapping described by equations (B.3) is unique only if $[J]^{-1}$ exists. If the sign of $|J|$ is not changing in the solution domain, the mapping is acceptable.

With these transformation, the integrals such as expression (B.1) reduces to the following form as

$$\int_{-1}^{1}\int_{-1}^{1} f'(\xi,\eta) d\xi d\eta \tag{B.11}$$

where, f' is the transformed function of f. Since the transformed integrand is not a simple function that permits closed form integration. For this reason, it is necessary to resort to numerical integration.

Appendix C. Capacitance Matrix Diagonalization

Row Summing: This method diagonalizes the matrix by replacing each diagonal with the sum of the terms on its row. Thus,

$$C(I,I) = \sum_{J=1}^{NNPE} \int_{Ve} N_I \mu N_J \, dV \tag{C.1}$$

$$C(I,J) = 0, \qquad I \neq J$$

Because the sum of the shape functions always add to be unity, the above gives

$$C(I,I) = \int_{Ve} N_I \mu \, dV \tag{C.2}$$

Hence summing rows results in lumping the distributed capacitance at the nodes in exactly the same manner that we have lumped distributed sources at the nodes. The following is a comparison of the consistent matrix with the lumped matrix for three elements. The numbers are the fraction of the total capacitance of the element given by

$$c = \int_{Ve} \mu \, dV \tag{C.3}$$

Element	Consistent Matrix	Lumped Matrix
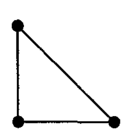	$\frac{c}{12}\begin{bmatrix} 2 & 1 & 1 \\ 1 & 2 & 1 \\ 1 & 1 & 2 \end{bmatrix}$	$\frac{c}{3}\begin{bmatrix} 1 & 0 & 0 \\ 0 & 1 & 0 \\ 0 & 0 & 1 \end{bmatrix}$
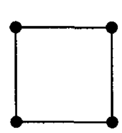	$\frac{c}{36}\begin{bmatrix} 4 & 2 & 1 & 2 \\ 2 & 4 & 2 & 1 \\ 1 & 2 & 4 & 2 \\ 2 & 1 & 2 & 4 \end{bmatrix}$	$\frac{c}{4}\begin{bmatrix} 1 & 0 & 0 & 0 \\ 0 & 1 & 0 & 0 \\ 0 & 0 & 1 & 0 \\ 0 & 0 & 0 & 1 \end{bmatrix}$

In each case above, the sum of the entries in each matrix equals unity, hence the matrices represent the total capacitance of the element. For the three node and four node elements, the lumped form are very acceptable; however, the lumped form for the six node element is not. The zero terms on the diagonal exclude the possibility of using this in an explicit formulation. Other higher order elements have equal problems, with either zeros or negative values appearing on the diagonal. For this reason, the following method is preferable when high order elements are used.

Scaled Diagonals: This method diagonalizes the matrix by retaining the relative values of each diagonal term but multiplying them by a scale factor to conserve the total capacitance of the matrix. Thus the relative values of the diagonal terms in the lumped matrix are kept the same as they are in the consistent matrix. Because none of the terms is zero or negative (true also for higher order elements) this method will always produce acceptable results.

For the three node and four node elements, the two methods of lumping give identical results. For the six node element, the following matrix is obtained:

$$\frac{c}{114}\begin{bmatrix} 6 & 0 & 0 & 0 & 0 & 0 \\ 0 & 32 & 0 & 0 & 0 & 0 \\ 0 & 0 & 6 & 0 & 0 & 0 \\ 0 & 0 & 0 & 32 & 0 & 0 \\ 0 & 0 & 0 & 0 & 6 & 0 \\ 0 & 0 & 0 & 0 & 0 & 32 \end{bmatrix} \tag{C.4}$$

where, again,

$$c = \int_{Ve} \mu dV \tag{C.5}$$

Special Quadrature: This method diagonalizes the matrix by taking the integration:

$$C(I,J) = \int_{Ve} N_I \mu N_J dV \tag{C.6}$$

using quadrature points located at the nodes. Therefore, the off-diagonal terms are always zero at the quadrature points; hence the resulting matrix has zeros on all off-diagonal terms.

Special Shape Functions: This method diagonalizes the matrix by using different shape functions to approximate $\dot{\phi}$ than are used to approximate ϕ. Because spatial derivatives of $\dot{\phi}$ do not appear in the integral for [C], it is not necessary that the approximation for this function be continuous. Therefore, discontinuous finite element approximations can be used instead of the continuous approximations used for ϕ. It is important to note, however, that in the integral

$$C(I,J) = \int_{Ve} N_I \mu N_J dV \tag{C.7}$$

only the second shape function can be replaced. The first shape function is used to approximate the weighting function and must be the same for all terms appearing in the weak form of the governing equation. Hence, we have

$$C(I,J) = \int_{Ve} N_I \mu \hat{N}_J dV \tag{C.8}$$

is the discontinuous shape function. Unfortunately, the diagonalization is often presented in the literature by replacing both shape functions. This may lead to an acceptable formulation, but it is not correct mathematics.

Appendix D. Treatment on Nodal Point Boundary Values

With higher order elements comes the added difficulty of calculating the nodal point values for the surface flux $q(s)$. The general expression for this flux is:

$$\begin{aligned}\int_S q(s)\delta\phi ds &= \int_S \{\delta\phi\}^T \lfloor N_s \rfloor^T q(s) ds \\ &= \{\delta\phi\}_s^T \{q_s\} \\ &= \lfloor \delta\phi \rfloor_s \{q_s\}\end{aligned} \tag{D.1}$$

where,

$$\begin{aligned}\{q\}_s &= \int_S \lfloor N_s \rfloor^T q(s) ds \\ &= \{\delta\phi\}_s^T \{q_s\} \\ &= \lfloor \delta\phi \rfloor_s \{q_s\}\end{aligned} \tag{D.2}$$

The surfaces over which this integration is taken are the sides of elements which coincide with the exterior boundary of our region. For 6-node elements, these sides will be curves in the x-y plane. In addition, the flux $q(s)$ may vary from point to point along these boundaries. Thus, the integration must be carried out numerically. We do so in the u-v plane using Gaussian quadrature.

In a manner similar to that used for the mapping of the isoparametric element in two dimensions, the curved boundary will be considered as having been mapped from a straight line segment along the u-axis.

The shape functions for the line segment on the u-axis are:

$$N_1 = -\frac{1}{2}(u)(1-u) \tag{D.3a}$$

$$N_1 = (1+u)(1-u) \tag{D.3b}$$

$$N_1 = +\frac{1}{2}(1+u)(u) \tag{D.3c}$$

The segment of the surface in the x-y plane is represented by the parametric equations

$$x(u) = \lfloor N_1 \quad N_2 \quad N_2 \rfloor \begin{Bmatrix} x_1 \\ x_2 \\ x_3 \end{Bmatrix} \tag{D.4a}$$

$$y(u) = \lfloor N_1 \quad N_2 \quad N_2 \rfloor \begin{Bmatrix} y_1 \\ y_2 \\ y_3 \end{Bmatrix} \tag{D.4b}$$

Analogous to the Jacobian matrix, we also have

$$\begin{aligned} dx &= \frac{dx}{du} du = \lfloor dN_s / du \rfloor \{x\}_s \, du \\ dx &= \frac{dy}{du} du = \lfloor dN_s / du \rfloor \{y\}_s \, du \end{aligned} \tag{D.5}$$

Because

$$ds^2 = dx^2 + dy^2 \tag{D.6}$$

and

$$ds = \left[\left(\frac{dx}{du} \right)^2 + \left(\frac{dy}{du} \right)^2 \right]^{\frac{1}{2}} du \tag{D.7}$$

or, simply

$$ds = \|J_s\| du \tag{D.8}$$

where,

$$\|J_s\| = \left[\left(\frac{dx}{du} \right)^2 + \left(\frac{dy}{du} \right)^2 \right]^{\frac{1}{2}} \tag{D.9}$$

Now, assume that $q(s)$ can be approximated by the shape functions such that

$$q(s) = \lfloor N_1 \quad N_2 \quad N_3 \rfloor \begin{Bmatrix} qs_1 \\ qs_2 \\ qs_3 \end{Bmatrix} \tag{D.10}$$

where, the *qs* values are the nodal point values of *q(s)*. Note these are not the same as the equivalent point sources. The relationship between the point sources and the nodal values of *q(s)* is

$$q = \int_{u=-1}^{u=+1} \{N_s\} \lfloor N_s \rfloor \{qs\} \|J_s\| du \tag{D.11}$$

where,

$$\{N_s\} = \lfloor N_s \rfloor^T \tag{D.12}$$

Integration by Gaussian quadrature requires the following steps at each point:

1. Evaluation of $\lfloor N_s \rfloor$ and $\lfloor dN_s/du \rfloor \{x\}_s$
2. Calculation of
$$\frac{dx}{du} = \lfloor dN_s/du \rfloor \{x\}_s$$
$$\frac{dy}{du} = \lfloor dN_s/du \rfloor \{y\}_s$$
3. Calculation of $\|J_s\|$
4. Evaluation of $q(s_i) = \lfloor N_s(u_i) \rfloor \{qs\}$
5. Final summation for quadrature
$$\{q\}_s = \{q\}_s + WT * \{N_s\} q(s_i) \|J_s\|$$

Appendix E. Stability Analysis

When the lumped capacitance is used for the solution of a transient problem, the algorithm can become unstable. In order to understand this, consider the following one-dimensional problem

$$R\frac{\partial^2\phi}{\partial x^2} - B\frac{\partial \phi}{\partial x} = \mu\frac{\partial \phi}{\partial t} \tag{E.1}$$

The weak form and finite element approximation creates the following element matrices.

$$\begin{bmatrix} -\frac{R}{\Delta x}+\frac{B}{2} & \frac{R}{\Delta x}-\frac{B}{2} \\ \frac{R}{\Delta x}+\frac{B}{2} & -\frac{R}{\Delta x}-\frac{B}{2} \end{bmatrix} \qquad \begin{bmatrix} \frac{\mu\Delta x}{3} & \frac{\mu\Delta x}{6} \\ \frac{\mu\Delta x}{6} & \frac{\mu\Delta x}{3} \end{bmatrix} \tag{E.2}$$

where, Δx is the element length.

The capacitance matrix on the right, when lumped, becomes

$$\begin{bmatrix} \frac{\mu\Delta x}{2} & 0 \\ 0 & \frac{\mu\Delta x}{2} \end{bmatrix} \tag{E.3}$$

For example, if we have a four element mesh of equal length and constant

$$\begin{bmatrix} -\frac{R}{\Delta x^2}+\frac{B}{2\Delta x} & \frac{R}{\Delta x^2}-\frac{B}{2\Delta x} & 0 & 0 & 0 \\ \frac{R}{\Delta x^2}+\frac{B}{2\Delta x} & -\frac{2R}{\Delta x^2} & \frac{R}{\Delta x^2}-\frac{B}{2\Delta x} & 0 & 0 \\ 0 & \frac{R}{\Delta x^2}+\frac{B}{2\Delta x} & -\frac{2R}{\Delta x^2} & \frac{R}{\Delta x^2}-\frac{B}{2\Delta x} & 0 \\ 0 & 0 & \frac{R}{\Delta x^2}+\frac{B}{2\Delta x} & -\frac{2R}{\Delta x^2} & \frac{R}{\Delta x^2}-\frac{B}{2\Delta x} \\ 0 & 0 & 0 & \frac{R}{\Delta x^2}+\frac{B}{2\Delta x} & -\frac{R}{\Delta x^2}-\frac{B}{2\Delta x} \end{bmatrix} \begin{Bmatrix} \Phi_1 \\ \Phi_2 \\ \Phi_3 \\ \Phi_4 \\ \Phi_5 \end{Bmatrix} = \begin{Bmatrix} \frac{1}{2}\dot{\Phi}_1 \\ \dot{\Phi}_2 \\ \dot{\Phi}_3 \\ \dot{\Phi}_4 \\ \frac{1}{2}\dot{\Phi}_5 \end{Bmatrix} \tag{E.4}$$

For any interior node i, the following equation can be obtained

$$\begin{bmatrix} \frac{R\Delta t}{\Delta x^2}+\frac{B\Delta t}{2\Delta x} & -\frac{2R\Delta t}{\Delta x^2} & \frac{R\Delta t}{\Delta x^2}-\frac{B\Delta t}{2\Delta x} \end{bmatrix} \begin{Bmatrix} \Phi_{i-1} \\ \Phi_i \\ \Phi_{i+1} \end{Bmatrix} = \dot{\Phi}_i \Delta t = \Phi_i(t+\Delta t) - \Phi_i(t) \tag{E.5}$$

Because the left hand side of the equation is evaluated at time *t*, $\Phi_i(t)$ on the right can be moved to the left side to obtain

$$\begin{bmatrix} \frac{R\Delta t}{\Delta x^2}+\frac{B\Delta t}{2\Delta x} & 1-\frac{2R\Delta t}{\Delta x^2} & \frac{R\Delta t}{\Delta x^2}-\frac{B\Delta t}{2\Delta x} \end{bmatrix} \begin{Bmatrix} \Phi_{i-1} \\ \Phi_i \\ \Phi_{i+1} \end{Bmatrix} = \Phi_i(t+\Delta t) \tag{E.6}$$

The cause of instability can now be illustrated by assuming that at time $t = 0$, in such a condition that all node have a Φ value of zero except node *i*, which has a value of ε, then the next increment of time, the above equation gives us the following values

Time	Φ_{i-2}	Φ_{i-1}	Φ_i	Φ_{i+1}	Φ_{i+2}
0	0	0	ε	0	0
Δt	0	$\varepsilon(r + B\Delta t/2\Delta x)$	$\varepsilon(1-2r)$	$\varepsilon(r - B\Delta t/2\Delta x)$	0

where, $r = \frac{R\Delta t}{\Delta x^2}$

It is clear from the first step, that if $r > 1/2$, the sign of Φ will change, hence creating an oscillation in the results. However, if $r < 1$, then $(1-2r)$ is less than unity and the magnitude of Φ will have decreased even though its sign will have changed. It is expected continued integration to create oscillation of decreasing magnitude. Because the governing equation requires that such perturbations be dissipated and that the solution eventually return to the steady-state condition, the algorithm will approach the correct answer but with unwanted oscillations. On the other hand, note that if $r > 1$, the perturbation will not only change sign, it will increase in magnitude. Finally, note that if

$r < 1/2$, then the Φ will remain same sign but decrease in magnitude which the preferred behavior. The conclusion is

$\Delta t < (\Delta x)^2/2R$: Stable with no oscillations

$\Delta t > (\Delta x)^2/2R$: Stable, but oscillations may happen

$\Delta t < (\Delta x)^2/R$: Unstable, oscillation with increasing magnitude may happen

In a two dimensional finite element mesh, the above conditions can be used as a guide for selecting Δt. The value to be used for the parameters R, B, and Δx should be taken as the worst case at any point in the mesh. Here, Δx can be taken as the diameter of circle circumscribing the element at the point being considered.

Appendix F. Numerical Schemes for Unsteady Term

Forward difference method

After the convection and diffusion terms are assembled into the global matrix. Assuming the value of ϕ is given at all nodes at time t, it is possible to solve time derivative for $\{\dot{\phi}\}_t$ at time t. Then, the matrix form will be as follows.

$$[C]\{\dot{\phi}\}_t = \{Q\}_t - [K]\{\phi\}_t \tag{F.1}$$

Once $\{\dot{\phi}\}_t$ is known, to obtain ϕ at a later time, it is integrated with respect to time. Applying the simple Eulerian integration, following equation is obtained.

$$\{\phi\}_{t+\Delta t} = \{\phi\}_t + \{\dot{\phi}\}_t \Delta t \tag{F.2}$$

Solving above equation with respect to $\{\dot{\phi}\}$

$$\{\dot{\phi}\}_t = \frac{1}{\Delta t}\left[\{\phi\}_{t+\Delta t} - \{\phi\}_t\right] \tag{F.3}$$

and substituting this into Equation (F.1) to obtain

$$[C]\frac{1}{\Delta t}\left[\{\phi\}_{t+\Delta t} - \{\phi\}_t\right] = \{Q\}_t - [K]\{\phi\}_t \tag{F.4}$$

Finally solving Equation (F.4) with respect to $\{\phi\}_{t+\Delta t}$,

$$\frac{1}{\Delta t}[C]\{\phi\}_{t+\Delta t} = \{Q\}_t + \left[\frac{1}{\Delta t}[C] - [K]\right]\{\phi\}_t \tag{F.5}$$

Equation (F.5) is simply the forward difference approximation of $\{\dot{\phi}\}$ at time t. This is straight forward and simple, but as Δt increase, it becomes unstable in value.

Backward Difference

In the forward difference method, it easily allows computing values of $\{\phi\}$ at time $t + \Delta t$ without any known boundary conditions at that time. Even except the problem of instability, this latter characteristic seems to place some doubt on its desirability. Although taking every smaller time step, any error due to selecting the time step can be resolved. However, it would be better if any other available solution which does not require very small time step and thus not require as many time steps to complete a given simulation condition.

The backward difference scheme requires to begin by writing the finite element Equation (F.1) at time $t+\Delta t$ rather than at time t. That is,

$$[C]\{\dot{\phi}\}_{t+\Delta t} = \{Q\}_{t+\Delta t} - [K]\{\phi\}_{t+\Delta t} \tag{F.6}$$

and considering the finite element expression for $\{\dot{\phi}\}$ as a backward difference at time $t+\Delta t$ rather than a forward difference at time t. Therefore,

$$\{\dot{\phi}\}_{t+\Delta t} = \frac{1}{\Delta t}\{\{\phi\}_{t+\Delta t} - \{\phi\}_t\} \tag{F.7}$$

After substituting into Equation (F.6) to yield

$$\frac{1}{\Delta t}[C]\{\{\phi\}_{t+\Delta t} - \{\phi\}_t\} = \{Q\}_{t+\Delta t} - [K]\{\phi\}_{t+\Delta t} \tag{F.8}$$

which can be rewritten as

$$\left[\frac{1}{\Delta t}[C] + [K]\right]\{\phi\}_{t+\Delta t} = \{Q\}_{t+\Delta t} + \frac{1}{\Delta t}[C]\{\phi\}_t \tag{F.9}$$

All parameters used in the calculations of $[K]$ and $[C]$ are evaluated at time $t+\Delta T$.

Now, a set of simultaneous equations is derived for $\{\phi\}_{t+\Delta t}$ based on values of $\{\dot{\phi}\}$ which take into account of the boundary conditions at $t+\Delta T$. Note that this formulation is unconditionally stable.

Central Difference Scheme

The forward difference formulation is

$$\frac{1}{\Delta t}[C]\{\phi\}_{t+\Delta t} = \{Q\}_t + \left[\frac{1}{\Delta t}[C] - [K]\right]\{\phi\}_t \tag{F.10}$$

and the backward difference formulation is

$$\left[\frac{1}{\Delta t}[C] + [K]\right]\{\phi\}_{t+\Delta t} = \{Q\}_{t+\Delta t} + \frac{1}{\Delta t}[C]\{\phi\}_t \tag{F.11}$$

For both formulations the following expression is used

$$\frac{1}{\Delta t}\{\{\phi\}_{t+\Delta t} - \{\phi\}_t\} \tag{F.12}$$

For the approximation of the term $\{\dot{\phi}\}$, either at the beginning of the time step or at the end of the time step, at the center of the time step, this expression more accurately approximates $\{\dot{\phi}\}$. Therefore, Equation (F.1) can be written as

$$[C]\{\dot{\phi}\}_{t+\Delta t/2} = \{Q\}_{t+\Delta t/2} - [K]\{\dot{\phi}\}_{t+\Delta t/2} \tag{F.13}$$

For the left hand side of above Equation, a central difference scheme is applied, and for the right hand side, use the averaged value of ϕ which is given as

$$\{\phi\}_{t+\Delta t/2} = \frac{1}{2}\{\{\phi\} + \{\phi\}_{t+\Delta t}\} \tag{F.14}$$

Therefore, Equation (F.13) becomes

$$\frac{1}{\Delta t}[C]\{\{\phi\}_{t+\Delta t} - \{\phi\}_t\} = \{Q\}_{t+\Delta t/2} - \frac{1}{2}[K]\{\{\phi\}_{t+\Delta t} + \{\phi\}_t\} \tag{F.15}$$

or

$$\left[\frac{1}{\Delta t}[C] + \frac{1}{2}[K]\right]\{\phi\}_{t+\Delta t} = \{Q\}_{t+\Delta t/2} + \left[\frac{1}{\Delta t}[C] - \frac{1}{2}[K]\right]\{\phi\}_t \tag{F.16}$$

From the above equations, all parameters used in the calculations of $[K]$ and $[C]$ are evaluated at time $t+\Delta t/2$. This is referred as the central difference approximation and it is correspondent to the Crank-Nicolson scheme in the finite difference method. Although many other formulations are available, the central difference formulation is the most popular. This scheme is also unconditionally stable and has higher order of accuracy than either forward difference or backward difference scheme.

Appendix G. Determination of the Characteristic Length

Since the definition of $\bar{h}$ in Petrov-Galerkin is somewhat arbitrary, it depends on the resultant velocity as well as the size of element. Heinrich and Yu (1988) proposed following equation for defining the element length $\bar{h}$ in the direction of the flow.

$$\bar{h} = \frac{1}{|\mathbf{U}|}\left(|h_1| + |h_2|\right) \tag{G.1}$$

where,

$$\begin{aligned} h_1 &= \mathbf{a} \cdot \mathbf{U} \\ h_2 &= \mathbf{b} \cdot \mathbf{U} \end{aligned} \tag{G.2}$$

and **a** and **b** are the vectors which are given as follows

$$\begin{aligned} a_1 &= \frac{1}{2}(x_2 + x_3 - x_1 - x_4) \\ a_2 &= \frac{1}{2}(y_2 + y_3 - y_1 - y_4) \\ b_1 &= \frac{1}{2}(x_3 + x_4 - x_1 - x_2) \\ b_2 &= \frac{1}{2}(y_3 + y_4 - y_1 - y_2) \end{aligned} \tag{G.3}$$

Vectors **a** and **b** are the ones that join the midpoint of opposite sides in a quadrilateral element shown in Figure G.1. h_1 and h_2 are the projections of these vectors in the direction of the flow.

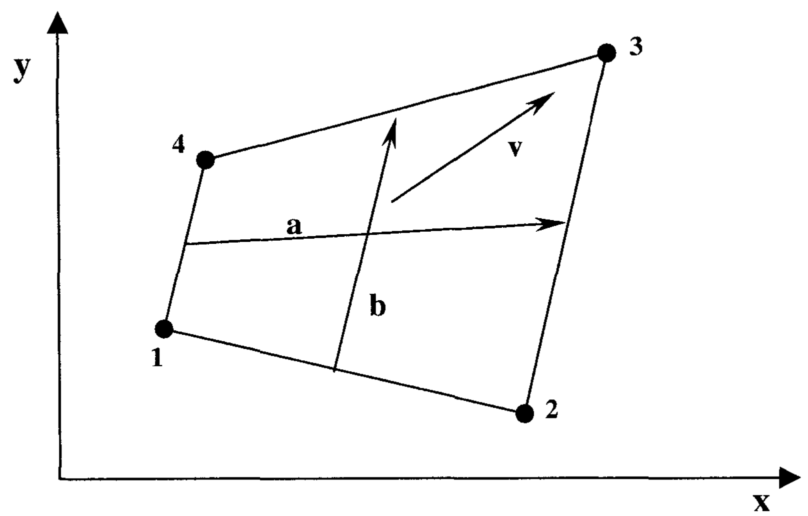

Figure G.1 General bilinear quadrilateral element (After Heinrich & Pepper, 1999).

Appendix H. Numerical Diffusion

For simplicity, describe the truncation error of the pure convection equation

$$\frac{\partial c}{\partial t} = -U\frac{\partial c}{\partial x} \tag{H.1}$$

A backward Taylor-series expansion can be written in space and truncated to yield

$$\frac{\partial c}{\partial x} \cong \frac{c_i^l - c_{i-1}^l}{\Delta x} + \frac{\Delta x}{2}\frac{\partial^2 c}{\partial x^2} \tag{H.2}$$

In same manner, a forward series can be written in time and truncated to give

$$\frac{\partial c}{\partial t} \cong \frac{c_i^{l+1} - c_i^l}{\Delta t} + \frac{\Delta t}{2}\frac{\partial^2 c}{\partial t^2} \tag{H.3}$$

Equations (H.2) and (H.3) can be combined with (H.1) to yield

$$\frac{\partial c}{\partial t} = -U\frac{\partial c}{\partial x} + U\frac{\Delta x}{2}\frac{\partial^2 c}{\partial x^2} - \frac{\Delta t}{2}\frac{\partial^2 c}{\partial t^2} \tag{H.4}$$

The second-order time derivative can be converted to a space derivative by differentiating Equation (H.1) with respect to time

$$\frac{\partial^2 c}{\partial t^2} = -U\frac{\partial^2 c}{\partial t \partial x} \tag{H.5}$$

Next differentiate Equation (H.1) with respect to space

$$\frac{\partial^2 c}{\partial x \partial t} = -U\frac{\partial^2 c}{\partial^2 x} \tag{H.6}$$

and substituted into Equation (H.4) to yield

$$\frac{\partial c}{\partial t} = \left(\frac{\Delta x}{2}U - \frac{U^2 \Delta t}{2}\right)\frac{\partial^2 c}{\partial x^2} - U\frac{\partial c}{\partial x} \tag{H.7}$$

Thus, the numerical diffusion is

$$E_n = \frac{\Delta x}{2} U - \frac{U^2 \Delta t}{2} \tag{H.8}$$

In general, the numerical diffusion can be represented as

$$E_n = U\Delta x\left[(\alpha - 0.5) - \frac{U\Delta t}{2\Delta x}\right] \tag{H.9}$$

Close inspection of this formula indicates that there are two independent effects on numerical dispersion that is spatial and temporal discretization effects

$$E_n = U\Delta x(\alpha - 0.5) - \frac{U^2 \Delta t}{2\Delta x} \tag{H.10}$$

In the backward difference case $(\alpha = 1)$, the time step that would yield zero numerical diffusion can be obtained by setting Equation (H.10) to zero and solving for

$$\Delta t = \frac{\Delta x}{U} \tag{H.11}$$

since finite element is equivalent to the central difference in space domain which yields no spatial diffusion $(\alpha = 0.5)$. For this case Equation (H.9) reduces to

$$E_n = -\frac{U^2 \Delta t}{2} \tag{H.12}$$

Thus, a negative numerical diffusion is created. In this case, an additional diffusion equivalent to the absolute value of the quantity calculate in Equation (H.12) would be added to the actual physical diffusion used in the model.

Appendix I. Results of the Suspended Load Transport in the Mississippi River

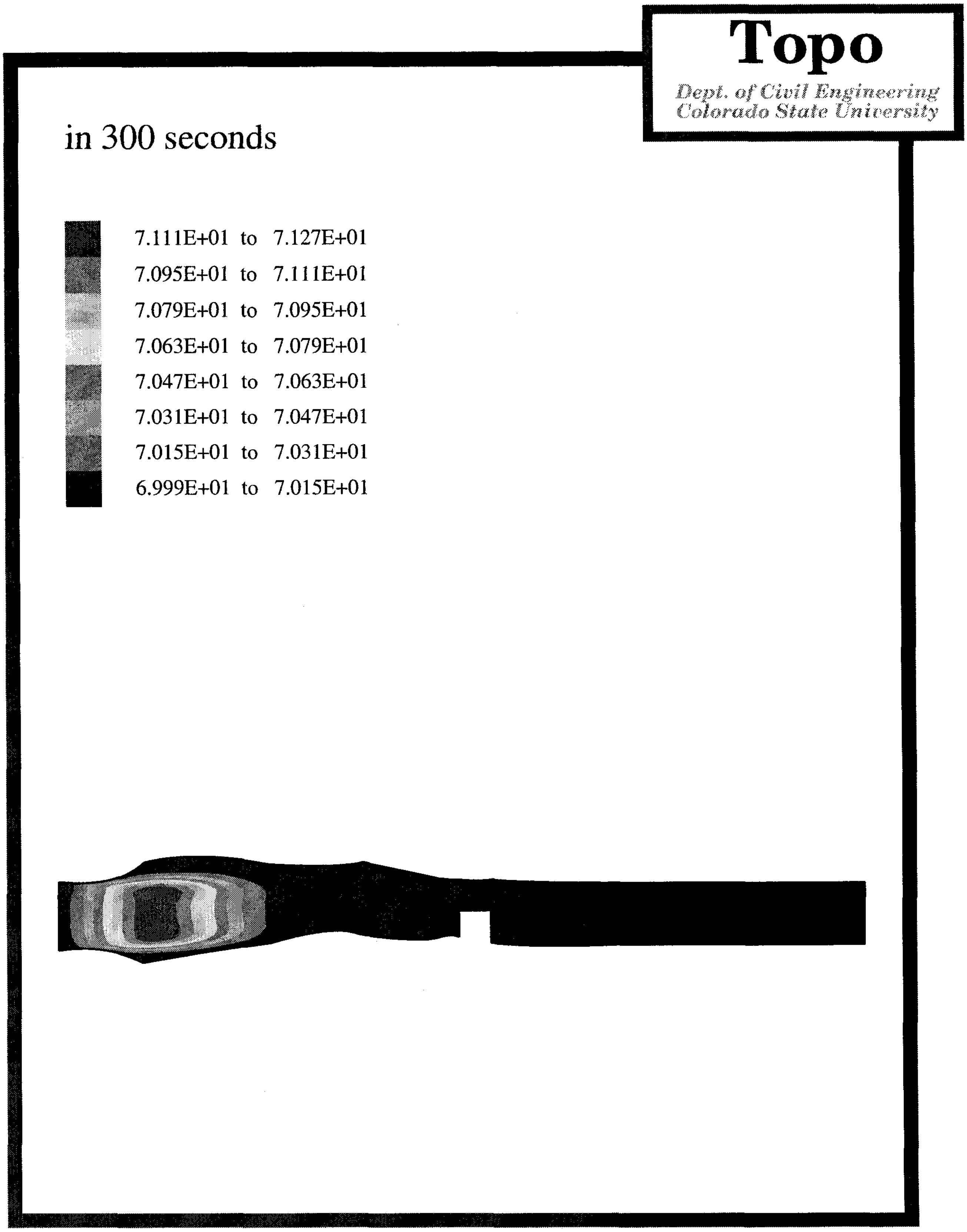
Topo
Dept. of Civil Engineering
Colorado State University
in 300 seconds
7.111E+01 to 7.127E+01
7.095E+01 to 7.111E+01
7.079E+01 to 7.095E+01
7.063E+01 to 7.079E+01
7.047E+01 to 7.063E+01
7.031E+01 to 7.047E+01
7.015E+01 to 7.031E+01
6.999E+01 to 7.015E+01

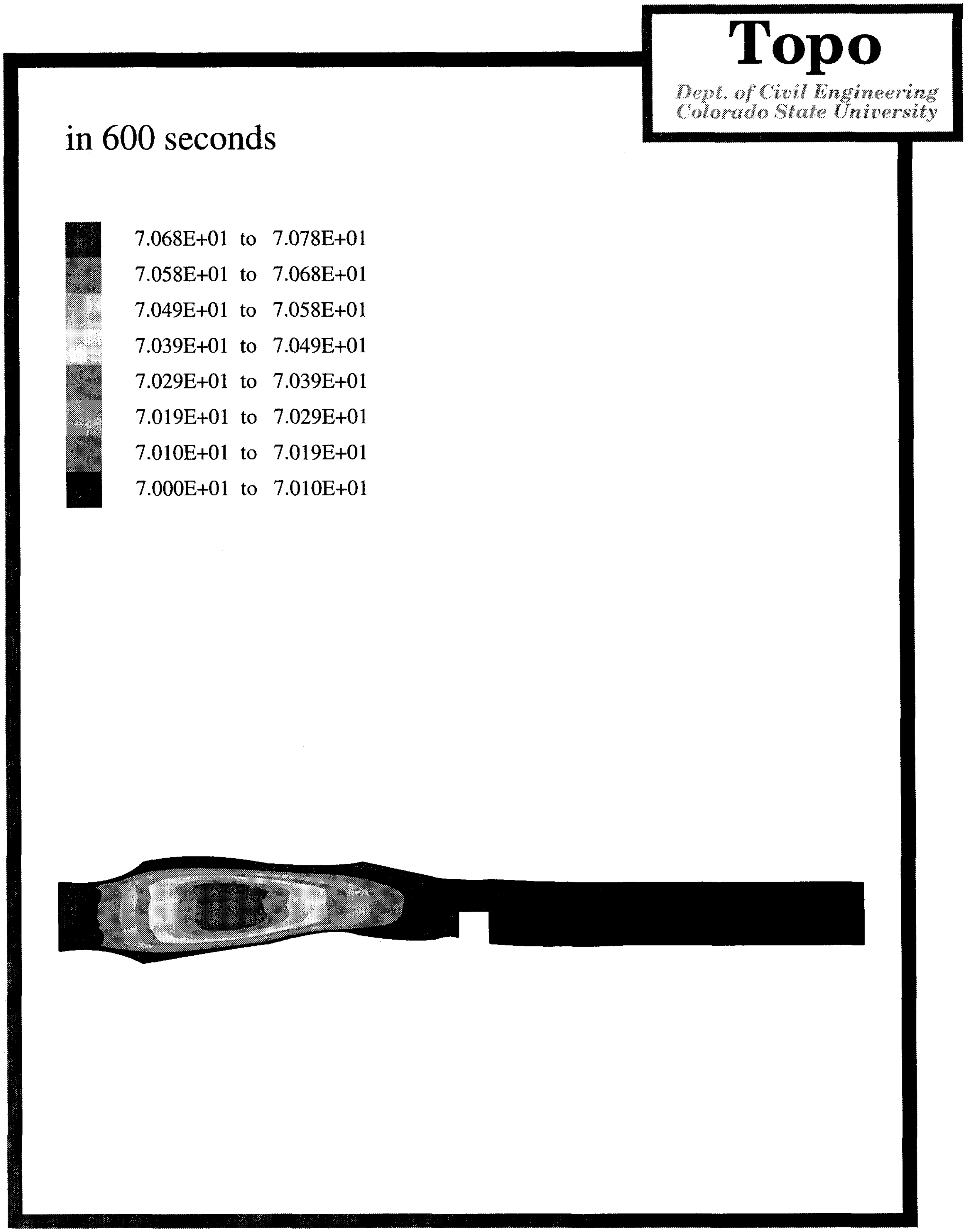
Topo
Dept. of Civil Engineering
Colorado State University
in 600 seconds
7.068E+01 to 7.078E+01
7.058E+01 to 7.068E+01
7.049E+01 to 7.058E+01
7.039E+01 to 7.049E+01
7.029E+01 to 7.039E+01
7.019E+01 to 7.029E+01
7.010E+01 to 7.019E+01
7.000E+01 to 7.010E+01

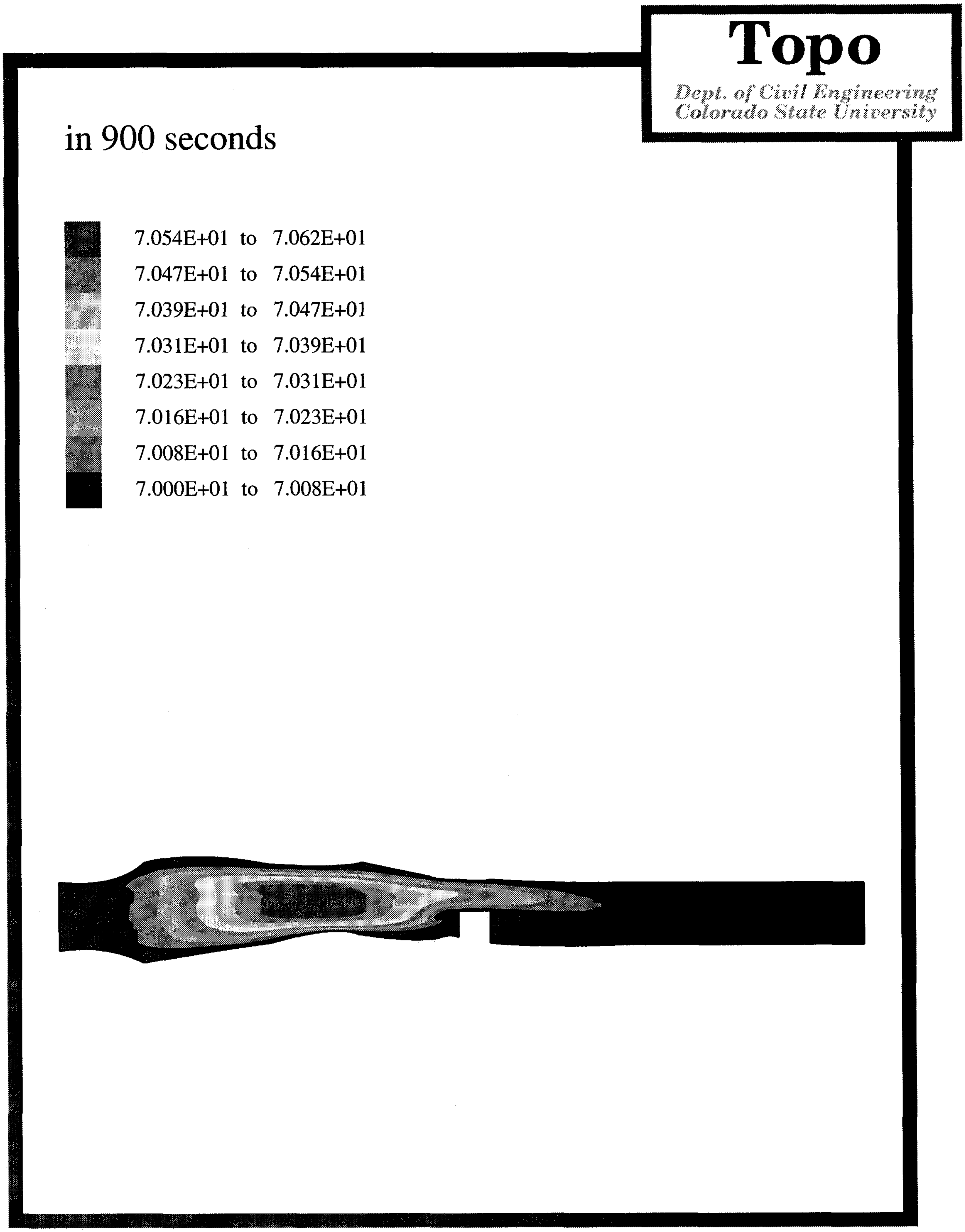
Topo
Dept. of Civil Engineering
Colorado State University
in 900 seconds
7.054E+01 to 7.062E+01
7.047E+01 to 7.054E+01
7.039E+01 to 7.047E+01
7.031E+01 to 7.039E+01
7.023E+01 to 7.031E+01
7.016E+01 to 7.023E+01
7.008E+01 to 7.016E+01
7.000E+01 to 7.008E+01

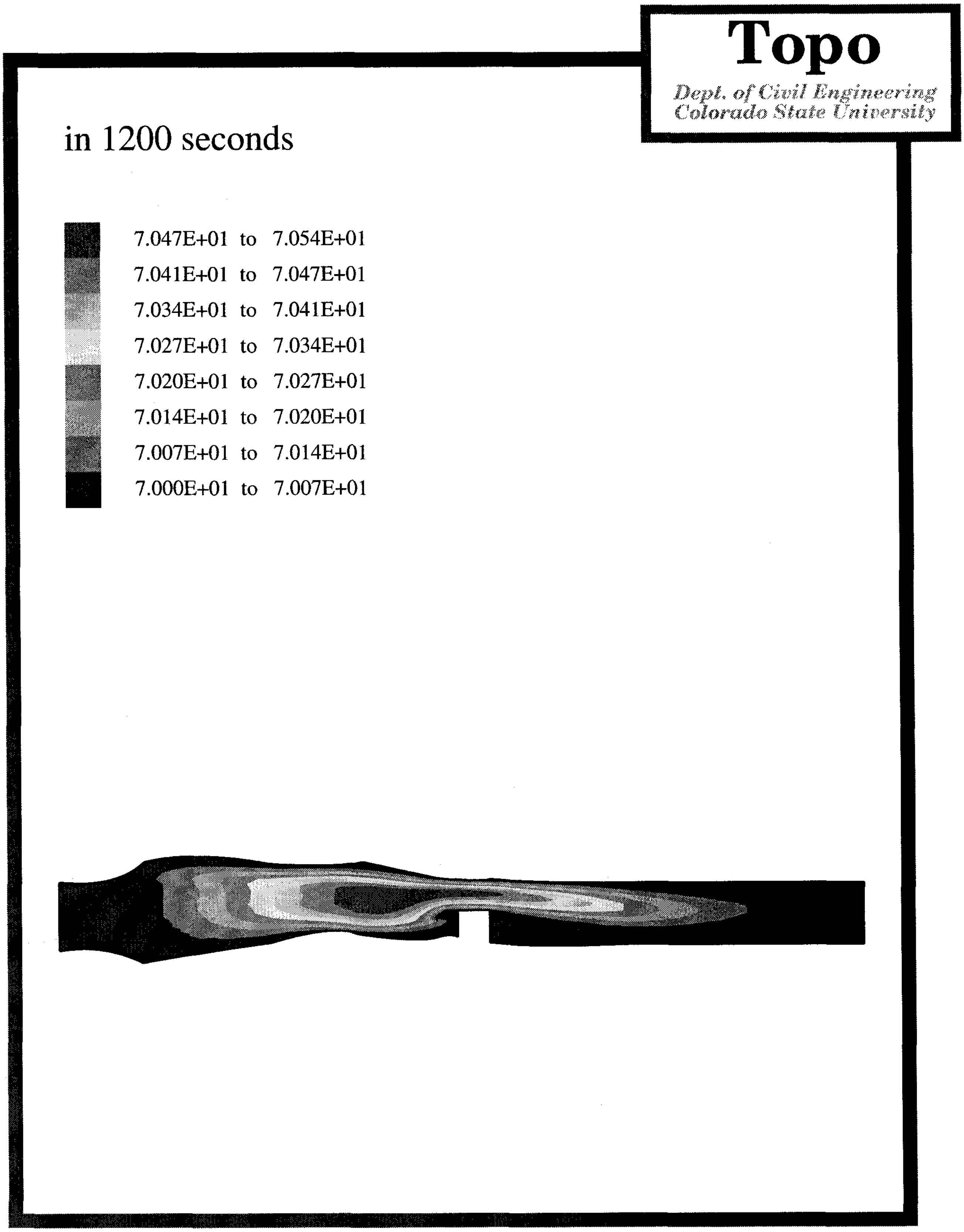
Topo
Dept. of Civil Engineering
Colorado State University
in 1200 seconds
7.047E+01 to 7.054E+01
7.041E+01 to 7.047E+01
7.034E+01 to 7.041E+01
7.027E+01 to 7.034E+01
7.020E+01 to 7.027E+01
7.014E+01 to 7.020E+01
7.007E+01 to 7.014E+01
7.000E+01 to 7.007E+01

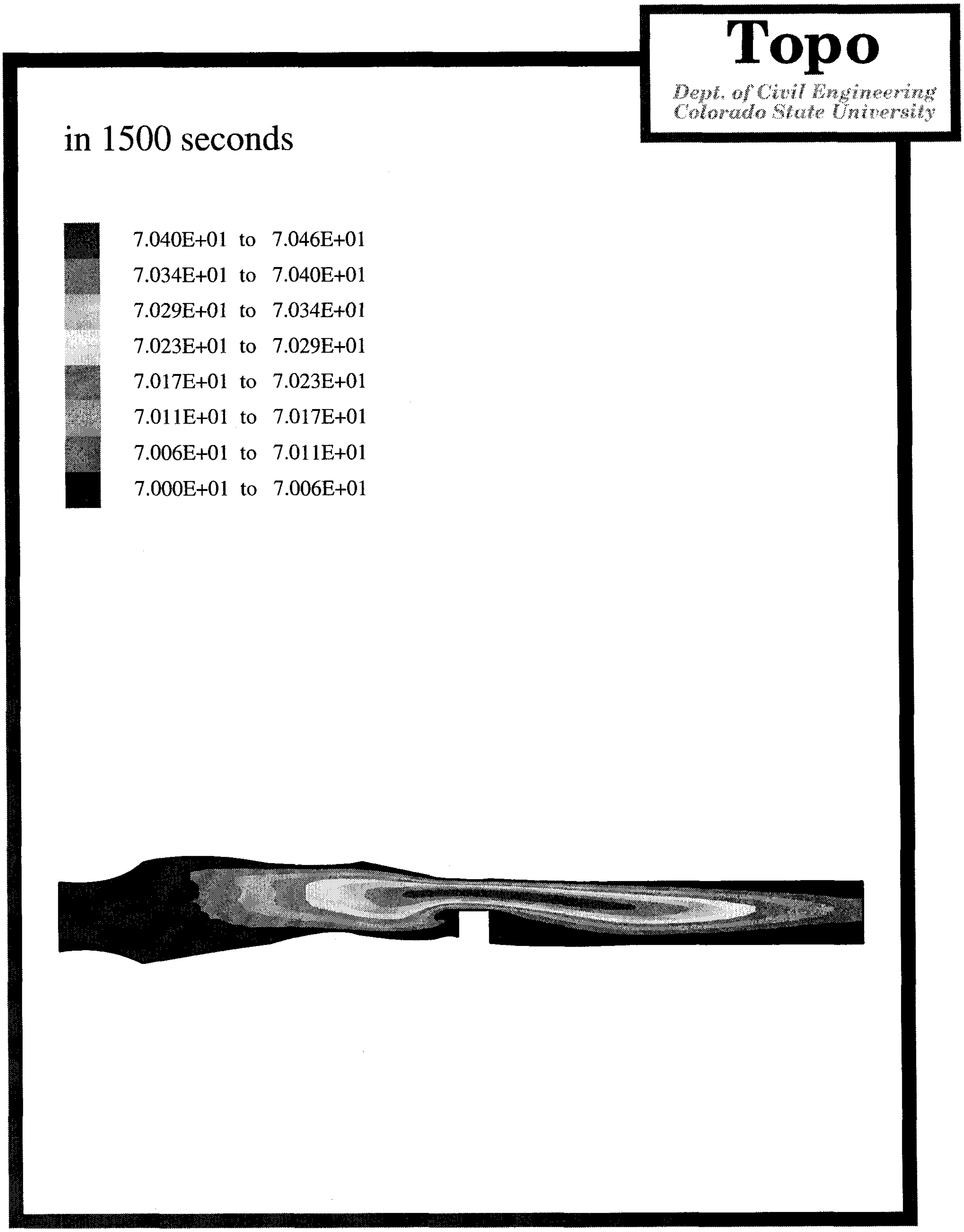
Topo
Dept. of Civil Engineering
Colorado State University
in 1500 seconds
7.040E+01 to 7.046E+01
7.034E+01 to 7.040E+01
7.029E+01 to 7.034E+01
7.023E+01 to 7.029E+01
7.017E+01 to 7.023E+01
7.011E+01 to 7.017E+01
7.006E+01 to 7.011E+01
7.000E+01 to 7.006E+01

Topo

Dept. of Civil Engineering
Colorado State University

in 1800 seconds

7.033E+01 to 7.038E+01
7.028E+01 to 7.033E+01
7.024E+01 to 7.028E+01
7.019E+01 to 7.024E+01
7.014E+01 to 7.019E+01
7.009E+01 to 7.014E+01
7.005E+01 to 7.009E+01
7.000E+01 to 7.005E+01

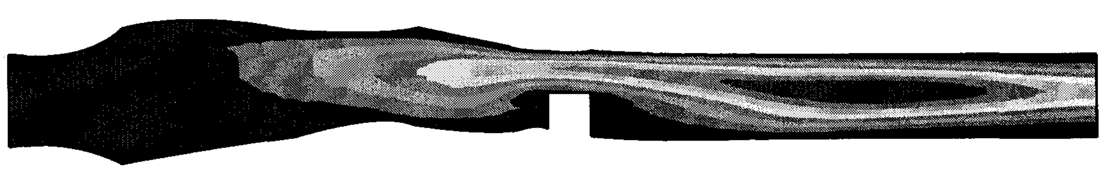

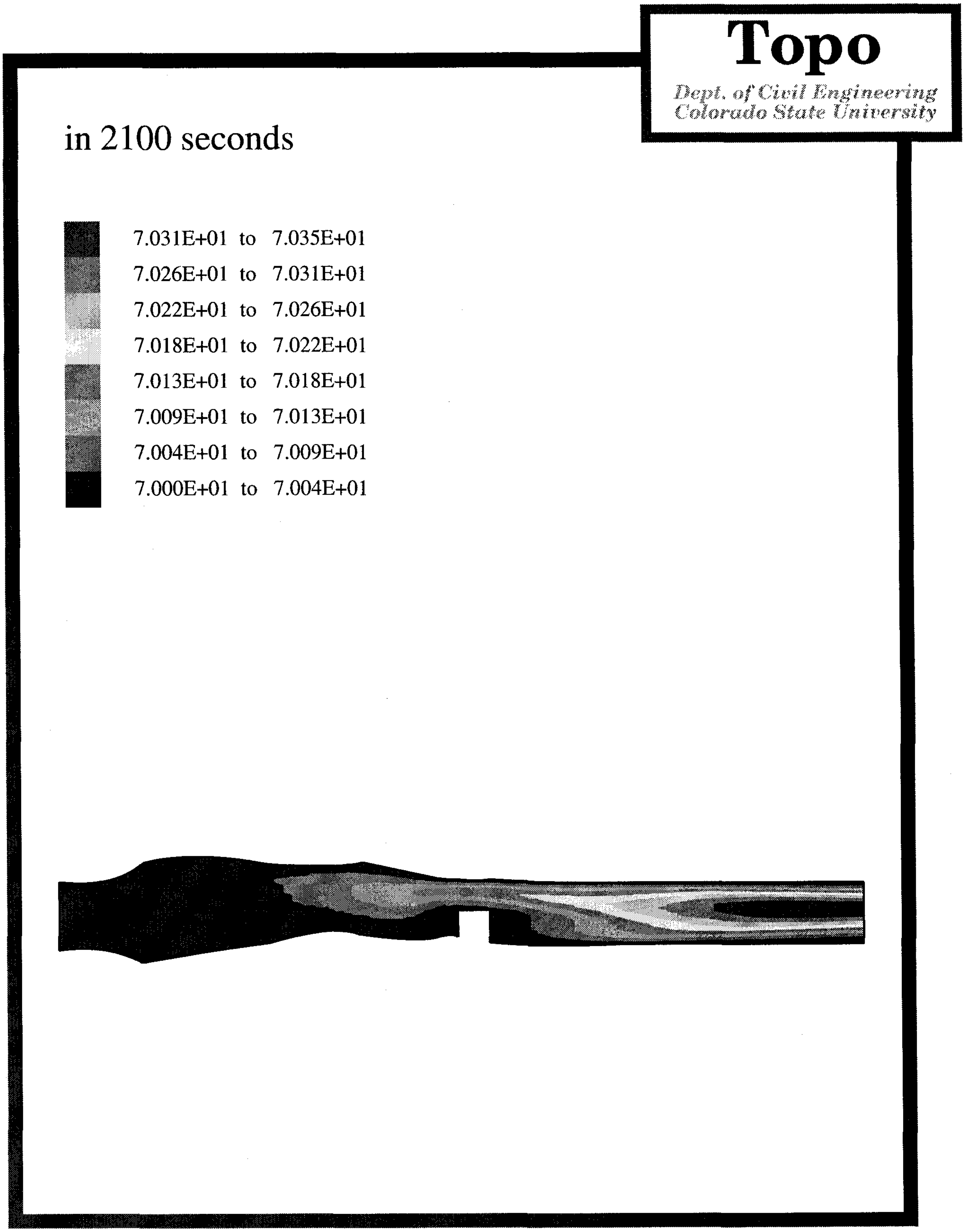
Topo
Dept. of Civil Engineering
Colorado State University
in 2100 seconds
7.031E+01 to 7.035E+01
7.026E+01 to 7.031E+01
7.022E+01 to 7.026E+01
7.018E+01 to 7.022E+01
7.013E+01 to 7.018E+01
7.009E+01 to 7.013E+01
7.004E+01 to 7.009E+01
7.000E+01 to 7.004E+01

Topo

Dept. of Civil Engineering
Colorado State University

in 2400 seconds

7.027E+01 to 7.031E+01
7.023E+01 to 7.027E+01
7.019E+01 to 7.023E+01
7.015E+01 to 7.019E+01
7.012E+01 to 7.015E+01
7.008E+01 to 7.012E+01
7.004E+01 to 7.008E+01
7.000E+01 to 7.004E+01

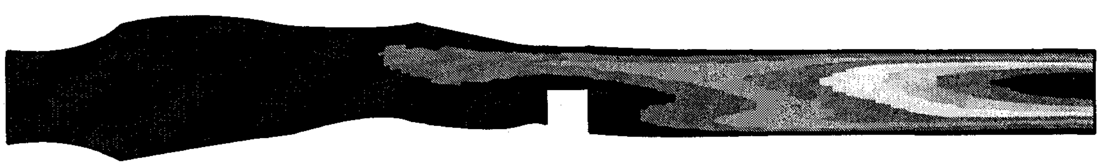

Topo

Dept. of Civil Engineering
Colorado State University

in 2700 seconds

7.019E+01 to 7.022E+01
7.017E+01 to 7.019E+01
7.014E+01 to 7.017E+01
7.011E+01 to 7.014E+01
7.008E+01 to 7.011E+01
7.006E+01 to 7.008E+01
7.003E+01 to 7.006E+01
7.000E+01 to 7.003E+01

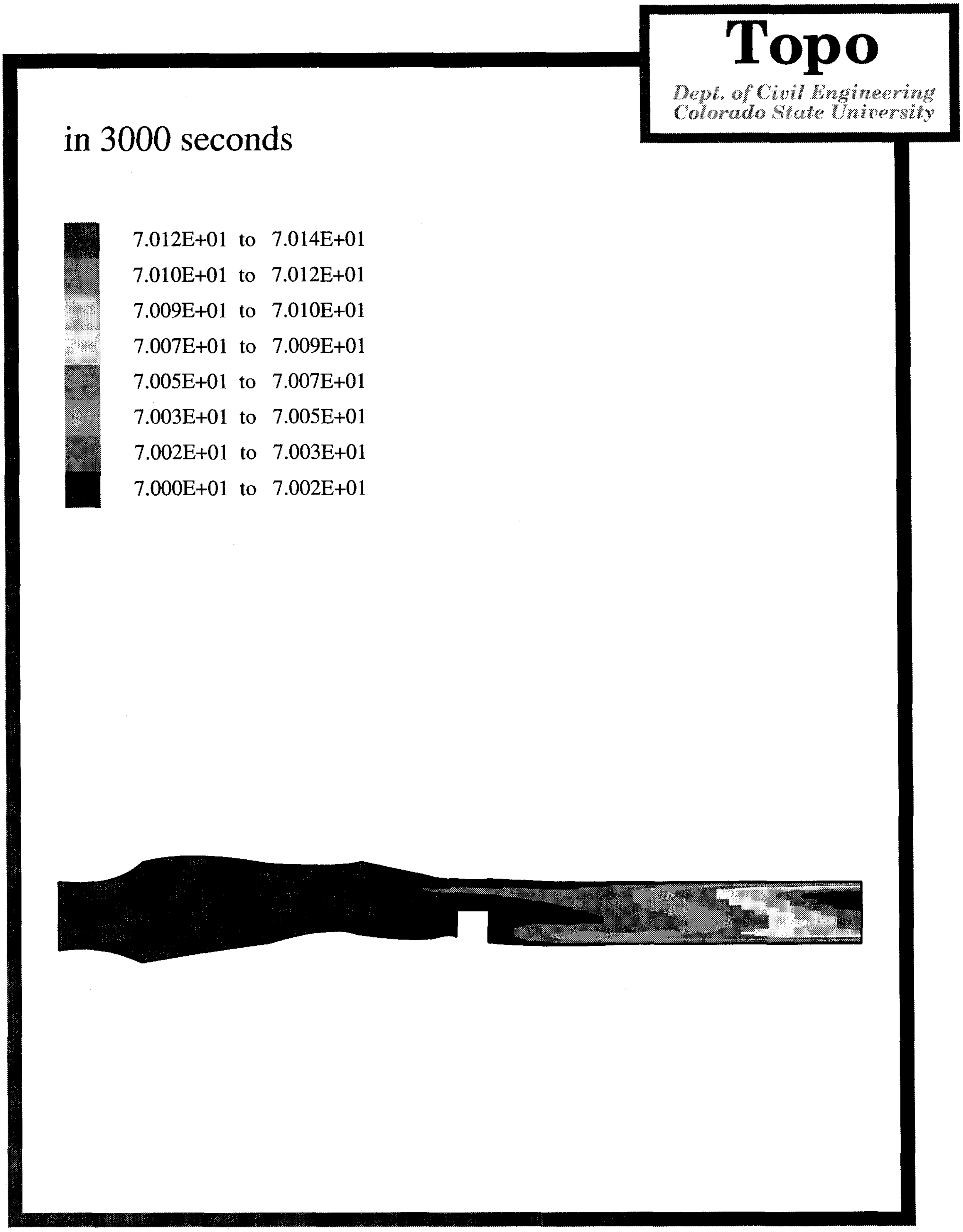
Topo
Dept. of Civil Engineering
Colorado State University
in 3000 seconds
7.012E+01 to 7.014E+01
7.010E+01 to 7.012E+01
7.009E+01 to 7.010E+01
7.007E+01 to 7.009E+01
7.005E+01 to 7.007E+01
7.003E+01 to 7.005E+01
7.002E+01 to 7.003E+01
7.000E+01 to 7.002E+01